Large Amplitude Whistler Waves: Nonlinear Dynamics and Interactions

by

Scott Graham Karbashewski

A thesis submitted in partial fulfillment of the requirements for the degree of

Master of Science

Department of Physics
University of Alberta

Abstract

In this thesis we present Particle-in-Cell (PIC) plasma simulations designed to model large amplitude whistler waves. There are significant nonlinear effects that arise due wave-wave and wave-particle interactions. There are two related sections to this report: one investigating the evolution of the nonlinear dynamics of obliquely propagating whistler waves, and the other investigating the wave-wave coupling between whistler waves and electrostatic modes.

Recent satellite observations by *Cattell et al. (2008)* [20] have identified the presence of large amplitude whistler plasma waves in the Earth's outer radiation belt ($3 \leq L \leq 15$) that propagate obliquely with respect to the Earth's magnetic field. *Cattell et al. (2008)* suggest that these large amplitude whistlers are a mechanism for the rapid acceleration of radiation belt electrons to relativistic energies. Previous efforts have been made in *Yoon (2011)* [19] to simulate these large amplitude whistlers and the resulting particle acceleration using a cold electron fluid model with test particles in the nonlinear wave fields. Additionally, nonlinear effects such as particle trapping in *Kellogg et al. (2010)* [23] and wave steepening in *Yoon (2011)* have been identified as being important to the wave dynamics. We present results from a PIC simulation with self-consistent electromagnetic fields to account for the feedback effects of particles on the large amplitude whistler wave. Using initial conditions to launch a large amplitude plasma wave that is consistent with the dispersion relation for oblique whistler waves we characterize the nonlinear effects in the wave evolution. We show that the wave fields are capable of thermalizing a self-consistent electron distribution from ~ 1 eV to ~ 100 eV, and can accelerate a non-interacting seed population from ~ 100 eV into the range of $\sim 20 - 30$ keV. We highlight the presence of compressional wave steepening effects as well as particle trapping and

wave field distortion and damping that follow thereafter. Finally, we present wave amplitude scaling relations for three important time scales: wave steepening time, particle trapping time, and particle acceleration time.

The second set of simulations revolve around a satellite observation by *Agapitov et al. (2015)* [28] of the parametric decay of a whistler wave into a backscattered whistler and an electron acoustic wave. It is claimed that this process is the source of spiked electrostatic fields in the outer radiation belt observed by *Mozer et al. (2013)* [26] that have been shown by *Artemyev et al. (2014)* [27] to rapidly accelerate $\sim 10 - 100$ eV electron populations into the $\sim 1 - 2$ keV range. We present a set of Darwin PIC simulations investigating the interactions of parallel electromagnetic whistler waves with electrostatic plasma modes. By adding external wave fields consistent with the whistler dispersion to the self consistent electromagnetic fields we launch a whistler wave in different plasma conditions to isolate interactions with the Langmuir, ion acoustic, and electron acoustic wave modes. We identify a nonlinear coupling to the Langmuir mode that results in nonlinear electrostatic structures and modification to the electron velocity distribution at the whistler phase velocity. With moving ions we present multiple parametric decay channels of a whistler into a backscattered whistler and ion acoustic mode that show remarkable agreement with predictions made using a simple ponderomotive force as the coupling mechanism. However, a similar process does not occur for the electron acoustic mode as the Langmuir coupling dominates in this scenario. Drawing from the ion acoustic results and the conditions in *Agapitov et al. (2015)* we suggest that it may be necessary to have a relative drift between hot and cold electron populations to observe the parametric decay of a whistler wave into an electron acoustic wave in space plasma conditions.

Acknowledgements

I would like to thank my research supervisor Professor Richard Sydora for his invaluable guidance throughout this research project. Richard has been an outstanding mentor in my academic career and I have fully appreciated his careful approach to research and his confidence in the work I do. I have been fortunate to develop a great working relationship with Richard and I look forward to continuing my studies with him for the next several years.

This research is simulation based and I would like to thank Dr. Viktor Decyk and Joshua Kelly for their help in setting up the UPIC particle code on my personal computer.

My time in Edmonton has been wonderful so far and I would like to extend a big thank you to all of my extended family members in the city and surrounding area for their valuable support, even though they are not sure what it is I really do. Family BBQs, softball teams, squash Wednesday's, and other gatherings have helped me maintain a great work-life balance the last two years.

Lastly, I'd like to thank my parents for all their support in my choice as a career student. I really appreciate the interest they both show in my research as well as all the free lunches.

Table of Contents

List of Figures

CHAPTER 1.

Introduction

1.1 Background and Motivation

1.1.1 Whistler Waves

Whistler plasma waves are low frequency electromagnetic waves that have become ubiquitous in the research fields of space and plasma physics alike. The "whistler" name is attributed to the rising and falling whistling tones associated with their discovery in World War I over radio communication systems [1, 2]. An example of the time and frequency analysis of these signals when observed from the ground is shown in Fig. 1.1. If converted to audio these produce a short, high frequency whistle.

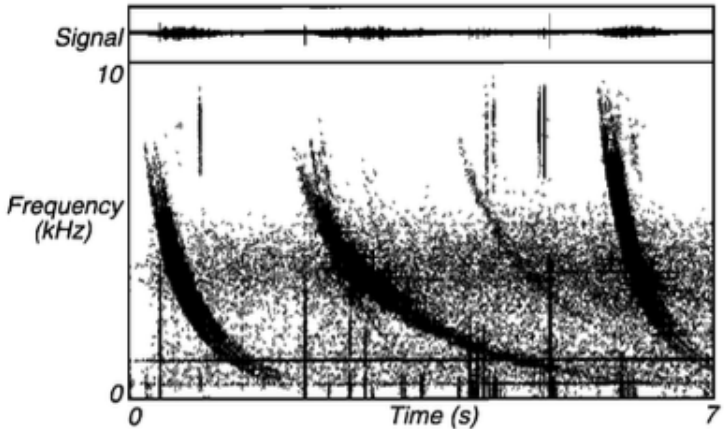

Figure 1.1: (Top) Ground-based radio signal observations of whistler waves. (Bottom) A frequency analysis of the time domain signal showing the characteristic falling tones of whistler waves that have a fast whistling sound when played through a speaker (Taken from Ref. [2]).

The first account linking the sounds heard over radio to an atmospheric phenomenon is attributed to the German physicist Heinrich Barkhausen in his 1919 paper in *Physikalische Zeitschrift* (*Physical Journal*) [3]. In the decade that followed, articles were published correlating the whistling tones to the occurrence of atmospheric clicks or sferics as well as observed lighting stikes [4, 5]. By the mid 1930's the first frequency-time measurements of whistlers had been made that showed quantitatively the dispersive nature of the sounds, and a dispersion law based on theories at the time had been established [6, 7]. It was not until the 1950's that the full nature of the phenomenon had a clear picture when *Storey (1953)* [8] presented a comprehensive experimental study. It was shown that successive whistling tones after an atmospheric click in the northern hemisphere grew in time duration and followed time delay ratios of 1:3:5... and 2:4:6... in the northern and southern hemispheres, respectively. Storey proposed that the waves were propagating along the lines of force of the Earth's magnetic field and reflecting between the two hemispheres. Shortly following this revelation, several independent experiments were able to confirm predictions made by Storey about the observable characteristics of these waves located in near-Earth space [9, 10, 11].

Today, it is understood that whistler waves are a branch of right-hand circularly polarized electromagnetic waves that exist in magnetized plasmas. In Earth's space plasma environment these waves propagate along Earth's geomagnetic dipole field and reflect near the poles, extending the duration of the time domain signal with each bounce; individual whistlers have been recorded to bounce or echo between the poles greater than twenty times [12]. The characteristic rising and falling tones are due to the phase velocity reaching a maximum near the middle of the whistler frequency range; broadband excitation and long transit lengths around the globe mean the frequencies arrive at different times at a measurement location, giving

rise to the chirping tones when converted to sound. In the field of space physics, whistler signals have been recorded from both ground and space throughout Earth's magnetosphere [1, 2], in the solar wind via satellites [13], and in the atmospheres of Jupiter [14] and Saturn [15] by the Voyager 1 and Cassini spacecraft, respectively. In laboratory plasmas, whistlers were first observed in the 1960's and a number of early diagnostic techniques using whistlers were developed [2]. Since then, a large number of experiments have investigated whistlers in laboratory settings, detailing the three-dimensional dispersion, thermal noise spectrum, and various methods of generation from anisotropic distributions relevant to space [2].

In space physics, whistler wave modes are believed to play a key role in the energization and loss of electrons in the magnetosphere and they have long since been linked to the variability of trapped energetic particles in the Earth's radiation or Van Allen belts [16], two large toroidal regions of plasma surrounding Earth [17]. Readers interested in a more detailed description of the radiation belts and Earth's magnetosphere are referred to *Basic Space Plasma Physics* by W. Baumjohann and R.A. Treumann [17], as it is an extensive topic and not directly related to the research herein. Magnetospheric waves consistent with the whistler dispersion are broadly divided into three types: chorus, hiss, and standard whistlers. Whistler chorus, sometimes called the dawn chorus due to its almost exclusive presence on the dawn side of Earth, is characterized by closely grouped discrete whistler tones [12]. One mechanism of chorus excitation is the injection of energetic particles during magnetic substorms [2]; an example of whistler chorus measured at the Palmer research station in Antarctica is shown in the top panel of Fig. 1.2 [18]. Hiss, generally attributed to energetic electron distributions, is broadband incoherent whistler noise that is further subdivided into many groups by different characteristics [2, 12]; an example of whistler hiss measured at the Palmer station is shown in the middle panel of

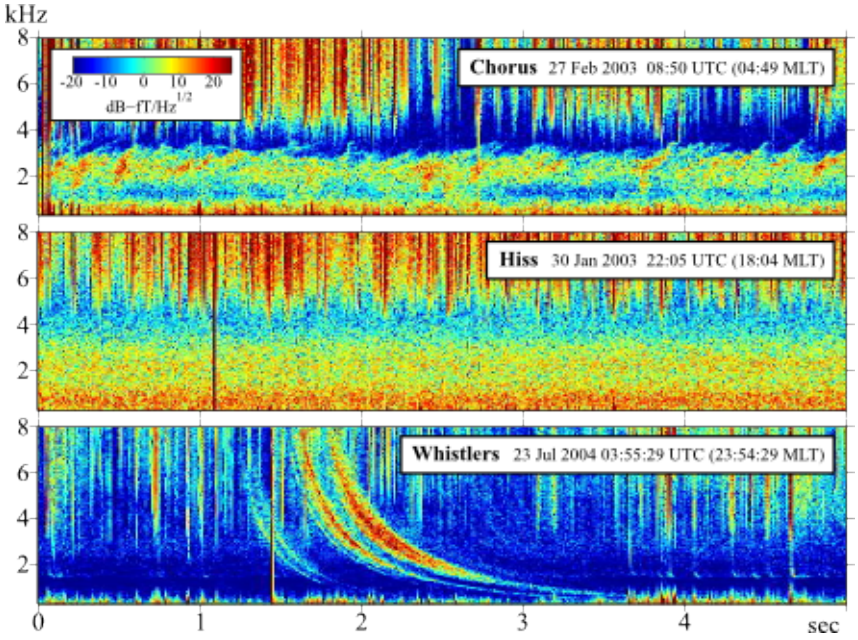

Figure 1.2: (Top) Frequency-time spectrum of whistler chorus waves, the chorus is situated in the range of $1-3$kHz. (Middle) Frequency-time spectrum of whistler hiss, the incoherent hiss noise is situated in the range of $0.5-4$kHz. (Bottom) Frequency-time spectrum of standard whistler waves with falling tones.(Taken from Ref. [18]).

Fig. 1.2. Standard whistlers are the aforementioned coherent whistling tones shown in the bottom panel of Fig. 1.2 and are commonly generated by sferics, broadband electromagnetic impulses excited by lightning strikes that make their way into the magnetosphere.

1.1.2 Large Amplitude Whistlers

Recent STEREO and WIND spacecraft observations in the radiation belts, bow shock and magnetotail of the Earth have revealed that a significant portion of the whistler mode population consists of unusually large amplitude waves. *Cattell et al. (2008)* [20] and *Kellogg et al. (2011)* [21] report quasi-monochromatic whistler mode chorus waves propagating obliquely to the background magnetic field in the lower band frequency range of $\sim 0.2 f_{ce}$, where f_{ce} is the electron cyclotron frequency, with

electric field amplitudes $\gtrsim 100$ mV/m and magnetic field amplitudes $\delta B \sim 0.5-2$ nT that correspond to $\delta B/B_0 \sim 0.01-0.1$ when measured with respect to the background magnetic field B_0. A statistical analysis of the many WIND events reported by *Kellogg et al. (2011)* was conducted by *Wilson et al. (2011)* [22] that showed the wave propagation angle θ with respect to the background magnetic field occurs over a wide range $0^o \leq \theta < 90^o$ and showed the generation may be caused by anisotropic electron distribution functions. For such large amplitude waves nonlinear effects of wave particle interaction are significant.

One such nonlinear effect is particle trapping, which is a mechanism used by *Kellogg et al. (2010)* [23] to interpret the distortion of electric field waveforms measured by the STEREO and Wind satellites. The physical effects of electrons trapped in the potential of the electrostatic part of the oblique whistlers was analyzed and shown to result in significant transport of trapped electrons leading to electrostatic potentials of several kilovolts. This effect is demonstrated by the large amplitude whistler event in Fig. 1.3, the black line is the distorted sinusoidal electrostatic potential of the large amplitude wave, the electron density is shown in red, and the calculated density of trapped electrons that account for the distortion is indicated by the green line.

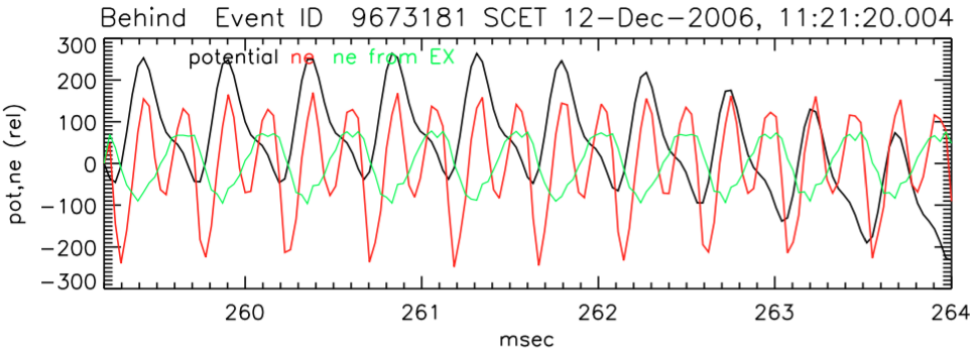

Figure 1.3: A large amplitude oblique whistler event showing a distorted electrostatic potential (black), the electron density (red) and the a calculated density profile of trapped electrons that account for the distortion of the electrostatic potential (Taken from Ref. [23]).

Using the observed oblique whistler wave fields as a guide, *Cattell et al. (2008)* performed test particle simulations and demonstrated rapid electron energy gain from $\sim$ 0.1 MeV up to $\sim$ 4 MeV in timescales on the order of tens of ms that could account for STEREO observations of electron intensity enhancements. *Bortnik et al. (2008)* [24] and *Tao and Bortnik (2010)* [25] performed test particle simulations and demonstrated acceleration similar to *Cattell et al. (2008)* but using simpler wave models.

Subsequently, *Yoon (2011)* [19] carried out relativistic test particle simulations using wave fields obtained by solving the fully nonlinear cold electron fluid equations for obliquely propagating large amplitude whistlers. This work pointed out the importance of nonlinear wave steepening effects due to the presence of longitudinal field components; Fig. 1.4 depicts the density profile from the simulations in *Yoon (2011)* that show distortion of the initial sinusoidal waveform due to wave steepening. The results showed that a population of initially $\sim$ 500 keV electrons could be accelerated to $\sim 10MeV$ energies within a few seconds. A limitation of this work is that it did not include thermal and collective dissipation effects and back-reaction of the trapped and energetic particles on the nonlinear wave fields.

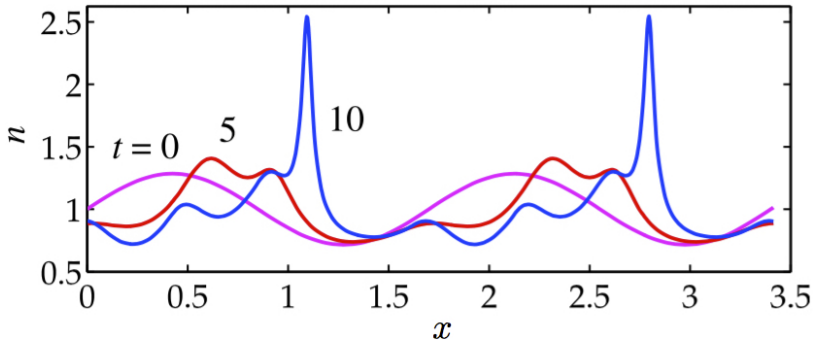

Figure 1.4: The evolution of the electron density from a numerical solution of an oblique whistler wave propagating at an angle $\theta = 70^o$ with respect to the background magnetic field. Wave steepening effects cause the initially sinusoidal profile to become extremely nonlinear (Taken from Ref. [19]).

1.1.3 TIME DOMAIN STRUCTURES AND WHISTLER DECAY

Mozer et al. (2013) [26] report on large numbers of short spiked structures in the electrostatic field observed in the outer radiation belt by the Van Allen Probes. These rapid bursts, lasting on the order of seconds to several minutes, of millisecond timescale spikes have been dubbed Time Domain Structures (TDS) and have been identified as nonlinear electron acoustic wave (EAW) modes. *Artemyev et al. (2014)* [27] highlighted the importance of these phenomena to the overall view of belt dynamics by showing that a single TDS burst can rapidly accelerate $\sim 10 - 100$ eV thermal electron populations into the range of $\sim 1 - 2$ keV. A significant event observed by the Van Allen Probes spacecraft was reported in *Agapitov et al. (2015)* [28] which showed a chorus whistler wave decaying into a backwards travelling whistler and an electron acoustic wave. Such a process is known as a parametric decay and is a common type of instability observed in plasmas. This event is presented in Fig. 1.5; panel

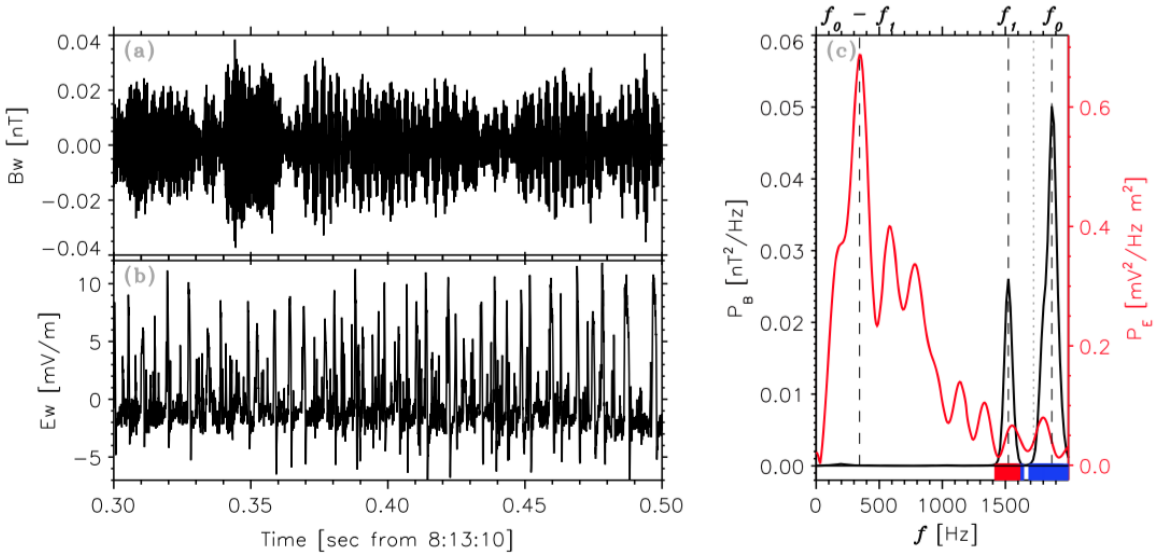

Figure 1.5: (a) Transverse magnetic field component measuring whistler waves. (b) Electrostatic field depicting TDS and the electron acoustic wave. (c) Fourier analysis of the signals (a) in black and (b) in red. The frequency matching of the parametric decay is indicated. (Taken from Ref. [28]).

(a) depicts the transverse magnetic fluctuations containing the whistler wave, panel (b) the TDS and electron acoustic wave, and (c) the frequency analysis of the whistler (black) and EAW (red) components. The frequency of the EAW being the difference of two whistler frequencies depicted in (c) is indicative of a parametric decay process. The authors propose the resulting EAW evolves though electron trapping into the nonlinear TDS that are responsible for rapid particle acceleration. This event and its possible large importance in understanding global radiation belt dynamics pushes for a better understanding of the mechanisms and conditions that facilitate the coupling of electromagnetic whistler wave modes to electrostatic modes.

1.2 OBJECTIVES

One objective of this work is to extend upon the work of *Yoon (2011)* and include the thermal and feedback effects absent in the cold electron fluid description and quantify their impact on the nonlinear dynamics of oblique whistler waves. Electromagnetic particle-in-cell (PIC) simulations with relativistic particle dynamics are used to model the evolution of an initial large amplitude oblique whistler wave perturbation. The evolution of the wave is investigated to develop a more detailed understanding of the wave steepening processes highlighted by *Yoon (2011)*. Additionally, the nonlinear effect of particle trapping is analysed using particle trajectories and electrostatic potentials to be compared with work presented in *Kellogg et al. (2010)*. And finally, particle energization is studied to make comparisons with the energizations reported in previous simulations.

The event observed by *Agapitov et al. (2015)* and subsequently interpreted as the parametric decay of a whistler wave into a backscattered whistler and electron acoustic wave presents a unique opportunity for an investigation into nonlinear wave-wave interactions involving whistler waves. We wished to model with an electromagnetic

Darwin PIC code the coupling of a pumped whistler with different electrostatic wave modes, namely, the typical Langmuir waves, ion acoustic waves (IAW), and aforementioned electron acoustic waves. *Agapitov et al. (2015)* note that the EAW and IAW parametric coupling with whistler waves are similar processes theoretically and study of one could lead to insights about the other. The results of these isolated simulations can be tied back to the space observations to make a statement about the criteria for these physical processes to occur.

1.3 Thesis Outline

In the next chapter, Chapter 2, we present the background theory that is necessary for understanding the physical phenomena being investigated. A more rigorous description of the electromagnetic modes present in a magnetized plasma is given with special attention given to whistler waves at oblique angles. Next, a description of both the ion acoustic and electron acoustic wave dispersion relations and characteristics are summarized. Following this we present a derivation of the ponderomotive force, an important nonlinear plasma phenomena that can facilitate coupling between electromagnetic and electrostatic wave modes. Finally, this chapter ends with a description of parametric decay processes and the conditions necessary for them to occur.

In Chapter 3 the particle codes used to investigate the objectives outlined in Section 1.2 are explained. We begin with a general description of plasma modelling with PIC codes and move to a more detailed description of the inner workings of two different codes and the simulation parameters used to model the whistler waves. Chapter 4 contains the results of modeling the nonlinear dynamics of oblique whistler waves outlined in the first objective. Chapter 5 presents results from modelling the interactions of parallel whistler waves with electrostatic wave modes. Finally, this thesis and possible extensions on the results herein are summarized in Chapter 6.

CHAPTER 2.

Theory

2.1 Whistler Waves

The importance of whistler waves to many space physics phenomena was discussed previously in Section 1.1.1. In this section we present the dispersion relation that defines the relationship between the frequency ω and wavenumber k for electromagnetic modes that can exist in a magnetized plasma. To begin we use a cold uniform magnetized plasma and ignore the interactions between the electrons and ions. Using linear theory the particle equations of motion are solved consistent with Maxwell's Equations to obtain an expression for the dispersion relation which contains terms dependent on the motions of both the electrons and ions. In the simulations presented in Chapters 4 and 5 we will be dealing with fixed ions or else we are not concerned with the modes introduced by moving ions and we can ignore the ion terms. Thus, the general dispersion relation for electromagnetic waves in a cold uniform magnetized plasma propagating at an oblique angle θ with respect to the magnetic field is [29],

$$\frac{c^2k^2}{\omega^2} = \frac{RL\sin^2\theta + PS(1+\cos^2\theta) \pm [(RL-PS)^2\sin^4\theta + 4P^2D^2\cos^2\theta]^{\frac{1}{2}}}{2(S\sin^2\theta + P\cos^2\theta)} \tag{2.1}$$

and we define,

$$R = 1 - \frac{\omega_{pe}^2}{\omega(\omega+\omega_{ce})}$$

$$L = 1 - \frac{\omega_{pe}^2}{\omega(\omega - \omega_{ce})}$$
$$P = 1 - \frac{\omega_{pe}^2}{\omega}$$
$$S = \frac{1}{2}(R + L)$$
$$D = \frac{1}{2}(R - L)$$

where $\omega_{ce} = \frac{eB_0}{m}$ is the electron cyclotron frequency defined with respect to the magnitude of the external magnetic field B_0 and $\omega_{pe} = \left(\frac{n_e e^2}{\epsilon_0 m_e}\right)^{\frac{1}{2}}$ is the electron plasma frequency. Eq. (2.1) is often called the Appleton-Hartree equation who each derived it separately [32, 33]; the form presented here is derived from *Introduction to Plasma Physics: With Space and Laboratory Applications* by D.A. Gurnett and A. Bhattacharjee and interested readers are directed there for a full derivation of the solution [29]. Fig. 2.1a shows Eq. (2.1) for waves propagating parallel to the background magnetic field, i.e. $\theta = 0^o$; the unitless normalizations ω/ω_{pe} and kc/ω_{pe} will be used throughout this report for most dispersion plots. The lower branch below the electron cyclotron frequency is the whistler branch. Recall that the whistler wave is right hand circularly polarized in the sense that it always rotates in the same direction as electron cyclotron orbits. As the whistler branch approaches the electron cyclotron frequency it reaches a resonance. Near the resonance the wavelength becomes very small and is on the order of the electron cyclotron radius. Additionally, the phase velocity and group velocity of the whistler wave both approach zero, while the wave momentum increases. The wave particle interactions are very strong in this regime and the wave will most often give energy to electrons and experience what is called cyclotron damping. As a result the whistler branch is heavily damped beyond small wavenumbers. Inclusion of ion terms in Eq. (2.1) would reveal another low frequency branch resembling the whistler branch except that it is left hand polarized

and resonant at the ion cyclotron frequency; we are not concerned with this branch in the present study and can safely ignore it in simulations with moving ions since $\omega_{ci} \ll \omega_{ce}$ and the waves will not interact. The upper branches of Fig. 2.1a are left

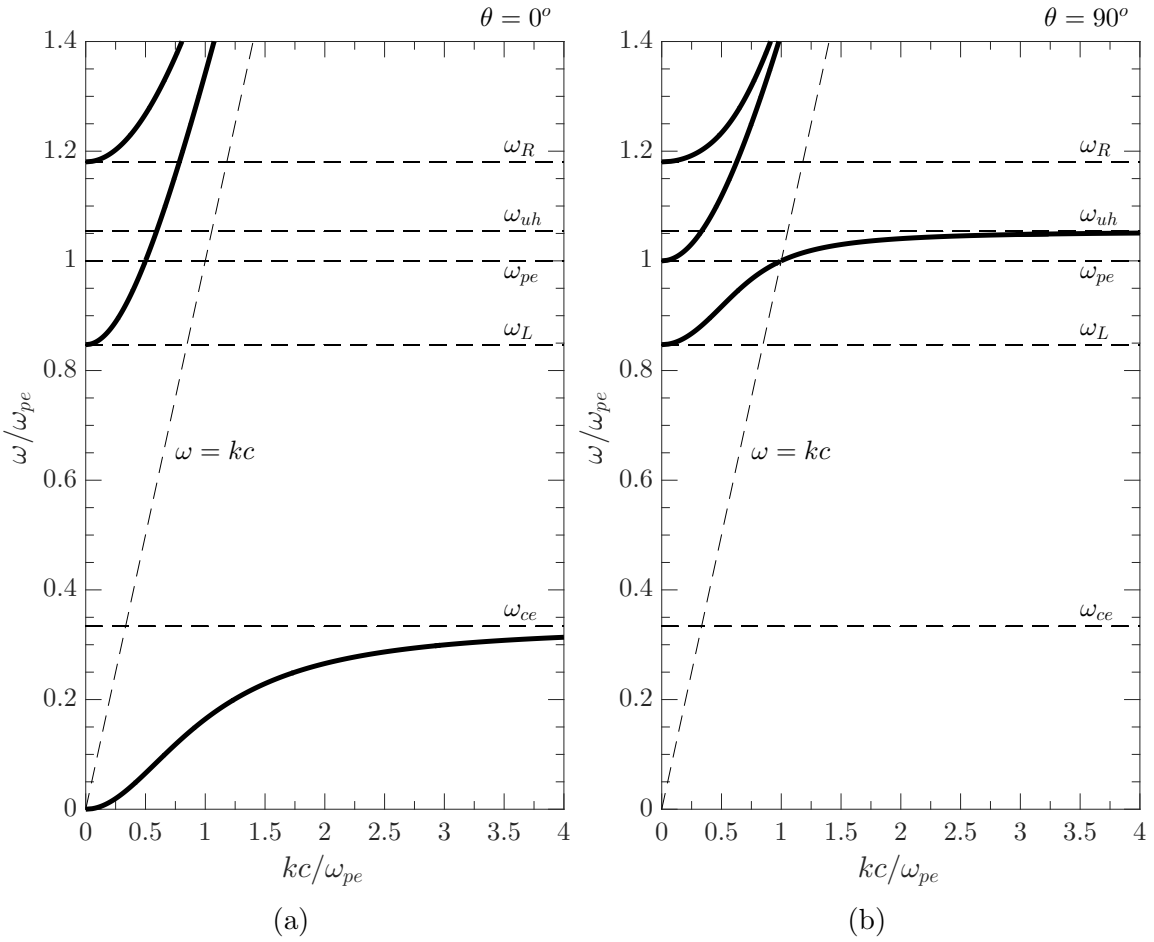

Figure 2.1: Dispersion relations for electromagnetic waves in a cold magnetized plasma. (a) Waves propagating parallel to the background magnetic field, the whistler branch saturates at the electron cyclotron frequency ω_{ce}. (b) The solution for waves propagating perpendicular to the background magnetic field has no whistler wave branch.

and right hand circularly polarized modes that closely resemble light waves and approach the vacuum electromagnetic wave solution $\omega = kc$ at short wavelengths; these high frequency modes do not exist below the left and right hand cuttoffs ω_L and ω_R,

respectively. The solution for perpendicular propagation is shown in Fig. 2.1b and the whistler branch no longer exists. Instead we see the presence of an electromagnetic mode beginning at the left hand cutoff frequency that hits a resonance at the upper hybrid frequency ω_{uh}. This is the lower branch of the extraordinary mode or X-wave, so named due to its longitudinal as well as transverse electric field components. There are again two light wave branches, the ordinary or O-wave has a cutoff at the plasma frequency and is linearly polarized with the electric field parallel to the background magnetic field, and the upper X-wave which has a cutoff at ω_R. The electromagnetic modes are very distinct in the perpendicular vs. parallel regimes but become more complex at oblique angles. Fig. 2.2a and Fig. 2.2b show Eq. (2.1) for angles $\theta = 30^o$ and $\theta = 70^o$, respectively. For oblique propagation we have a mix of (R,L) and (O,X) modes and both the lower X-mode and whistler branch are present. However, the whistler branch is modified in that it now also contains a longitudinal electric field component in addition to the circularly polarized transverse components. Another feature of the whistler branch is the decreasing resonance frequency from the cyclotron frequency at parallel propagation. The angle at which a whistler frequency can no longer propagate is called the whistler resonance angle θ_{res} defined by [17],

$$\cos\theta_{res} = \frac{\omega}{\omega_{ce}} \tag{2.2}$$

The resonance frequency of the oblique whistler mode is at the frequency with a resonance angle matching the propagation angle.

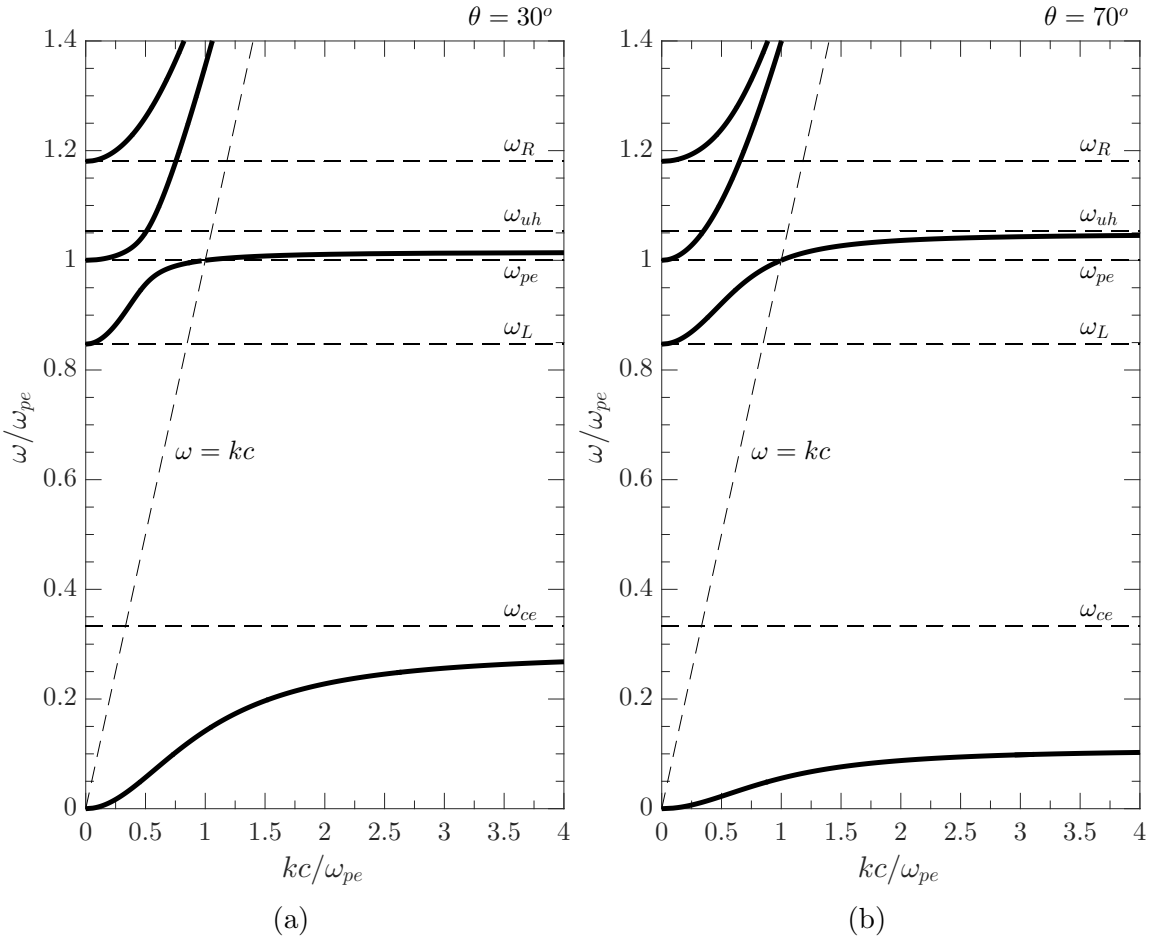

Figure 2.2: Dispersion relations for obliquely propagating electromagnetic waves in a cold magnetized plasma. For oblique propagation the whistler branch exists but reaches a resonance at $\omega = \omega_{ce} \cos\theta$. (a) Waves propagating at an angle $\theta = 30^o$ with respect to the background magnetic field. (b) Waves propagating at an angle $\theta = 70^o$ with respect to the background magnetic field.

2.2 Ion Acoustic Waves

Ion acoustic modes are low frequency electrostatic waves that are analogous to collisional sound waves in a gas, except the vibrations of ions are transmitted through the electric field instead [17, 30]. Observations of ion acoustic waves have been made in Earth's auroral regions of the ionosphere and have been suggested to be important in auroral energization processes [34, 35]. In the solar wind both whistler waves and ion

acoustic waves have been observed and may be responsible for particle energization in the solar wind upstream from Earth's bow shock [36, 37]. In the radiation belt regions of Earth's magnetosphere parametric instabilities between whistler waves and ion acoustic waves have been suggested to be possible and may play a role in belt dynamics [38]. The derivation of the dispersion relation is a simple yet tedious one best presented using a fluid description and we leave the rigours of the mathematics to others, readers can refer to any introductory plasma physics text such as those by Baumjohann and Treumann [17], Chen [30], and Nicholson [31]. The dispersion relation for ion acoustic waves is dependent on both the temperature of the electrons T_e and ions T_i as well as the mass of the ions M and defines the ion acoustic velocity v_{ia},

$$v_{ia} = \frac{\omega}{k} = \left(\frac{\gamma_e K T_e}{M} \frac{1}{1 + k^2 \lambda_{De}^2} + \frac{\gamma_i K T_i}{M} \right)^{\frac{1}{2}} \tag{2.3}$$

where K is the Boltzmann constant, $\lambda_{De} = \left(\frac{\epsilon_0 K T_e}{n_e e^2} \right)^{\frac{1}{2}}$ is the electron debye length, and γ_s is the heat capacity ratio with $\gamma_i = 3$ for ions moving in one dimension and $\gamma_e = 1$ for isothermal electrons [30]. Ion acoustic waves experience heavy Landau damping by ions moving at velocities near the ion acoustic phase velocity, thus the waves become significant only when $T_e \gg T_i$ and the contribution of the ion temperature term becomes negligible [39, 40]. Inspection of Eq. (2.3) reveals that the ion acoustic wave has a mostly linear dispersion until reaching large k, or short wavelengths. Fig. 2.3 shows the ion acoustic dispersion relation across a large range of k to depict both the linear dispersion and constant frequency regions.

If we ignore the ion temperature contribution and take $k\lambda_{De} \gg 1$ then Eq. (2.3)

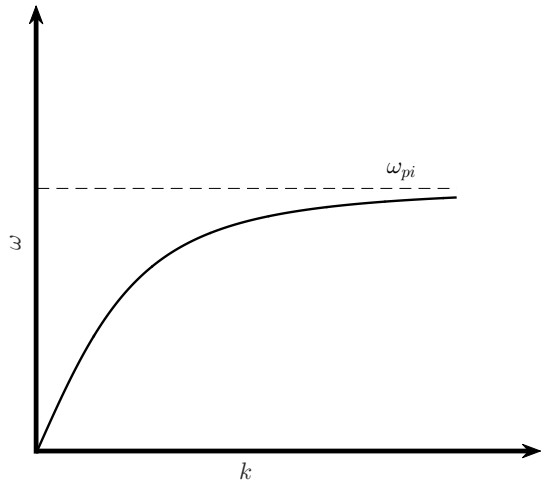

Figure 2.3: The ion acoustic dispersion relation defined by Eq. (2.3). The dispersion relation is linear at long wavelengths and resonates at the ion plasma frequency at short wavelengths.

becomes [30],

$$\omega^2 = k^2 \frac{n_i e^2}{\epsilon_0 M k^2} = \frac{n_i e^2}{\epsilon_0 M} \equiv \omega_{pi}^2 \tag{2.4}$$

where ω_{pi} defines the ion plasma frequency and we have used the plasma approximation $n_i = n_e = n_0$. Eq. (2.4) states that in the short wavelength limit the ion acoustic wave frequency resonates at the ion plasma frequency. We note that the whistler wave region of the lower right hand electromagnetic branch has relatively small k and thus the ion acoustic branch essentially has a linear dispersion in this region.

2.3 Electron Acoustic Waves

The electrostatic dispersion relation for a homogeneous, unmagnetized plasma yields three solutions and was first solved numerically in *Fried and Gould (1961)* [41]. Two of the roots are lightly damped solutions and correspond to the familiar Langmuir or electron plasma waves and ion acoustic waves. The third root is an electron acoustic-like solution that is heavily damped under uniform plasma conditions. The third

solution was largely ignored in plasma and space physics research at the time due to its unlikely role in understanding physical phenomena. *Watanabe and Taniuti (1977)* [42] showed that if the plasma is made up of two electron components, one hot at T_h and one cold at T_c relative to the other, then the third solution can become only lightly damped for a finite range of wavenumbers. Furthermore, *Yu and Shukla (1983)* [43] highlighted that the frequency of the electron acoustic mode had a strong dependence on the desity ratio n_h/n_c of the hot and cold electron populations.

Around this time a number of observations were made of the growth of electron acoustic modes in the Earth's bow shock [44] and the auroral ionosphere [45, 46] and this phenomena was dubbed the "electron acoustic instability". Following this revival of interest *Gary and Tokar (1985)* [47] presented the parameter regime for which the electron acoustic mode is lightly damped. Fig. 2.4 is taken from Ref. [47] and maps out the region where the electron acoustic mode is lightly damped as a function of the density and temperature ratios. The approximate conditions are $T_h/T_c < 10$ and $0 < n_c < 0.8n_e$ where $n_e = n_h + n_c$. An interesting outcome is that a very small population that is sufficiently cold compared to the hot population can produce undamped electron acoustic modes.

Additionally, *Gary (1987)* [48] showed that the instability reported in the space observations of Refs. [44, 45, 46] was due to counter streaming populations of hot and cold ions that resulted in growth of the electron acoustic mode. The electron acoustic wave has been reported to be produced in laboratory experiments using only hot and cold populations [49] and also driven unstable using a relative drift between the populations with an electron beam [50]. In some of the simulations presented in Chapter 5 we will be using two electron populations to create a condition where the electron acoustic mode is lightly damped but we do not drive it unstable with relative drifts of the populations.

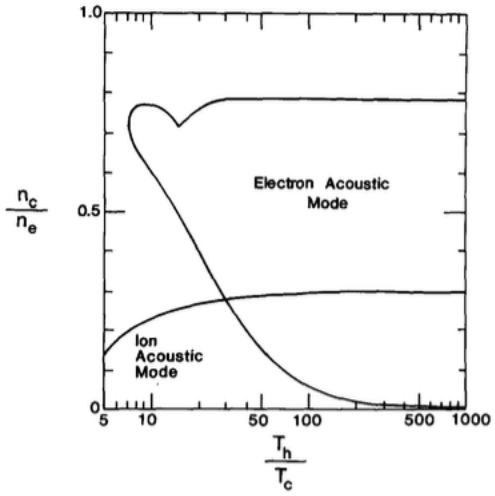

Figure 2.4: The parameter space for which the electron acoustic mode is lightly damped is shown as a function of the density and temperature ratios of hot and cold electron populations. In addition to Langmuir oscillations, plasmas within the undamped region will exhibit thermal electron oscillations consistent with the electron acoustic dispersion relation (Taken from Ref. [47]).

The dispersion relation for the electron acoustic mode is not a simple expression, but an approximation for the undamped range of wavenumbers is given by [47],

$$\omega^2 \approx \omega_{pc}^2 \frac{1 + 3k^2/k_c^2}{1 + k_h^2/k^2} \tag{2.5}$$

where $\omega_{ps} = \left(\frac{n_s e^2}{\epsilon_0 m_e}\right)^{\frac{1}{2}}$ and $k_s^2 = \left(\frac{m_e}{KT_s}\right)^2 \omega_{ps}^2$ and the subscript s is replaced by h and c for the hot and cold electron populations, respectively. Fig. 2.5 taken from Ref. [47] displays the complex frequency dispersion relations for Langmuir and electron acoustic waves at varying density ratios and a constant temperature ratio of $T_h/T_c = 100$. The undamped range of the electron acoustic mode is generally around ω_{pc} which increases with the cold fraction of the total population, as does the minimum k for which the electron acoustic wave is undamped. Thus for lower cold population fractions the electron acoustic wave is more likely to be able to interact with the undamped region of the whistler branch.

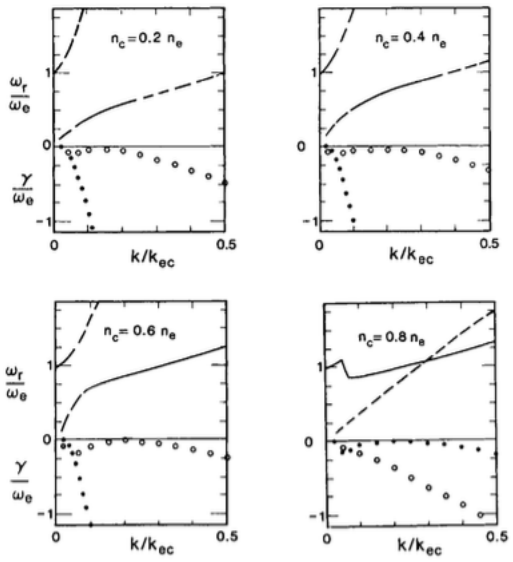

Figure 2.5: The dispersion relations for Langmuir and electron acoustic waves for varying density ratios of hot and cold populations at $T_h/T_c = 100$. The normalizations used are unitless where ω_r follows from a different set of notation and is simply the mode frequency ω, γ is the complex frequency component indicated by black cirlces for Langmuir waves and empty circles for electron acoustic waves, ω_e is the plasma frequency of the combined populations; the solid lines of the real frequency indicate where the mode is lightly damped and dashed lines where it is heavily damped (Taken from Ref. [47]).

2.4 PONDEROMOTIVE FORCE

Before discussing parametric decay processes in the next section it is necessary to present a derivation and interpretation of the ponderomotive force, an effect that arises in plasmas due to spatial variations of the electric field from either electrostatic or electromagnetic origins. The ponderomotive force is a nonlinear effect that has been used to describe many plasma phenomena, such as the self-focusing of lasers in a plasma [51], electromagnetic-electrostatic mode conversion in non-uniform plasmas [52], and density structures in the auroral ionosphere [53]. The interpretation presented here draws from Francis F. Chen's book *Introduction to Plasma Physics and Controlled Fusion* [30] and Dwight R. Nicholson's book *Introduction to Plasma*

Theory [31]. The effect is best demonstrated by considering the motion of an electron in electric and magnetic fields oscillating sinusoidally in time. The constant in time components $\mathbf{E_0}$ and $\mathbf{B_0}$ may be neglected in this derivation; it is important to note that this is done only to reduce the number of terms present as the ponderomotive force is unaffected by the presence of background electric and magnetic fields. Additionally, we may consider the particle to initially be at rest in our frame of reference, thus $\mathbf{v_0} = 0$. The equation of motion of the electron is,

$$m_e \frac{d\mathbf{v}}{dt} = -e\left(\mathbf{E} + \mathbf{v} \times \mathbf{B}\right) \tag{2.6}$$

and is evaluated for the following first order perturbations,

$$\mathbf{v} = \mathbf{v_1} \tag{2.7}$$

$$\mathbf{B} = \mathbf{B_1} \tag{2.8}$$

$$\mathbf{E} = \mathbf{E_1} = \mathbf{E_s}(\mathbf{x})\cos(\omega t) \tag{2.9}$$

where $\mathbf{E_s}(\mathbf{x})$ is the spatial variation of the amplitude of the electric fields and is not necessarily sinusoidal. After neglecting second order terms and evaluating the electric field at the initial position $\mathbf{x_0}$ the equations of motion of the electron take the form,

$$\mathbf{a_1} = \frac{d\mathbf{v_1}}{dt} = -\frac{e}{m_e}\mathbf{E_s}(\mathbf{x_0})\cos(\omega t) \tag{2.10}$$

$$\mathbf{v_1} = \frac{d\mathbf{x_1}}{dt} = -\frac{e}{m_e\omega}\mathbf{E_s}(\mathbf{x_0})\sin(\omega t) \tag{2.11}$$

$$\mathbf{x_1} = \frac{e}{m_e\omega^2}\mathbf{E_s}(\mathbf{x_0})\cos(\omega t) \tag{2.12}$$

where the $\mathbf{v_1} \times \mathbf{B_1}$ term is neglected as it is second order in nature. It can be seen that these first order perturbations result in oscillations of the electron about $\mathbf{x_0}$ at

the same frequency as the time dependent electric field oscillations. The time average over $2\pi/\omega$ of the first order equation of motion is zero and there is no net force on the particle. Since the ponderomotive force is a nonlinear force we must move to a second order solution in order to reveal its presence. A second order solution requires a first order Taylor expansion of $\mathbf{E_s}$ about $\mathbf{x_0}$,

$$\mathbf{E} = \mathbf{E_s}(\mathbf{x_0})\cos(\omega t) + (\mathbf{x_1}\cdot\nabla)\mathbf{E_s}|_{\mathbf{x_0}}\cos(\omega t) \tag{2.13}$$

and the first order magnetic field perturbation is defined by Faraday's Law,

$$\begin{aligned}\nabla\times\mathbf{E} &= -\frac{d\mathbf{B}}{dt}\\ \mathbf{B_1} &= -\frac{1}{\omega}\nabla\times\mathbf{E_s}|_{\mathbf{x_0}}\sin(\omega t)\end{aligned} \tag{2.14}$$

where the typical Taylor expansion property $\mathbf{E_s}(\mathbf{x_0}) \gg (\mathbf{x_1}\cdot\nabla)\mathbf{E_s}|_{\mathbf{x_0}}$ is used to discard the second order contribution of the electric field. The equation of motion is thus,

$$m_e\left(\frac{d\mathbf{v_1}}{dt}+\frac{d\mathbf{v_2}}{dt}\right) = -e\left[(\mathbf{E_s}+(\mathbf{x_1}\cdot\nabla)\mathbf{E_s}|_{\mathbf{x_0}})\cos(\omega t) + (\mathbf{v_1}+\mathbf{v_2})\times\mathbf{B_1}\right] \tag{2.15}$$

where we now wish to solve for the second order force term, which we will call the ponderomotive force on a single particle, $\mathbf{f_p}$. Substituting Eqs. (2.10), (2.11), (2.12), (2.13), and (2.14) into Eq. (2.15) and then taking the time average over the short time scale $2\pi/\omega$ results in,

$$\mathbf{f_p} = m_e\left\langle\frac{d\mathbf{v_2}}{dt}\right\rangle = -\frac{e^2}{m_e\omega^2}\frac{1}{2}[(\mathbf{E_s}\cdot\nabla)\mathbf{E_s}+\mathbf{E_s}\times(\nabla\times\mathbf{E_s})] \tag{2.16}$$

where $\langle ...\rangle$ indicates a time average over $2\pi/\omega$ and the substitution $\langle\cos^2(\omega t)\rangle = \langle\sin^2(\omega t)\rangle = 1/2$ has been made. The above expression is quite general and at this

point it is intuitive to discuss the simplification of Eq. (2.16) from both the electrostatic and electromagnetic cases. In the case of electrostatic perturbations the $\mathbf{E_s} \times (\nabla \times \mathbf{E_s})$ term on the right of Eq. (2.16) vanishes since the curl of $\mathbf{E}$ is zero, this is identical to repeating the original derivation with $\mathbf{B_1} = 0$. What is left can be simplified using the product rule [54],

$$\mathbf{A} \times (\nabla \times \mathbf{A}) = \frac{\mathbf{1}}{\mathbf{2}} \nabla(A^2) - (\mathbf{A} \cdot \nabla)\mathbf{A} \tag{2.17}$$

where the left hand side will again be zero due to the zero curl of the electric field leaving only $\frac{1}{2}\nabla(E_s^2) = (\mathbf{E_s} \cdot \nabla)\mathbf{E_s}$); the ponderomotive force becomes,

$$\mathbf{f_p} = -\frac{1}{4}\frac{e^2}{m_e \omega^2}\nabla E_s^2 \tag{2.18}$$

For electromagnetic perturbations the $\mathbf{E_s} \times (\nabla \times \mathbf{E_s})$ term in Eq. (2.16) does not vanish, substituting this term for the right side of the product rule in Eq. (2.17) will remove the contribution of the $(\mathbf{E_s} \cdot \nabla)\mathbf{E_s}$ term in Eq. (2.16) leaving only a $\frac{1}{2}\nabla(E_s^2)$ term, and the ponderomotive force again simplifies to Eq. (2.18). The derivation presented is only for a single electron, to extend it to the bulk plasma we may multiply by the density n_e to obtain the force per m^3,

$$\mathbf{F_p} = -\frac{\omega_{pe}^2}{\omega^2}\nabla\frac{\langle \epsilon_0 E^2 \rangle}{2} \tag{2.19}$$

where the substitution $E_s^2 = 2\langle E^2 \rangle$ has been made. In the electrostatic and electromagnetic cases the physical mechanisms behind the force are quite different even though both cases return the same outcome.

During the motion of the electron oscillating in an electrostatic wave with non-uniform spatial amplitude it will experience a larger force from spatial regions with

larger electric field than in weaker and this effect will not average to zero over an oscillation, resulting in a net drift of the particle over one oscillation. Particles will be forced into regions of low field amplitude that cannot "push back" as much resulting in a build of charge there [31].

The physical mechanism of the ponderomotive force is entirely different in the electromagnetic case though the end result is the same; it arises from the second order Lorentz force $\mathbf{v_1} \times \mathbf{B_1}$ in the direction of the wave vector, $\mathbf{k}$, since $\mathbf{E} \times \mathbf{B}$ is in the direction of $\mathbf{k}$ and $\mathbf{v_1}$ is parallel to $\mathbf{E}$. The phases of $\mathbf{v_1}$ and $\mathbf{B_1}$ are separated by $\pi/2$ and the motion along the wave vector does not average to zero over an oscillation resulting in a net drift for all particles. If there are spatial amplitude variations the magnitude of the drift will not be the same for all particles and there will be a bunching of particles in small amplitude regions [30].

In both cases, the spatial variations of the electric field result in a bunching of particles and some force, the ponderomotive, has to be responsible for the build-up of charges in high density regions. The derivation presented here was for electrons, but one can see that the ponderomotive force is proportional to the spatial gradient of the electric field as well as the density of the region and will therefore be felt by all charged particles. However, because of the mass dependence the effect is smaller for ions relative to the force on electrons by a factor of m_e/M. The ponderomotive force on the ions can often be neglected; however, the reaction of the ions to charged regions created by the ponderomotive force on electrons can be a large low-frequency effect [30, 31].

2.5 Parametric Decay

The ponderomotive force provides a mechanism for coupling between different plasma wave modes. A subset of non-linear wave-wave interactions are known as parametric

decay instabilities, and the coupled waves involved must satisfy a set of matching conditions [30]. A simple derivation of the matching conditions can be presented using harmonic oscillators a_s with resonant frequencies ω_s described by the equation of motion,

$$\frac{d^2 a_s}{dt^2} + \omega_s^2 a_s = 0 \tag{2.20}$$

2.5.1 HARMONIC OSCILLATOR COUPLING

Consider a system of three harmonic oscillators: a high frequency oscillator a_P that will be pumped by an external source, another high frequency oscillator a_H that is coupled to the pump oscillator and also to a third low frequency oscillator a_L. The equations of motion for a_L and a_H including coupling terms to the other oscillators are, respectively,

$$\frac{d^2 a_L}{dt^2} + \omega_L^2 a_L = c_L a_H a_P \tag{2.21}$$

$$\frac{d^2 a_H}{dt^2} + \omega_H^2 a_H = c_H a_L a_P \tag{2.22}$$

where c_s is the coupling constant of an oscillator and the coupling term drives oscillations of the oscillator. If we let $a_L = A_L \cos(\omega_1 t)$, $a_H = A_H \cos(\omega_2 t)$ and $a_P = A_P \cos(\omega_P t)$ where A_s is the oscillator amplitude, then substitution into Eq. (2.22) results in,

$$\begin{aligned} -\omega_2^2 A_H \cos(\omega_2 t) + \omega_H^2 A_H \cos(\omega_2 t) &= c_H A_P A_L \cos(\omega_P t)\cos(\omega_1 t) \\ (\omega_H^2 - \omega_2^2) A_H \cos(\omega_2 t) &= c_H A_P A_L \frac{1}{2}(\cos([\omega_P + \omega_1]t) + \cos([\omega_P - \omega_1]t)) \end{aligned} \tag{2.23}$$

Thus the coupling terms are capable of driving oscillations of a_H with frequency,

$$\omega_2 = \omega_P \pm \omega_1 \tag{2.24}$$

If restricting ourselves to linear interactions it is evident from the solution of Eq. (2.20) that the oscillator a_H can only oscillate at $\omega_2 = \omega_H$. However, if we extend to small non-linear interactions the oscillator a_H will have a small bandwidth over which it can resonate so that ω_2 needs only be approximately ω_H [30]. Additionally, the frequency ω_2 can have an imaginary component related to damping or growth of the oscillations. If ω_1 is small and ω_H is close to ω_P then a_H could conceivably oscillate at both $\omega_2 = \omega_P + \omega_1$ and $\omega_2 = \omega_P - \omega_1$ or else one of these frequencies will be too far outside of the bandwidth of a_2 and a single frequency will be driven. Similarly, a_L is also restricted to a small bandwidth of resonant oscillations and ω_1 must fall within this range. Given this result we can now let $a_L = A_L \cos(\omega_3 t)$ and $a_H = A_H \cos([\omega_P \pm \omega_1]t)$ and substitute into Eq. (2.21) and simplify,

$$(\omega_L^2 - \omega_3^2) = c_L A_P A_H \frac{1}{2}(\cos([2\omega_P \pm \omega_1]t) + \cos(\omega_1 t)) \tag{2.25}$$

The driven oscillations of a_H can in turn excite the original oscillation ω_1 of a_L but also oscillation frequencies of $\omega_3 = 2\omega_P \pm \omega_1$ so long as these are within the resonant bandwidth of a_L. One can see that this feedback process will go on indefinitely and we will instead restrict the resonant oscillations of a_L to be low frequency with $\omega_P > \omega_L$ so that ω_3 is non-resonant with a_L. Here we note that we have not put restrictions on a_H and we may have $\omega_H >$ or $< \omega_P$ and $\omega_H >$ or $< \omega_L$. Therefore, we have a set of three oscillations that are coupled to $a_P(\omega_P)$ by Eqs. (2.21) and (2.22): $a_L(\omega_1 \simeq \omega_L)$,

$a_H(\omega_2 = \omega_P - \omega_1 \simeq \omega_H)$, and $a_H(\omega_2 = \omega_P + \omega_1 \simeq \omega_H)$,

$$\begin{aligned}(\omega_L^2 - \omega_1^2)a_L(\omega_1) - c_L A_P[a_H(\omega_P - \omega_1) + x_H(\omega_P + \omega_1)] = 0 \\ ([\omega_H^2 - (\omega_P - \omega_1)^2]a_H(\omega_P - \omega_1) - c_H A_P a_L(\omega_1) = 0 \\ ([\omega_H^2 - (\omega_P + \omega_1)^2]a_H(\omega_P + \omega_1) - c_H A_P a_L(\omega_1) = 0\end{aligned} \tag{2.26}$$

which can be solved to yield a frequency matching condition,

$$\omega_P \approx \omega_2 \pm \omega_1 \tag{2.27}$$

so long as the frequencies ω_1 and ω_2 are approximately equal to the resonant frequencies of the oscillators $a_L(\omega_L)$ and $a_H(\omega_H)$, respectively. The coupled-oscillators scenario may be repeated using plasma waves $a_s(\mathbf{k} \cdot \mathbf{x} - \omega t)$ to yield a wavenumber matching condition [30],

$$\mathbf{k_P} \approx \mathbf{k_2} \pm \mathbf{k_1} \tag{2.28}$$

in addition to the frequency matching condition of Eq. (2.27).

2.5.2 PLASMA WAVE COUPLING

In Chapter 5 we will present 1D simulations designed to observe parametric coupling of a pumped parallel whistler wave with high and low frequency daughter waves that exist in the plasma as thermal modes. In these cases, the ion or electron acoustic wave will be the low frequency daughter wave and another whistler mode will be the high frequency daughter wave. A parallel whistler mode is a purely electromagnetic mode while ion and electron acoustic modes are electrostatic. The ponderomotive force provides a mechanism for the coupling between these different wave modes. A

pumped whistler wave will form spatial beats with the other high frequency thermal whistler modes that are present and form spatial variations in the electric field setting up a ponderomotive force equal to,

$$\begin{aligned}
\mathbf{F_P} &= \frac{\omega_{pe}^2}{\omega^2}\frac{\epsilon_0}{2}\nabla\langle(\mathbf{E_P}+\mathbf{E_H})^2\rangle \\
\mathbf{F_P} &= \frac{\omega_{pe}^2}{\omega^2}\frac{\epsilon_0}{2}\nabla\langle E_P^2 + \mathbf{2E_P}\cdot\mathbf{E_H} + E_H^2\rangle \\
\mathbf{F_P} &= \frac{\omega_{pe}^2}{\omega^2}\frac{\epsilon_0}{2}\nabla\langle 2\mathbf{E_P}\cdot\mathbf{E_H}\rangle
\end{aligned} \tag{2.29}$$

where we assume a uniform pump wave with $\langle E_P^2\rangle = 0$ and the gradient of the $\langle E_H^2\rangle$ term will be extremely small and may be discarded leaving only the cross term. The ponderomotive force will be an electrostatic force at frequency $\omega = \omega_P - \omega_H$ if $\omega_H < \omega_P$ or $\omega = \omega_H - \omega_P$ if $\omega_H > \omega_P$, that has spatial variations with wavenumber $k = k_P \pm k_H$. It is possible for the ponderomotive force to then couple to a thermal electrostatic mode at (k_L, ω_L) so long as $k \approx k_L$ and $\omega \approx \omega_L$ and form a set of three coupled waves. The oscillating ponderomotive force will drive the growth of the resonant low frequency mode which will in return drive the resonant high frequency whistler mode that supplied the original beat frequency.

This can only occur for a specific set of wave modes that obey Eqs. (2.27) and (2.28). Fig. 2.6 displays the ponderomotive beat waves for a pumped whistler mode beating with both forwards and backwards travelling whistler modes. The solid lines are the dispersion branches for a whistler wave propagating at $\theta = 0^o$ with respect to the background magnetic field when $\omega_{ce} = \omega_{pe}/3$, the black circle indicates the pumped mode. The dashed lines indicate all of the electrostatic ponderomotive beat modes that could couple to electrostatic wave modes. Had we not restricted ourselves to $\omega_L < \omega_P$ there would in theory be additional branches above ω_P predicted by

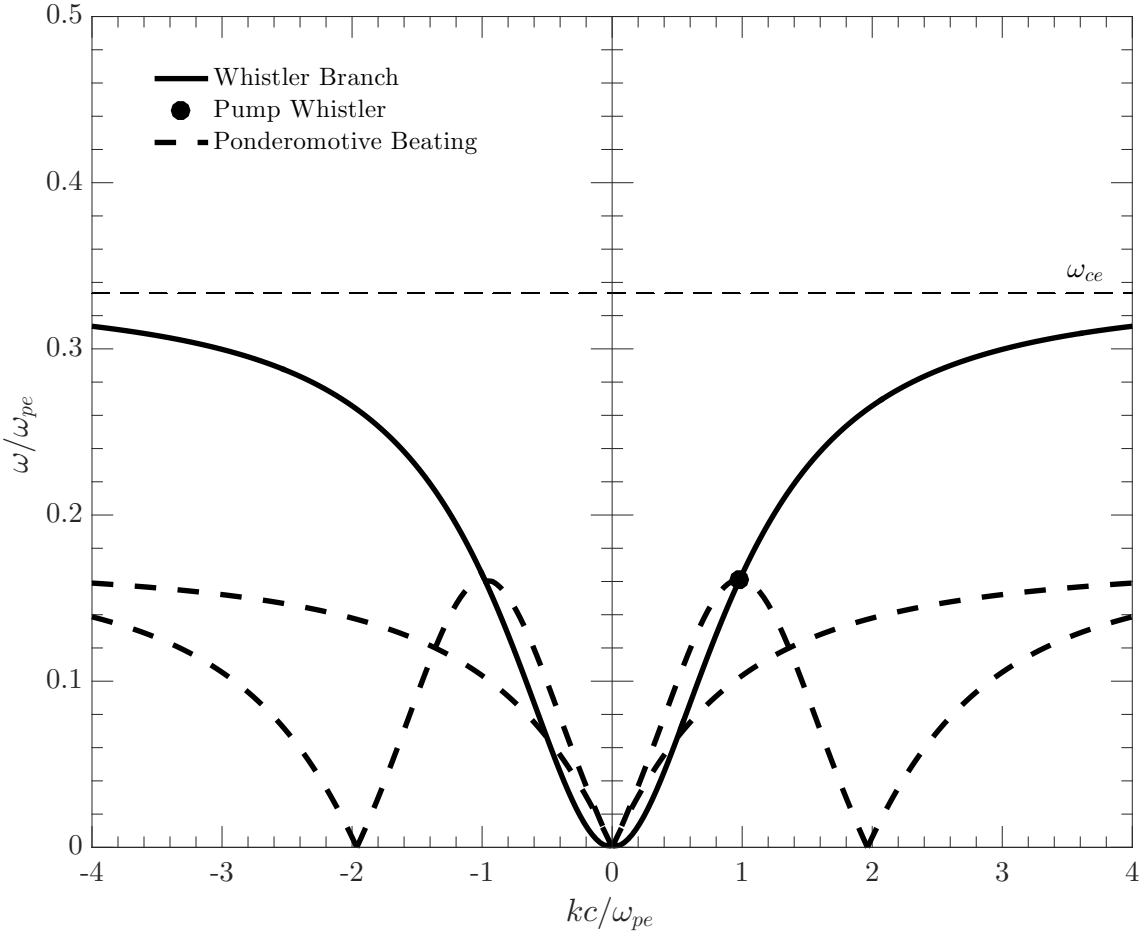

Figure 2.6: The low frequency parametric decay matching conditions for a pumped whistler beating with the rest of the whistler modes. The solid black line indicates the whistler dispersion relation for propagation parallel to a background magnetic field, the pumped whistler is highlighted by the black circle along the forward travelling whistler branch, and the $\omega_L < \omega_P$ ponderomotive beating solutions are indicated by the black dashed lines.

Eqs. (2.27) and (2.28) — in practice the ponderomotive force does not easily allow for coupling to the electrostatic branch in this regime as the $\langle E_P^2 \rangle$ term in Eq. (2.29) would not be averaged over a full oscillation. An electrostatic mode intersecting the dashed curves of Fig. 2.6 has the potential to form a three-wave coupling with the pump whistler mode and the matching mode along the whistler branch.

CHAPTER 3.

Simulation Models and Setup

3.1 Plasma Simulation

The results presented in Chapters 4 and 5 are generated using the KEMPO1 (Kyoto University ElectroMagnetic Particle cOde) Particle-in-Cell (PIC) code developed by *Omura and Matsumoto (1993)* [55], and a Darwin PIC code in the UCLA Particle-in-Cell (UPIC) Framework developed by *V.K. Decyk (2007)* [56]. PIC codes solve the particle equations of motion self-consistently with Maxwell's Equations to account for the feedback effects of the particles on the wave-fields. Both simulation codes are one-dimensional in space (x), three-dimensional in velocity space $\mathbf{v} = (v_x, v_y, v_z)$, with three-dimensional electromagnetic fields $\mathbf{E} = (E_x, E_y, E_z)$ and $\mathbf{B} = (B_x, B_y, B_z)$; it should be noted that for only a single dimension in space B_x must be a constant. Furthermore, both codes may have an imposed background magnetic field B_0 in the x-y plane that can be at any oblique angle θ with respect to x. This simulation structure is depicted in Fig. 3.1 with the external magnetic field depicted in red; the wave vector $\mathbf{k} = k_x = k$ must also be one-dimensional in a system with a single spatial dimension.

In general, PIC codes are set up as grid systems with grid spacing Δx and periodic boundary conditions; particles are able to exist anywhere in the cells and physical quantities are calculated on the grid points and then interpolated back to the particle positions to determine the forces there. In a cyclical fashion, charge density and

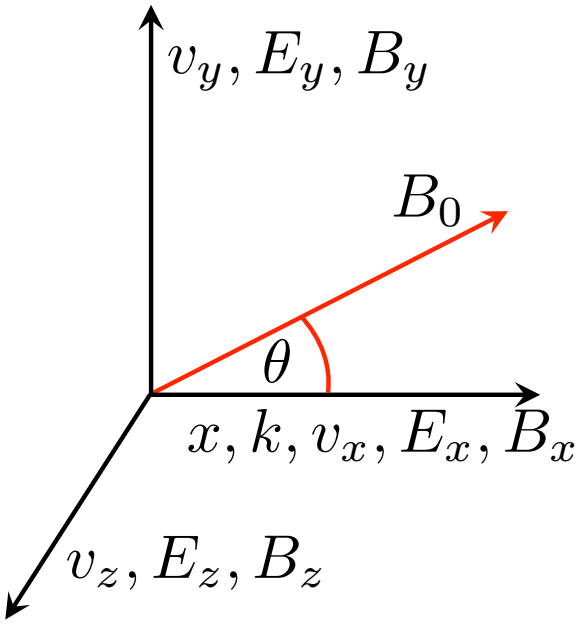

Figure 3.1: Schematic of the dimensional structure of the simulations. The code has a single spatial dimension, and is three dimensional in velocity-space and electromagnetic fields. There is the capability to align a background magnetic field B_0 at any angle θ with respect to x in the x-y plane.

current density are calculated using particle positions and velocites, these are used to calculate the electromagnetic fields at grid points and advance them in time, these updated fields are used to calculate the force at each particle location, the equation of motion is used to advance the particles in time, and the process repeats itself with the densities and fields being updated with the new particle data [57]. The charge density ρ and current density $\mathbf{J} = (J_x, J_y, J_z)$ are calculated at grid points using the particle positions and velocities [58],

$$\rho(\mathbf{x}) = \sum_i q_i S(\mathbf{x} - \mathbf{x_i}) \tag{3.1}$$

$$\mathbf{J}(\mathbf{x}) = \sum_i q_i \mathbf{v_i} S(\mathbf{x} - \mathbf{x_i}) \tag{3.2}$$

where q_i, $\mathbf{x_i}$, and $\mathbf{v_i}$ are the charge, position, and velocity of the i-th particle, re-

spectively. The function $S(\mathbf{x})$ is known as the the particle shape function, for point particles this is a delta function but it is common to use a finite size in simulations; the reason for this is to suppress numerical heating that arises from not being able to resolve particle density fluctuations smaller than the grid spacing [59, 58]. From a signals perspective, this is analogous to filtering out fluctuations above the Nyquist frequency to prevent aliasing. Calculating the charge and current densities using Eqs. (3.1) and (3.2) automatically satisfies the equation of continuity,

$$\nabla \cdot \mathbf{J} = -\frac{\partial \rho}{\partial t} \tag{3.3}$$

Alternatively, one can use Eq. (3.1) to calculate the charge density and then use Eq. (3.3) to calculate the current density; however, in a one-dimensional system this can only be used to calculate the J_x component of the current density [59]. To solve for the fields we begin by satisfying Poisson's Equation, but again in a one-dimensional system this only yields information about the E_x component of the electric field [55],

$$\begin{aligned} \nabla \cdot \mathbf{E} &= \frac{\rho}{\epsilon_0} \\ \frac{\partial E_x}{\partial x} &= \frac{\rho}{\epsilon_0} \end{aligned} \tag{3.4}$$

where ϵ_0 is the permittivity of free space; in some codes it is necessary to only explicitly satisfy Eq. (3.4) initially, or it can be used to calculate E_x each iteration. A similar equation holds for the magnetic field component B_x,

$$\begin{aligned} \nabla \cdot \mathbf{B} &= 0 \\ \frac{\partial B_x}{\partial x} &= 0 \end{aligned} \tag{3.5}$$

and requires that B_x be constant in space. The electric fields $\mathbf{E} = (E_x, E_y, E_z)$ (if not explicitly solving for E_x with Eq. (3.4)) and magnetic fields $\mathbf{B} = (B_y, B_z)$ are found by solving,

$$\nabla \times \mathbf{B} = \mu_0 \mathbf{J} + \frac{1}{c^2} \frac{\partial \mathbf{E}}{\partial t} \tag{3.6}$$

$$\nabla \times \mathbf{E} = -\frac{\partial \mathbf{B}}{\partial t} \tag{3.7}$$

where μ_0 is the magnetic permeability of free space. Eq. (3.7) also shows us that B_x must be constant in time in addition to constant across space in a one-dimensional code. There are various numerical methods for solving the system of equations defined by Eqs. (3.4)–(3.7) and advancing the fields in time; the different methods employed by each of the codes used will be briefly discussed in the next sections. Once the fields have been advanced in time the fields are interpolated back to each particle position so the Lorentz force on each particle can be found. The interpolation method employed by both the KEMPO1 and UPIC Darwin codes is a linear interpolation.

The electron equation of motion is given by Eq. (2.6) and is displayed again for reference,

$$m_e \frac{d\mathbf{v}}{dt} = -e \left(\mathbf{E} + \mathbf{v} \times \mathbf{B} \right)$$

For relativistic dynamics m and $\mathbf{v}$ in the equation of motion are modified by the Lorentz factor [59],

$$\gamma = \frac{1}{\sqrt{1 - \left(\frac{v^2}{c^2}\right)}} \tag{3.8}$$

where $m = \gamma m_0$ and m_0 is the mass of the particle at rest and $\mathbf{u} = \gamma \mathbf{v}$ defined by,

$$\mathbf{u} = \frac{c}{\sqrt{c^2 - |\mathbf{v}|^2}} \mathbf{v} \tag{3.9}$$

yields a solution for $\mathbf{v}$,

$$\mathbf{v} = \frac{c}{\sqrt{c^2 + |\mathbf{u}|^2}} \mathbf{u} \tag{3.10}$$

where $\mathbf{u} = (u_x, u_y, u_z)$ is the particle momentum per unit mass. The particles are advanced in time according to the equation of motion using what is called a particle pusher — an algorithm that advances the particles a discrete step Δt while conserving energy and momentum to a small degree of error. Both the KEMPO1 and UPIC Darwin codes use the most common algorithm known as the Boris Method; readers interested in the details of the Boris particle pushing method should look in any introductory plasma physics simulation textbook such as *Plasma Physics via Computer Simulation* by C.K. Birdsall and A.B. Langdon [57]. The method amounts to initially advancing particles half a time step $\Delta t/2$ using only the electric field, followed by a rotation in space about the magnetic field from the $\mathbf{v} \times \mathbf{B}$ force, and finally advancing another $\Delta t/2$ using only the electric field [58]. The use of the Boris method strictly conserves energy and momentum during cyclotron motion [59]. We next discuss some of the inner workings of each code and the setup for the simulation results presented in Chapters 4 and 5.

3.2 KEMPO1

3.2.1 CODE STRUCTURE

The KEMPO1 code is a fully relativistic electromagnetic particle code written in MatLab that uses the Finite Difference Time Domain (FDTD) method for solving Maxwell's equations [55, 59]; the method was first presented by *Yee (1966)* [60]. The FDTD method discretizes space to two grid systems, one on full-integer steps $l\Delta x$ and the other on half-integer steps $(l + 1/2)\Delta x$ where $(l = 1, 2, 3...N_x)$ and N_x is the number of grid points. The KEMPO1 code defines E_y, B_y, J_y, and ρ on the full-integer grid and E_x, J_x, E_z, B_z, and J_z on the half-integer grid. Derivatives in Maxwell's equations are instead performed as central difference approximations, for example the initial E_x calculated using Eq. (3.4) becomes,

$$\frac{E_x(l + 1/2) - E_x(l + 1/2)}{\Delta x} = \frac{\rho(l)}{\epsilon_0} \tag{3.11}$$

where the spatial derivative of $E_x(l)$ is approximated using a full-integer step centred at location l and one never requires actually knowing $E_x(l)$ when satisfying the condition. The quantities are also updated on full and half-integer temporal grids $j\Delta t$ and $(j + 1/2)\Delta t$ where $(j = 1, 2, 3...N_t)$ and N_t is the number of time steps. The same quantities on the full-integer and half-integer spatial grids exist on the full-integer and half-integer temporal grids, respectively. Again, as an example one component of Eq. (3.6) becomes,

$$\frac{B_y(l + 1, j) - B_y(l, j)}{\Delta x} = \mu_0 J_z + \frac{1}{c^2}\frac{E_z(l + 1/2, j + 1/2) - E_z(l + 1/2, j - 1/2)}{\Delta t} \tag{3.12}$$

and we note that all derivatives are calculated at the location and time $(l + 1/2, j)$ but we need not know any quantity explicitly at that point except J_z which is easily approximated there using,

$$J_z(l + 1/2, j) = \frac{J_z(l + 1/2, j + 1/2) + J_z(l + 1/2, j - 1/2)}{2} \tag{3.13}$$

Using Eq. (3.12) an expression for $E_z(l + 1/2, j + 1/2)$ can be found in terms of quantities all known previously in time. Similarly, the whole set of centred difference forms of Maxwell's equations can be solved for solutions of some quantities advanced on half integer grids and others on full integer grids, in both space and time; this gives rise to the FDTD method being commonly referred to as the "leap-frog" method. In practice, a code using the FDTD method does not explicitly contain half-integer grids, the concept remains the same so long as the half-integer set is updated before the full-integer set in the beginning and each time step thereafter. Approximating the derivatives as centred differences with a finite resolution introduces a requirement on the size of the space and time step lengths such that the fastest travelling information must be resolved, which in the electromagnetic case is the speed of light,

$$\frac{\Delta x}{\Delta t} > c \tag{3.14}$$

this is known as the Courant condition or Courant-Freidrichs-Lewy (CFL) condition after their 1928 paper outlining this restriction on finite difference solutions to hyperbolic partial differential equations [61]. In summary, the KEMPO1 code calculates the charge and current densities through a weighting of the particle locations and velocities using Eqs. (3.1) and (3.2), then uses the FDTD method to solve Maxwell's equations and advance the **E** and **B** fields in time, then the fields are interpolated

back to the particle locations, and finally the particles are advanced in time using a Boris mover.

3.2.2 Simulation Setup

The KEMPO1 code is used to investigate the properties of oblique whistler waves and these results are contained in Chapter 4. To begin these investigations we use a set of initial perturbations to generate a whistler wave propagating obliquely with respect to a background magnetic field that is consistent with Eq. 2.1. At this point we adopt the following normalizations,

$$\begin{aligned} t &\to \omega_{pe} t, & \omega &\to \frac{\omega}{\omega_{pe}}, & x &\to \frac{\omega_{pe}}{c} x \\ n &\to \frac{n}{n_o}, & \omega_{ce} &\to \frac{\omega_{ce}}{\omega_{pe}}, & k &\to \frac{ck}{\omega_{pe}} \end{aligned} \tag{3.15}$$

The initial conditions of the pertubation are similar to those used in *Yoon (2011)* [19] but have been adapted to fit the set of normalizations presented above. Perturbations are applied to the density n_e, each of the particle velocity components (v_x, v_y, v_z), all three electric field components (E_x, E_y, E_z), and the transverse components of the magnetic field (B_y, B_z) and are given by,

$$n_e = 1 + \frac{k}{c\omega} v_x \tag{3.16}$$

$$v_x = \frac{c\omega^2 \omega_{ce}^2 \eta \tan\theta}{(\omega^2 - 1)} \left(\cos\theta - \frac{\omega\eta}{\omega_{ce}(\chi - N^2)} \right) \Delta_M \sin(kx) \tag{3.17}$$

$$v_y = \omega c \eta \left(\frac{\omega^2 - \omega_{ce}^2 \sin\theta - 1}{\cos\theta(\omega^2 - 1)} + \frac{\omega_{ce}\eta}{\omega(\chi - N^2)} \right) \Delta_M \sin(kx) \tag{3.18}$$

$$v_z = \frac{\omega \omega_{ce} c \eta}{\cos\theta} \left(\cos\theta + \frac{\omega\eta}{\omega_{ce}(\chi - N^2)} \right) \Delta_M \cos(kx) \tag{3.19}$$

$$E_x = \frac{\sin\theta}{c(\omega^2 - 1)} \Delta_M v_z \tag{3.20}$$

$$E_y = \Delta_M \cos(kx) \tag{3.21}$$

$$E_z = -\frac{\eta}{\chi - N^2}\Delta_M \sin(kx) \tag{3.22}$$

$$B_y = -\frac{k}{\omega}E_z \tag{3.23}$$

$$B_z = \frac{k}{\omega}E_y \tag{3.24}$$

$$N^2 = \chi + \frac{\omega_{ce}^2(1-\chi)\sin^2\theta}{2(\omega^2-1)}\left(1 + \sqrt{1 + \frac{4\cos^2\theta}{\sin^4\theta}\frac{(\omega^2-1)^2}{\omega^2\omega_{ce}^2}}\right) \tag{3.25}$$

$$\chi = 1 - \frac{(\omega^2-1)}{\omega^2(\omega^2-\omega_{ce}^2) - (\omega^2 - \omega_{ce}\cos^2\theta)} \tag{3.26}$$

$$\eta = \frac{\omega_{ce}}{\omega}\cos\theta(1-\chi) \tag{3.27}$$

where θ is again the angle of propagation with respect to the background magnetic field and Δ_M is used to scale the magnitude of the perturbation. In the current study we choose to investigate whistler waves that are propagating at oblique angles $\theta = 30^o$ and $\theta = 70^o$. These angles are consistent with the range of angles for observed oblique whistlers. Fig. 3.2 shows the dispersion relation curves for $\theta = 30^o$ and $\theta = 70^o$ with the perturbed modes highlighted by a black dot.

Two mobile electron species are loaded into the simulator, a self-consistent species and a non-interacting species. Charge neutrality is conserved using a fixed positive background plasma. The self-consistent species interacts with the wave fields and contains the feedback effects of the particles on the wave; it is initially perturbed according to Eqs. (3.16)–(3.19). The non-interacting species responds to the electromagnetic fields but does not contain feedback effects on the wave. It has the same initial perturbation conditions as the self-consistent species. The number of particles used for each electron species is $N_p = 4096$.

The normalized parameters of the system are chosen to be $\omega_{ce}/\omega_{pe} = 1/3$ and $c/\omega_{pe} = 10$. The number of grid points was chosen to be $N_x = 256$ with spacing $\Delta x = 1$ and a time step of $\Delta t = 0.04$ to satisfy the Courant condition of Eq. (3.14).

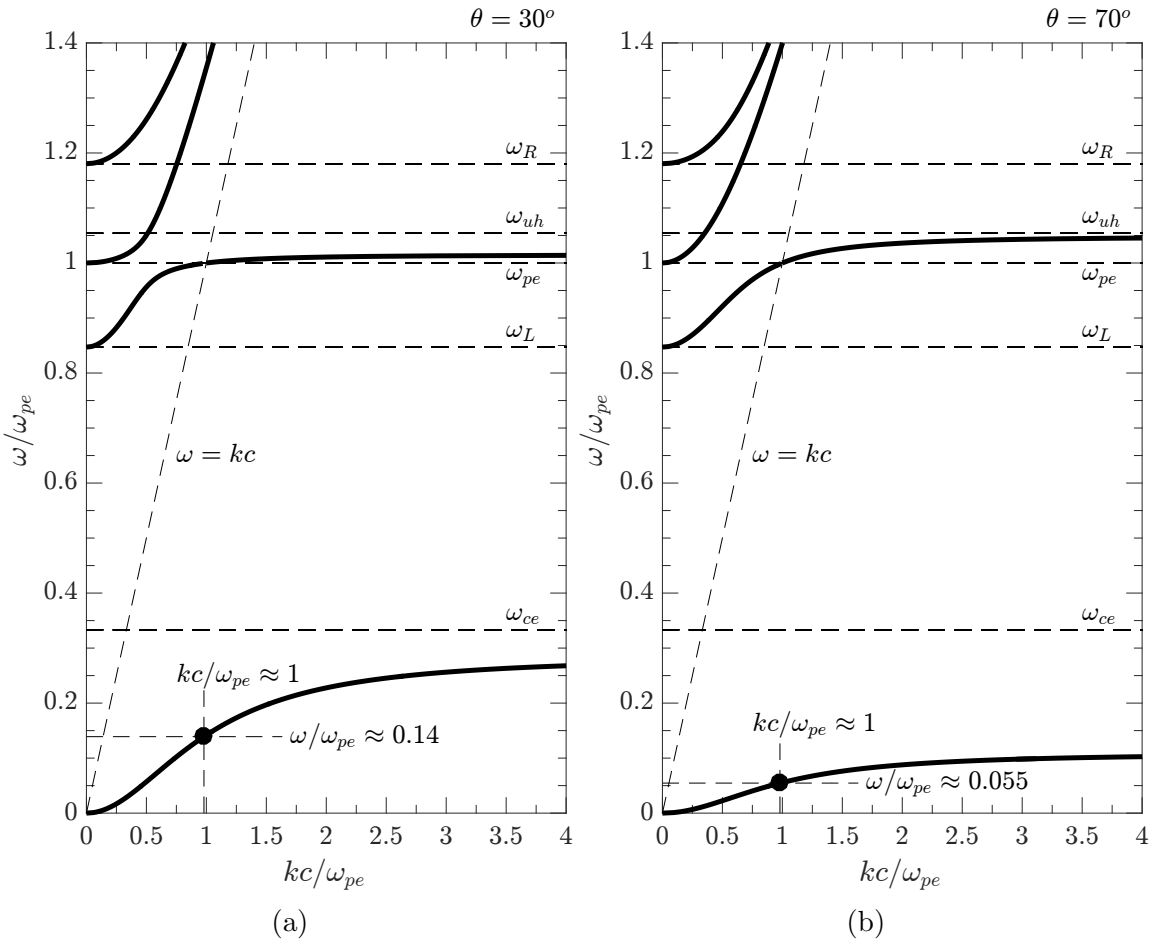

Figure 3.2: The modes of the oblique whistler branch perturbed using the initial conditions of Eqs. (3.16)–(3.27) (a) Waves propagating at an angle $\theta = 30^o$ with respect to the background magnetic field. (b) Waves propagating at an angle $\theta = 70^o$ with respect to the background magnetic field.

The KEMPO1 particle code is adapted to incorporate the initial conditions expressed earlier in Eqs. (3.16)–(3.27). The electromagnetic fields and particle velocities are assigned using Eqs. (3.17)–(3.27). Application of the initial condition for the density profile defined by Eq. (3.16) requires a non-uniform particle loading. The initial particle positions are loaded according to the prescribed density profile $n_e(x)$ from

the inversion [57],

$$\frac{i}{N_p} = \frac{\int_{x_{min}}^{x_i} n_e(x)\,\mathrm{d}x}{\int_{x_{min}}^{x_{max}} n_e(x)\,\mathrm{d}x} \tag{3.28}$$

where again i is the particle index, N_p is the number of particles, x_i is the position of particle i, and $n_e(x)$ is the density profile given by Eq. (3.16). $n_e(x)$ is put in the following useful form,

$$n_e(x) = 1 + \gamma \sin(kx), \qquad \gamma = \frac{k}{c\omega}\frac{c\omega^2\omega_{ce}^2\eta\tan\theta}{(\omega^2-1)}\left(\cos\theta - \frac{\omega\eta}{\omega_{ce}(\chi - N^2)}\right)\Delta_M$$

Carrying out the integration in Eq. (3.28) yields,

$$\frac{i}{N_p} = \frac{(x_i - x_{min}) + \gamma(\cos(kx_{min}) - \cos(kx_i))}{(x_{max} - x_{min}) + \gamma(\cos(kx_{min}) - \cos(kx_{max}))} \tag{3.29}$$

The position x_i of each particle is solved numerically and used to load each particle such that the initial density matches the density profile in Eq. (3.16).

We now discuss the selection of the wave number and frequency for the initial conditions. It is necessary to perturb the system at an integer mode number n because of the selection of periodic boundary conditions. The wave number is defined to be, $k = \frac{2\pi}{\lambda} = \frac{2\pi n}{N_x} = 0.09817$ where we choose $n = 4$. This gives a normalized wave number $\frac{kc}{\omega_{pe}} = k\frac{10}{1} = 0.9817$. The frequency of the perturbation is determined by the Appleton-Hartree equation, Eq. (2.1), for the chosen wave number. The corresponding frequencies for $\theta = 30^o$ and $\theta = 70^o$ are $\omega \approx 0.14\omega_{pe}$ and $\omega \approx 0.055\omega_{pe}$, respectively. We refer again to Fig. 3.2 where these perturbed modes are highlighted on the whistler branch. The value of $n = 4$ was chosen to make the normalized wave number ≈ 1. At this wave number the whistler branch is relatively steep and this

makes the wave perturbation easier to generate from initial conditions.

3.3 UPIC Darwin Code

3.3.1 Code Structure

The second code is constructed using the UPIC Framework and is known as a Darwin code, as it uses the Darwin subset of Maxwell's equations. The Darwin subset is identical to the standard set of Maxwell's equations except for a modification to Ampere's Law, Eq. (3.6) instead becomes,

$$\nabla \times \mathbf{B} = \mu_0 \mathbf{J} + \frac{1}{c^2} \frac{\partial \mathbf{E_L}}{\partial t} \tag{3.30}$$

where $\mathbf{E_L}$ indicates the longitudinal component of the electric field with respect to the direction of propagation of electromagnetic waves, i.e. E_x. The modification of the displacement current only coming from the longitudinal component of the electric field has the result that the high frequency ($\omega > \omega_{pe}$) electromagnetic light wave (R, L) branches are eliminated. For the present study, we are not concerned with these branches of the electromagnetic dispersion relation and can safely exclude them. Additionally, the Darwin subset are elliptical partial differential equations and have the benefit of not being restricted by the Courant condition in Eq. (3.14) and the time step needs only resolve the highest frequency, often plasma oscillations. Thus the Darwin code can use time steps that are an order of magnitude larger than what would otherwise be necessary in a full electromagnetic code (such as KEMPO1) — significantly cutting down on computation time. The Darwin code may be used to simulate very large numbers of both electron and ion species in a relatively short time compared to the KEMPO1 code.

The UPIC framework uses a spectral method for solving the Darwin subset, mean-

ing Fast Fourier Transforms (FFT) are employed to solve the system of equations defining the electromagnetic fields in a spatial gridless fashion in Fourier space and are only discretized in real space when assigned to a grid prior to using a Boris mover on the particles [58]. Advancing the fields in time requires an iterative solution as the transverse electric fields in the Darwin subset depend on the force on each particle, but the force on each particle depends on the fields so the FDTD method cannot be used. The iterative solution to this large set of coupled equations converges in only a few iterations so long as density perturbations do not become too extreme [58]. In summary, the UPIC Darwin code calculates the charge and current densities and then transforms them from real space to Fourier space using the FFT, the Darwin subset of Maxwell's equations are solved and advanced in time using an iterative method in Fourier space and then assigned to a grid in real space before the particles are advanced using a Boris mover.

3.3.2 SIMULATION SETUP

The UPIC Darwin code is used to investigate wave-wave coupling of parallel whistler wave modes through the ponderomotive force; these results are presented in Chapter (5). The idea is to pump a parallel whistler mode at a single wave number and frequency (k_P, ω_P) in the presence of electrostatic modes to see if a parametric decay process is easily mediated by the ponderomotive force created by beating whistler modes as depicted in Fig. 2.6. In discussing the setup and results we adopt a set of dimensionless normalizations,

$$\begin{aligned} t &\to \omega_{pe} t, & n &\to \frac{n}{n_o}, & x &\to \frac{x}{\Delta x} \\ \omega &\to \frac{\omega}{\omega_{pe}}, & m &\to \frac{m}{m_e}, & v &\to \frac{v}{\omega_{pe}\Delta x} \end{aligned} \tag{3.31}$$

where the grid spacing is related to the dimensionless thermal velocity by $v_{te} \rightarrow v_{te}/\omega_{pe}\Delta x$. The plasma parameters are selected to be $\omega_{ce} = \omega_{pe}/3$ with B_0 along B_x and $c/\omega_{pe} = 10$. The main modification to the original code written by V.K. Decyk was to enable the external pumping of transverse electric fields. Wave pumping or driving is accomplished by adding sinusoidal wave fields each iteration to the pre-existing fields; the amplitude is slowly increased as the system responds to the external pump and if done correctly the wave will continue to propagate once the pump is turned off. The code supported a longitudinal external wave driver already and it was a simple modification to add sinusoidal fields to the transverse components instead. In order to launch a whistler wave the external pump needs to be right-hand circularly polarized and the external wave fields added to the self-consistent fields are,

$$E_{Pz} = E_P(t)\cos(k_P x - \omega_P t) \tag{3.32}$$

$$E_{Py} = E_P(t)\sin(k_P x - \omega_P t) \tag{3.33}$$

in all simulations $E_P(t)$ increases linearly until $\omega_{pe}t = 100$ when it is then turned off. It is not necessary to perturb the transverse magnetic fields and velocities as the system will respond each iteration to the pumped electric fields and set up the necessary conditions for the wave to continue propagating. Additionally, since a parallel whistler mode has no longitudinal component the particles may be loaded uniformly. Three different cases were investigated with this wave pumping setup: a single electron species with no moving ions, a single electron species with a moving ion species, and two electron species at different temperatures and densities with no moving ions. The purpose of these cases is to investigate the result of whistlers beating with the pump wave when no electrostatic modes intersect the ponderomotive beating branches, when ion acoustic waves intersect, and when both electron acoustic

modes intersect. A parametric wave-wave coupling can be expected to occur wherever an electrostatic branch intersects the ponderomotive branches.

The time step in all simulations is $\Delta t = 0.2\omega_{pe}t$ and vary from $N_t = 5000 - 10000$ steps. A system of length $N_x = 512$ and is used for the single electron and single ion species runs with $N_{pi} = N_{pe} = 1.8432 \times 10^5$ particles where N_{pe} and N_{pi} are the total number of electrons and ions, respectively. To ensure the ion acoustic wave is undamped we use a ratio of the electron temperature to the ion temperature of $T_e/T_i = 100$ with a mass ratio $M/m_e = 16$. The other two cases use $N_{pi} = N_{pe} = 3.6864 \times 10^6$ particles and a system length of $N_x = 2048$. In runs using two electron species at different temperatures we have $N_{pc} = 0.1N_{pe}$ and $N_{ph} = 0.9N_{pe}$ giving $N_{pc} + N_{ph} = N_{pe}$ where N_{ph} and N_{pc} refer to the hot and cold electron populations, respectively. This increase in particles and system length is necessary to create a condition where the electron acoustic mode is undamped with sufficient resolution. Similar to the KEMPO1 code, we wish to generate a whistler wave with a wave number corresponding to an integer mode number of the system. We choose to generate the same mode at $kc/\omega_{pe} \approx 1$; this corresponds to $n = 8$ and $n = 32$ for $N_x = 512$ and $N_x = 2048$, respectively, and a frequency of $\omega \approx 0.16\omega_{pe}$ according to Eq. (2.1).

CHAPTER 4.

Oblique Whistler Wave Dynamics

4.1 Wave Evolution

In this chapter we present results from modelling oblique whistler waves using the KEMPO1 PIC code. To begin we confirm that the initial conditions correctly excite the whistler branch of the dispersion relation shown in Fig. 3.2. To better illustrate some of the nonlinear characteristics of the wave the amplitudes of the perturbations are made arbitrarily large in the following figures. Fig. 4.1 shows the time evolution of the B_y component of the magnetic field in position space when subject to the initial perturbations at both $\theta = 30°$ and $\theta = 70°$ in Fig. 4.1a and Fig. 4.1b, respectively. The wave paths through space and time are consistent with the phase velocity given by the values of ω and k used in the initial conditions. This is also the case for B_z, E_y, E_z, v_y, and v_z.

Along the x component we see the initial conditions perturb a second wave along with the longitudinal component of the oblique whistler wave. Fig. 4.2 is the space-time evolution the E_x component of the electric field at $\theta = 30^o$ and $\theta = 70^o$. Clearly depicted is a wave travelling at the whistler wave phase velocity along with another longitudinal mode moving in and out of phase with the whistler. Analysis of the phase velocity of the second longitudinal wave yields that it is consistent with a Langmuir wave. It is somewhat unsurprising that an initial sinusoidal perturbation to the density would have this outcome. In Fig. 4.2b at $\theta = 70°$ the Langmuir and whistler

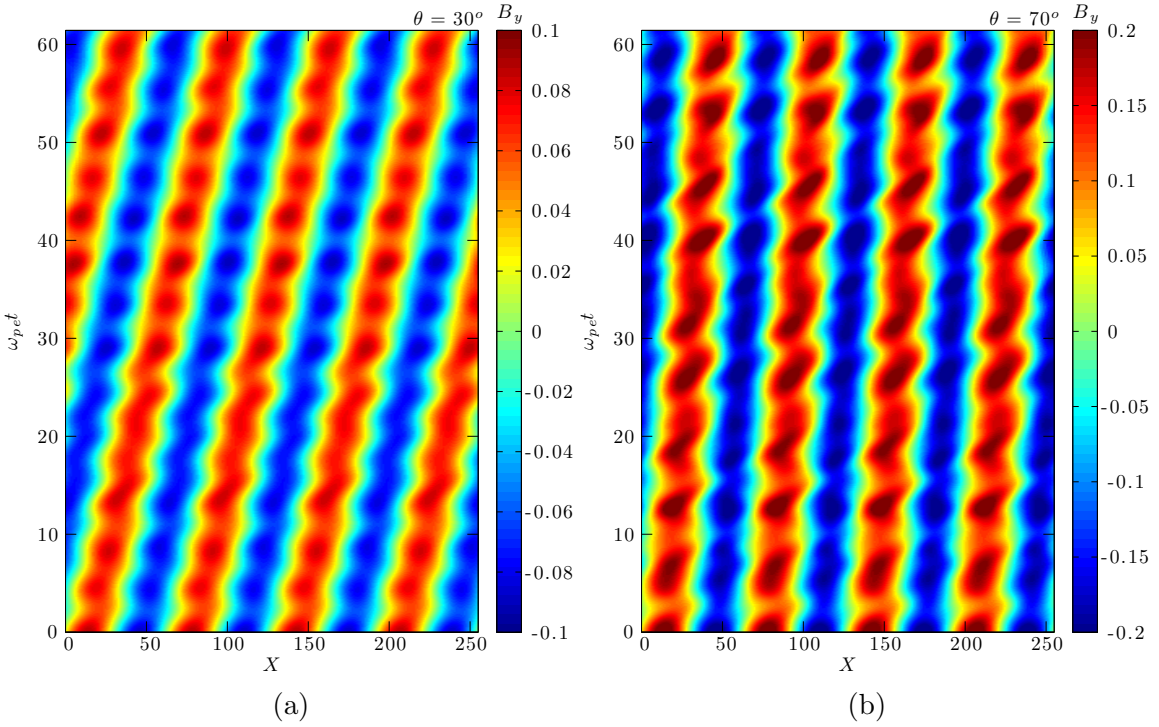

(a) (b)

Figure 4.1: Space-time diagrams of the y component of the magnetic field for (a) $\theta = 30^o$ and (b) $\theta = 70^o$. The phase velocity of the waveforms is consistent with the ratio of ω/k on the whistler branch of the dispersion relation at $kc/\omega_{pe} \approx 1$ as expected.

wave are at nearly the same amplitude, evident by the field amplitude being close to zero during the periods of anti-phase propagation. For less oblique propagation at $\theta = 30°$ the Langmuir wave dominates over the longitudinal component of the whistler wave as seen in Fig. 4.2a.

Fig. 4.3 illustrates the time evolution of the E_x component of the electric field in k-space when subject to the perturbations at angles $\theta = 30°$ and $\theta = 70°$. At $kc/\omega_{pe} = 0.9817$ the field is relatively strong at all times as expected. As time progresses the field grows in strength at exact integer multiples of the wave number used in the perturbation. These harmonics seen in k-space are a consequence of the wave steepening. It should be noted that more harmonics are present at angle $\theta = 70°$

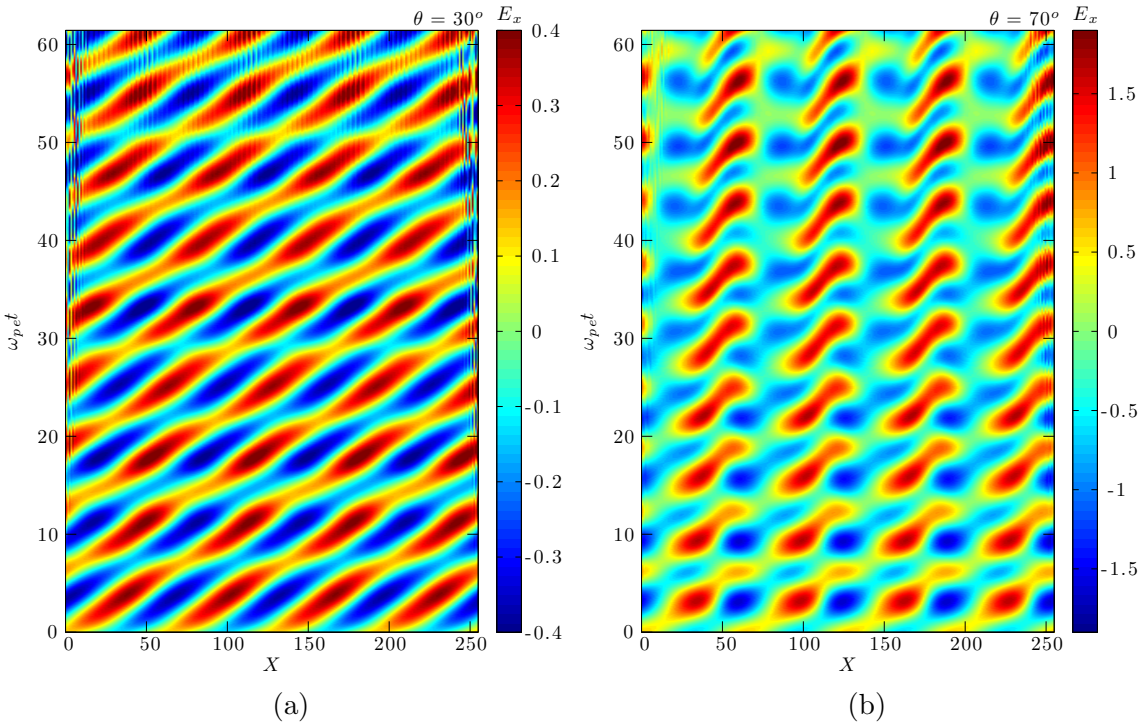

Figure 4.2: Space-time diagrams of the x-component of the electric field for (a) $\theta = 30^o$ and (b) $\theta = 70^o$. The initial conditions perturb the longitudinal component of the whistler wave along with Langmuir waves of the same mode number. The phase velocity of each mode is consistent with what is expected at $kc/\omega_{pe} \approx 1$. At $\theta = 30^o$ the Langmuir oscillations have a larger amplitude than the whistler component while at $\theta = 70^o$ the two waves have nearly identical amplitude as seen by the superposition when the waves are in anti-phase.

in Fig. 4.3b than at angle $\theta = 30°$ in Fig. 4.3a. Fig. 4.4 displays different time stages of the density profile for the self-consistent particles when the large perturbation is applied at oblique angles $\theta = 30°$ and $\theta = 70°$. It is important to note that the steepening seen here is more pronounced and occurs over a shorter time than the steepening seen at a perturbation amplitude that generates waves with amplitudes more consistent with observations. The wave steepens faster and is more nonlinear in Fig. 4.4b than in Fig. 4.4a. This outcome is consistent with the harmonic generation differences of 4.3. The wave steepening is more pronounced at more oblique angles and thus more harmonics are generated as a consequence.

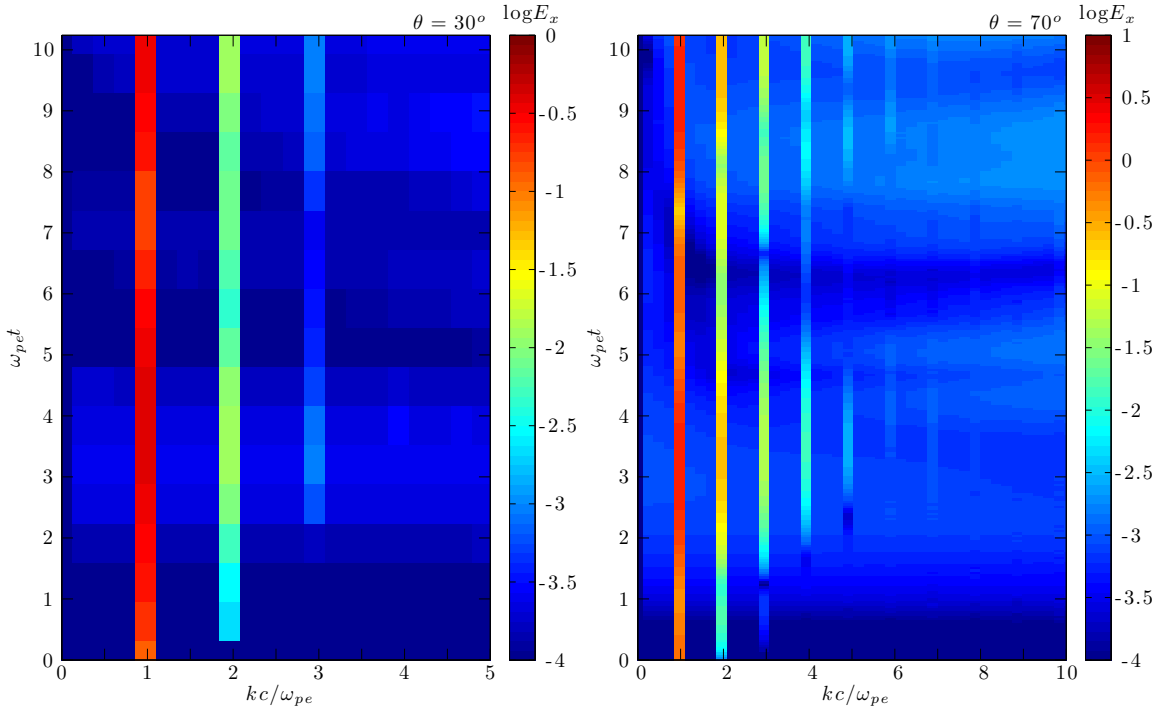

(a) (b)

Figure 4.3: Fourier analysis in space at each time step displays the generation of wave number harmonics in the x component of the electric field due to wave steepening. (a) At $\theta = 30°$ the second and third harmonics have a significant amplitude before a single Langmuir oscillation ($\omega_{pe}t = 2\pi$) has occurred. (b) At $\theta = 70°$ harmonics up to and including the fifth harmonic have a significant amplitude above the background.

It is confirmed that the initial conditions correctly excite the whistler branch of the dispersion relation shown in Fig. 3.2. In addition to the whistler branch the oblique propagation results in a coupling with the Langmuir branch of the dispersion relation, exciting a wave with a frequency very close to the plasma frequency and wave number identical to the whistler. The large amplitude compressional component causes the waves to steepen over time; this is more pronounced as the propagation angle becomes more oblique. Here we make note of the small edge instabilities in Fig. 4.2 and Fig. 4.4 that appear at all angles and perturbation amplitudes. These are considered to have a negligible effect on the simulation. An effort was made to remove these instabilities,

with no success, and they arise from a small discontinuity in the initialization of the density profile at the boundary.

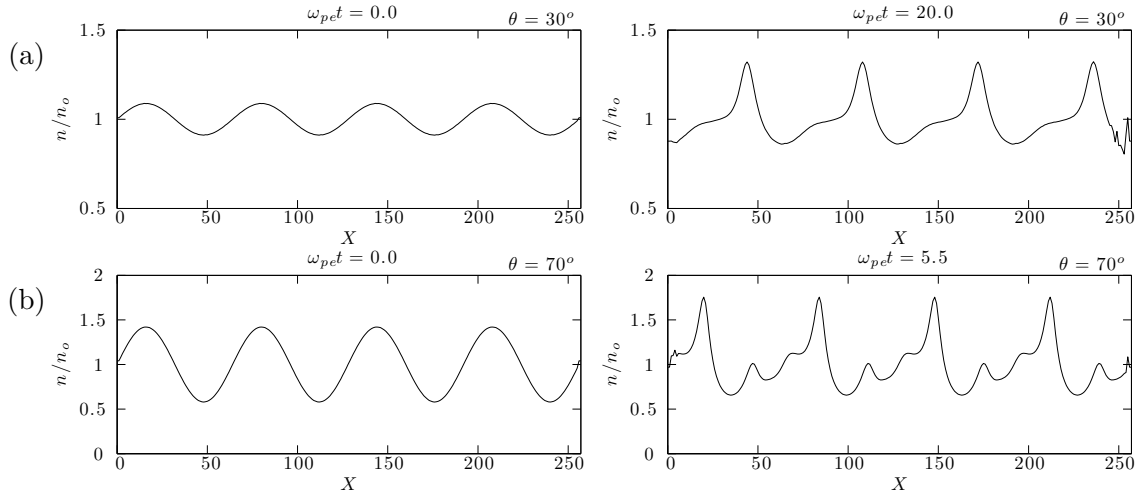

Figure 4.4: Illustration of wave steepening in the density profile for oblique whistler waves at an arbitrarily large wave amplitude. (a) Density profile at $\theta = 30°$ for the initial waveform and after steepening at $\omega_{pe}t = 20.0$. (b) Density profile at $\theta = 70°$ for the initial waveform and after steepening at $\omega_{pe}t = 5.5$.

4.2 Nonlinear Wave-Particle Interactions

4.2.1 Wave Breaking

A consequence of wave steepening is that the wave can eventually reach a point where it breaks, a nonlinear phenomena analogous to the white caps seen when ocean waves break. A wave breaking event is shown in Fig. 4.5 for the x component of the electric field and particle velocity. The electric field in Fig. 4.5a has a sharp decrease in magnitude at the same position as a vortical structures in the phase space plot of Fig. 4.5b. Wave breaking events were observed at a propagation angle of $\theta = 70^o$ down to $\theta = 45^o$ but at less oblique angles the wave steepening effects were not large enough to cause breaking even at very large perturbation amplitudes.

The steepening time until the first breaking event, $\omega_{pe}t_s$, decreases as the initial

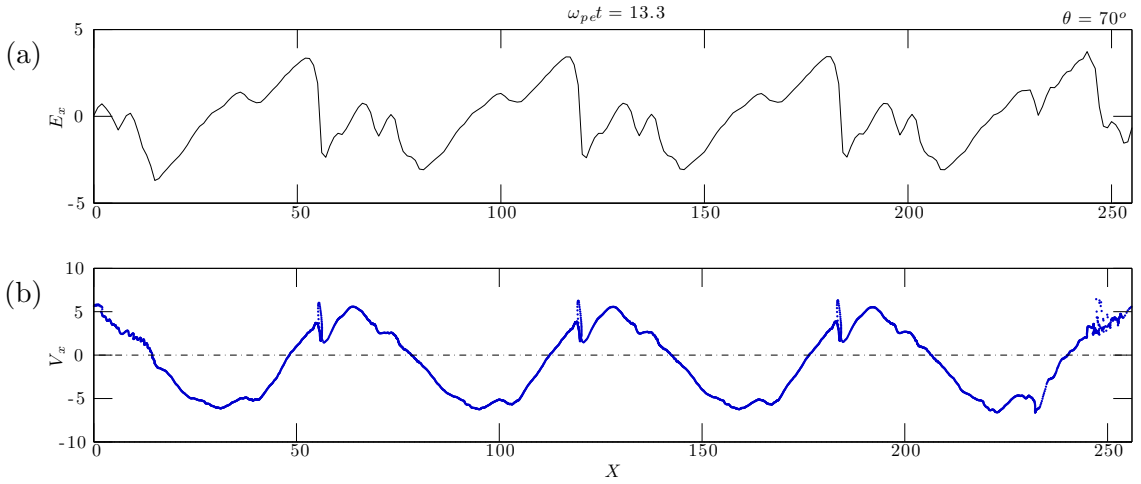

Figure 4.5: Wave breaking event for an arbitrarily large amplitude wave at $\theta = 70°$. (a) The x component of the electric field. (b) The x component of the self consistent particle velocities, a breaking structure occurs at the same position as the steepest part of the electric field.

amplitude of the wave increases. This steepening time follows an inverse power law with the strength of the magnetic perturbation, and is depicted in Fig. 4.6. The amplitudes measured in Fig. 4.6 range from $\delta B/B_0 \sim 0.3 - 1.0$ and are outside the range of observed whistler wave amplitudes in the Earth's radiation belts; at more realistic amplitudes of $\delta B/B_0 \sim 0.01 - 0.1$ the wave breaking time is very long and it is not practical to track these events in the simulation. However, we can use the relationship between the steepening time and wave amplitude to estimate the steepening time for amplitudes consistent with observed whistler waves; this is discussed in Section 4.3.

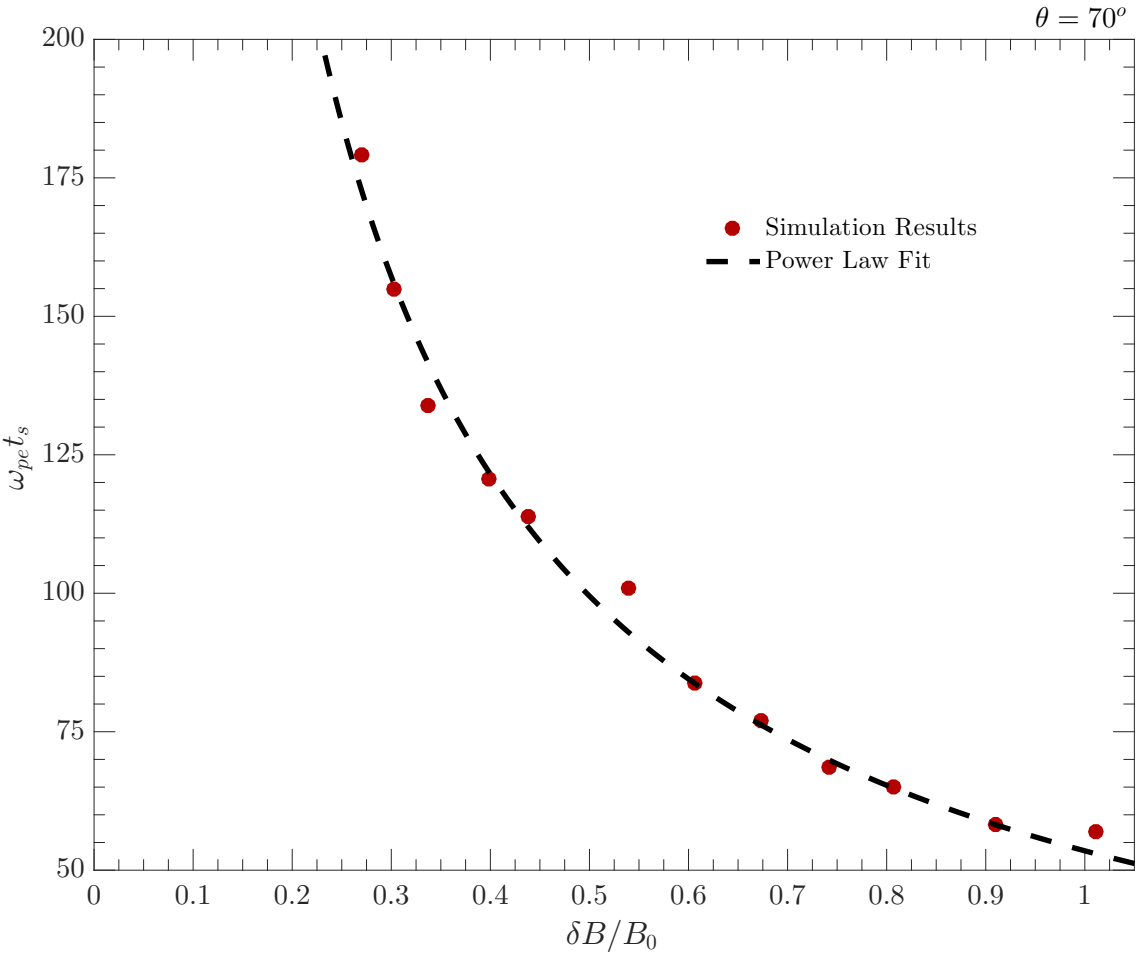

Figure 4.6: Wave breaking time, $\omega_{pe} t_{Br}$, as a function of the initial amplitude of the y-component of the magnetic field for $\theta = 70°$.

4.2.2 Particle Trapping and Wave Damping

At all amplitudes the system eventually begins to exhibit particle trapping by the wave when the angle of propagation is $\theta = 70^o$. Fig. 4.7 displays the trajectories of two particles trapped in a wave propagating at an oblique angle of $\theta = 70°$. The trajectory for the first particle is in Fig. 4.7a and it's corresponding phase space evolution is displayed in Fig. 4.7b. Similarly, the trajectory and phase space evolution of the second particle are shown in Fig. 4.7c and Fig. 4.7d, respectively.

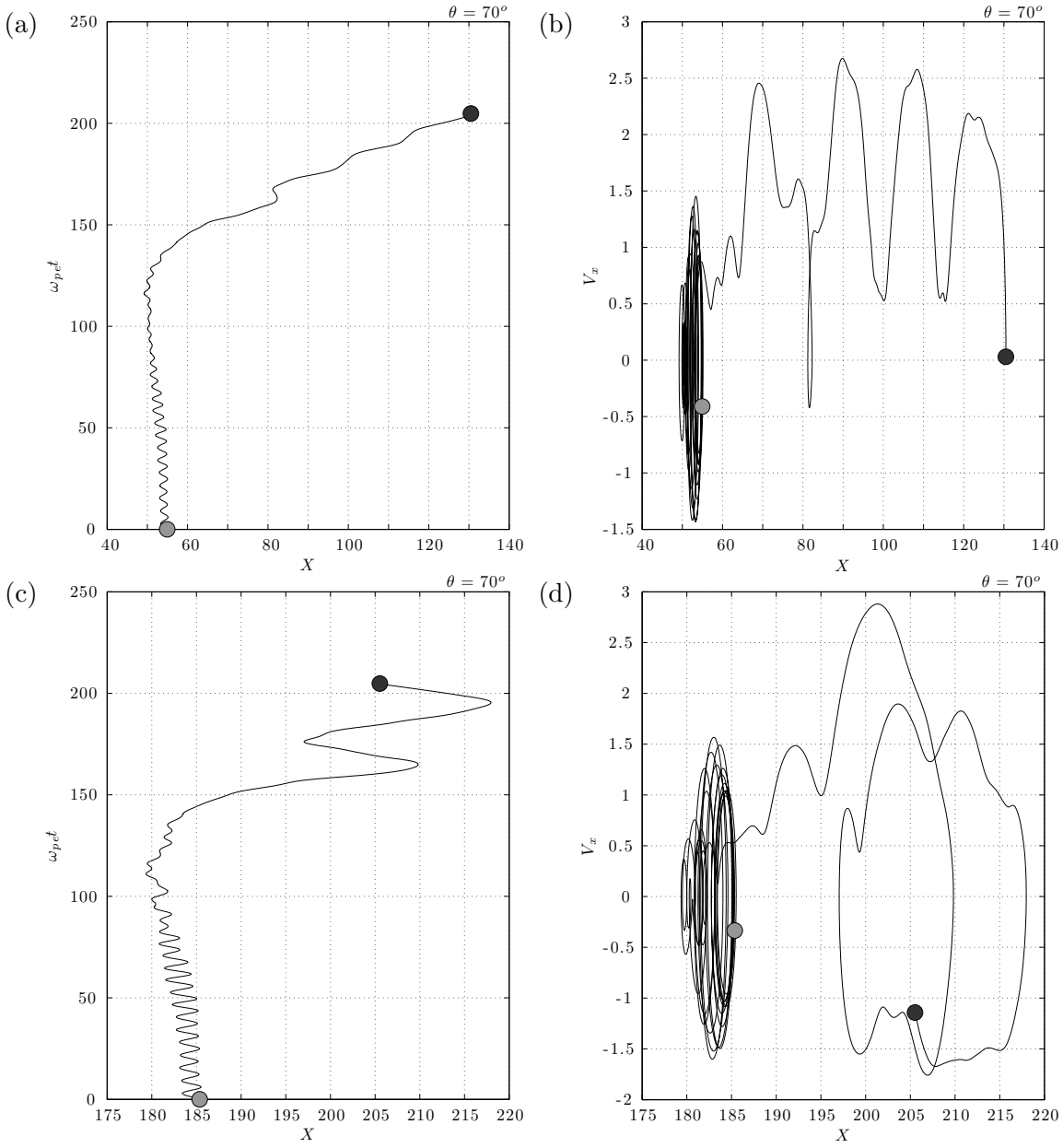

Figure 4.7: Trapped particle trajectories, the light grey circles mark the initial position of the particle and black cirlces the final position. (a) Phase space and position evolution of a trapped particle. (b) Time and position evolution of the same particle displayed in (a). (c) Phase space and position evolution of a second trapped particle. (d) Time and position evolution of the second particle displayed in (c)

The gray circles indicate the initial position of the particles and the black circles

the position at the end of the trajectory. Both particles exhibit velocity oscillations around a nearly constant position before becoming trapped in the wave and being accelerated to velocities that are nearly doubled. We note that the particles enter trapped orbits at $v_x \approx 0.5$, which is consistent with the phase velocity of the whistler wave at this angle. This is direct evidence that the particles are being trapped and energized by the wave. When the angle of propagation is $\theta = 30^o$ there is no evidence of particle trapping, staying consistent with the theme of less pronounced nonlinear dynamics at the shallower angle.

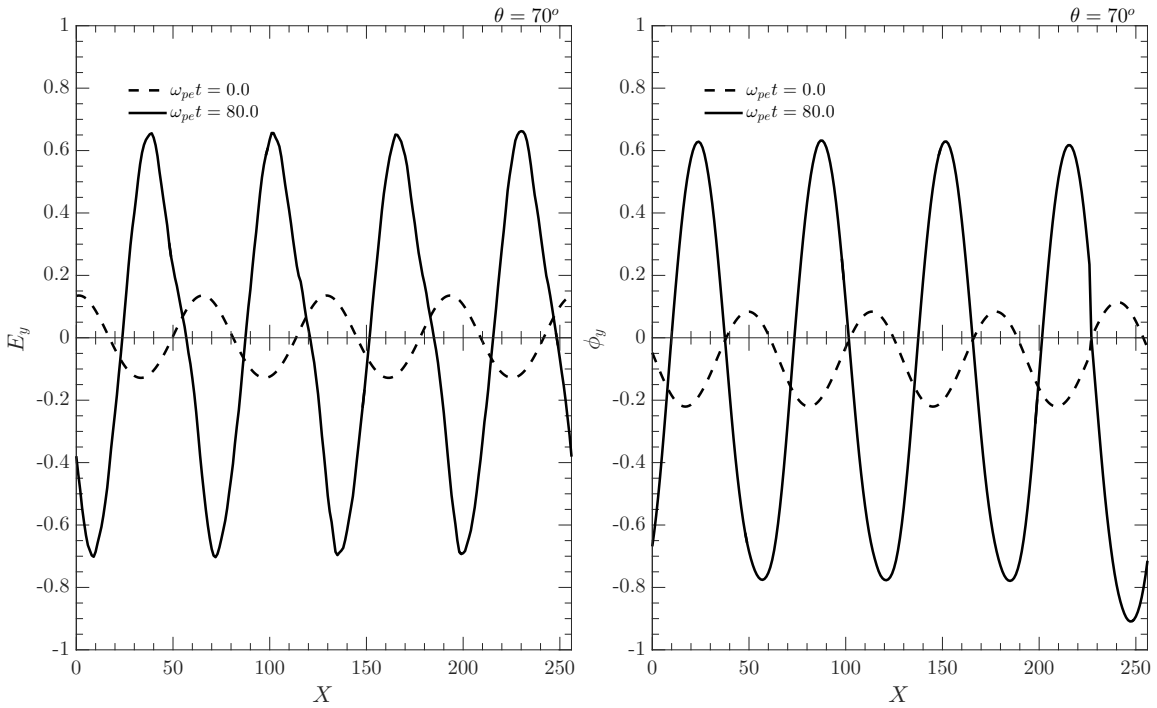

Figure 4.8: (a) The y-component of the electric field at $\theta = 70°$ for $\omega_{pe}t = 0$ (dashed line) and near the onset of particle trapping at $\omega_{pe}t = 80$ (solid line). (b) The corresponding electric potential, ϕ_y, at both the initial time (dashed line) and later time (solid line).

To further demonstrate the wave trapping the y component of the electric field and electric potential are shown in Fig. 4.8a and Fig 4.8b, respectively. The dashed lines

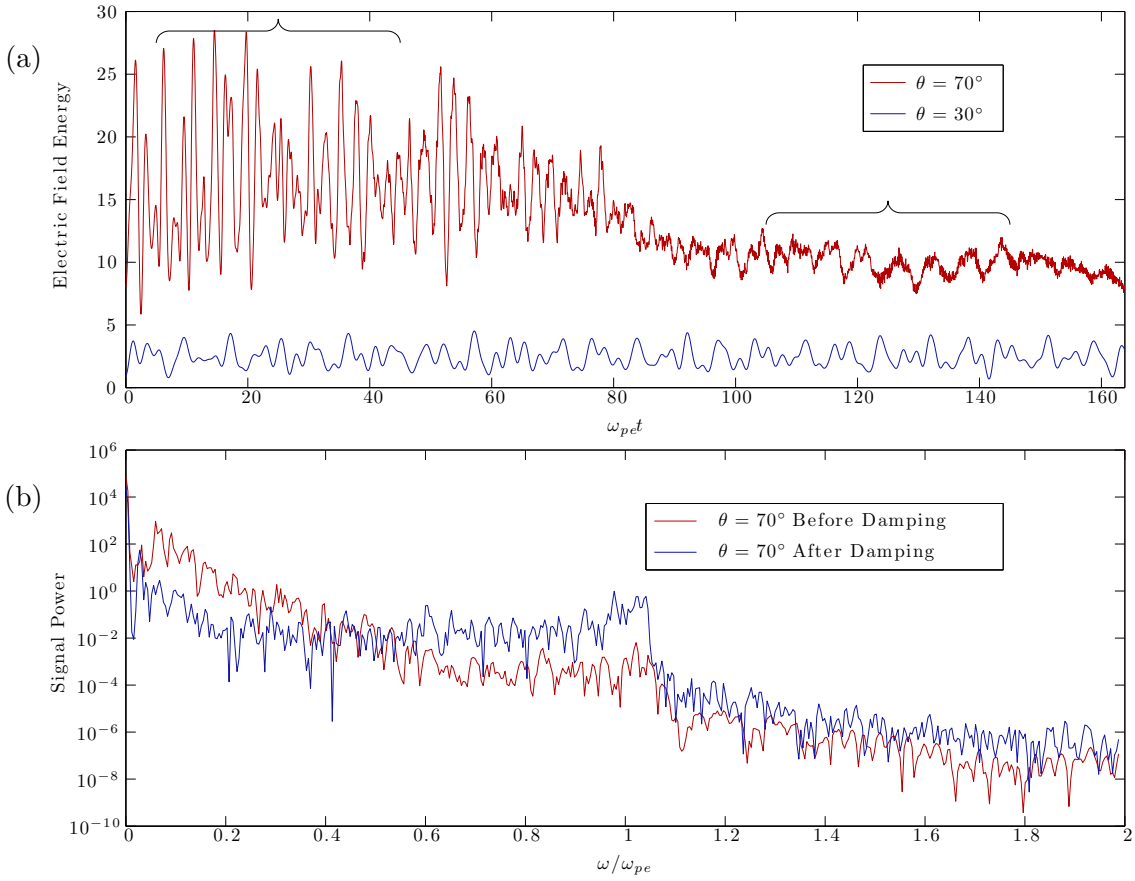

Figure 4.9: (a) The evolution of the electric field energy for propagation at $\theta = 30^o$ (blue) and $\theta = 70^o$ (red). Trapping at $\theta = 70^o$ occurs at $\omega_{pe}t \approx 70$ and coincides with a damping of the field energy. (b) Fourier analysis of the field energy at $\theta = 70^o$ before (red) and after (blue) the damping event shows a decrease in power of the whistler wave frequency and increase in Langmuir wave power after damping and trapping occur.

indicate the values at $\omega_{pe}t = 0$ while the solid lines indicate the values at $\omega_{pe}t = 80$. The development of deep potential wells in Fig 4.8b during the onset of the trapped particle trajectories seen in Fig. 4.7 supports the notion that the wave is responsible for this non-linear particle response.

Another important aspect of the particle trapping is the energy stored in the electric field. At the onset of particle trapping the energy of the electric field is significantly damped and exhibits a change in oscillation frequency. Fig. 4.9a shows

the electric field energy as a function of time for an arbitrarily large amplitude at both $\theta = 70^o$ and $\theta = 30^o$, shown in red and blue, respectively. First we note that there is no damping evident at $\theta = 30°$. At $\theta = 70^o$ there is evidence of the wave energy going through a damping phase from $\omega_{pe}t \approx 65$ to $\omega_{pe}t \approx 100$. At this amplitude the particle trapping begins around $\omega_{pe}t = 70$. This gives evidence that the energy stored in the field is being transferred to the trapped particles. Before and after the damping occurs there is a modulation of the high frequency oscillations in the field energy at $\theta = 70^o$. Fig. 4.9b shows the Fourier analysis of the oscillations prior to damping (red) and after damping (blue); the time range over which the transform is taken is indicated by braces in Fig 4.9a. The Fourier analysis reveals the dominant modulation prior to damping matches the frequency of the whistler wave, while a smaller modulation at the frequency of the Langmuir wave is also present. Following damping the modulation at the whistler frequency is decreased while the Langmuir frequency modulation increases and dominates.

4.2.3 PARTICLE ENERGIZATION

We now present a study of the energy distributions $f(E)$ of the self-consistent particle species to determine what role the waves play in the energization of particles. Fig. 4.10 displays the energy distributions of the self consistent particles for both $\theta = 30^o$ and $\theta = 70^o$; the initial distributions are shown by the dashed blue lines and a later time by the solid blue lines. The initial distribution function is cold and peaks at ~ 1 eV; the final energy distributions have been averaged over a single plasma oscillation. The perturbation amplitude corresponds to realistic waves observed in the radiation belts with $\delta B/B_0 = 0.01$. In Fig. 4.10a we see that for propagation at $\theta = 30^o$ the particles have undergone uniform thermalization by $\omega_{pe}t \approx 475$ peaked at an energy of ~ 100 eV. Similarly, in Fig. 4.10b at $\theta = 70^o$ the particles have also been

energized to be peaked around $\sim$ 100 eV but in a longer time scale of $\omega_{pe}t \approx 750$. It is an interesting outcome that at the more oblique propagation angle the wave takes longer to thermalize the particle distribution given the more nonlinear nature reported previously.

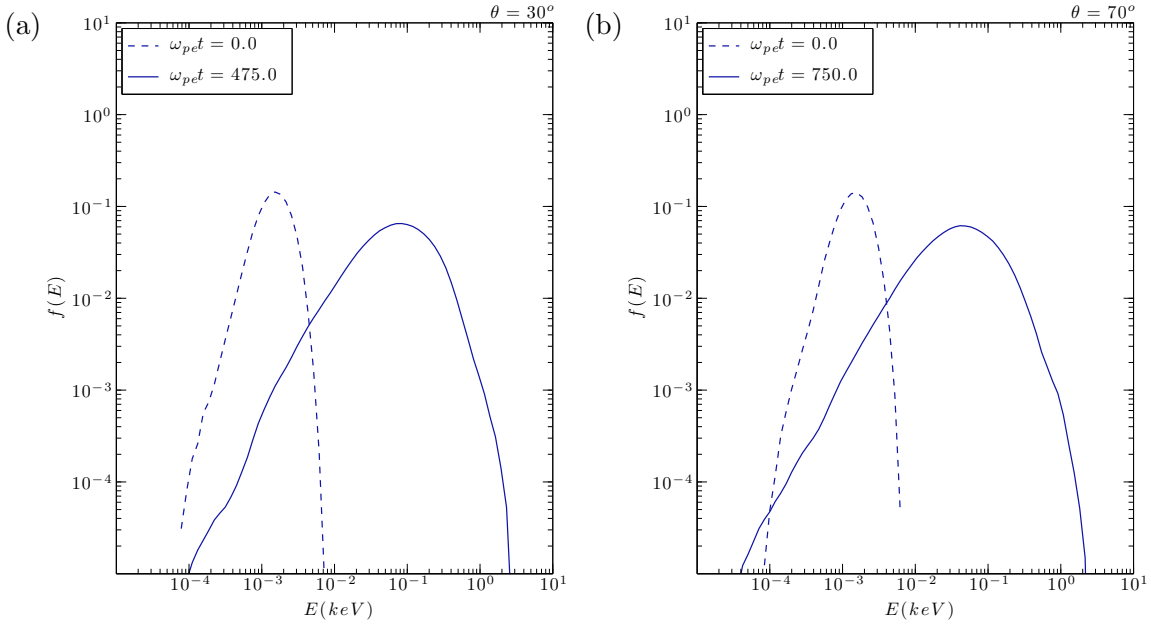

Figure 4.10: Thermalization of the particle energy distribution $f(E)$ of the self-consistent particle species during propagation of a wave with $\delta B/B_0 = 0.01$. The initial distribution is indicated by the dashed blue line and after thermalization by the soldi blue line. (a) The distribution for propagation of a wave at $\theta = 30^o$. (b) At $\theta = 70^o$ the final distribution is similar but takes longer to thermalize.

The results for the self-consistent particle species demonstrate that a large amplitude whistler wave is capable of uniformly thermalizing the energy distribution function. However, there is no direct evidence that large numbers of particles are being accelerated by the wave beyond the thermal distribution. To expand on this outcome, we initially load the non-interacting particles with a thermal distribution that is peaked around 100 eV to mimic the self-consistent particles after being thermalized; the self-consistent particles are kept cold. Fig. 4.11 displays the distribution

functions of the non-interacting particles when subjected to the same wave fields as the cold self-consistent particles. The initial distributions are indicated by the red dashed lines and the distributions at a later time by the solid red lines. We see that at $\theta = 70^o$ in Fig. 4.11b that the thermal distribution has become distorted and a population of electrons has been accelerated up to a maximum energy of $\sim 20 - 30$ keV. Similarly, in Fig. 4.11a at $\theta = 30^o$ there is evidence of electron acceleration up to a maximum of $\sim 8 - 9$ keV. The method employed here suggests that given an initial seed population of warmer electrons, an oblique whistler wave dominated by cold particle dynamics can further accelerate the warm population but not up to the MeV energies seen in previous studies.

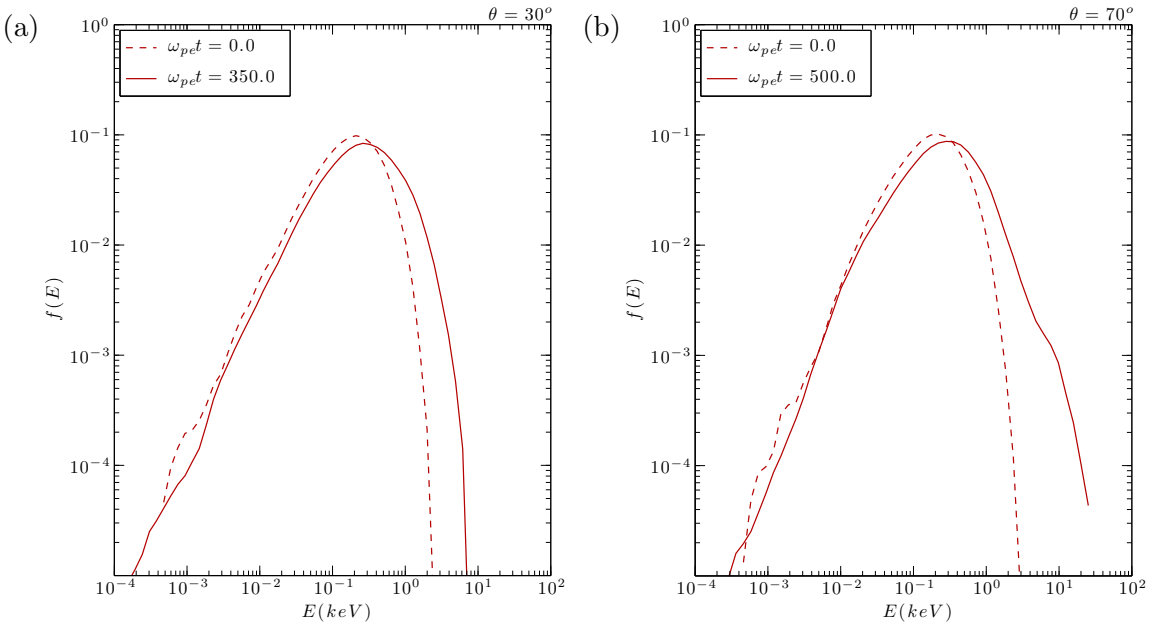

Figure 4.11: Acceleration of the particle energy distribution $f(E)$ of the non-interacting particle species during propagation of a wave with $\delta B/B_0 = 0.01$. The initial distribution is indicated by the dashed red line and after acceleration by the solid blue line. (a) The distribution for propagation of a wave at $\theta = 30^o$. (b) At $\theta = 70^o$ the final distribution is similar but takes longer to thermalize.

4.3 Discussion

In this section we make a comparison of the important time scales associated with the various physical processes which include wave steepening, particle trapping, thermalization and acceleration. This is followed by application of the simulation results to realistic plasma conditions in the Earth's radiation belts using the scaling relations between the different time scales of the physical process and initial wave amplitude. It should be noted that the scaling relations allow for more general application of the results to more realistic plasma conditions in terms of wave amplitude.

Large amplitude waves steepen because of the wave propagation speed dependence on the local wave intensity. *Yoon (2011)* has pointed out that large amplitude oblique whistler waves can steepen due to the presence of a longitudinal component. As shown in *Yoon (2011)* using fluid simulations and from particle simulations in this work illustrated in Fig. 4.4, the density perturbation steepens leading to a distorted non-sinusoidal waveform over long time scales. A steepening time scale (t_s) can be established from analysis of the waveforms at different times and associating t_s with $(\partial E_x/\partial x)_{max}$ like the event in Fig. 4.5. From a series of simulation runs using different initial wave amplitudes and fixed angle ($\theta = 70^o$), shown in Fig. 4.6, the steepening time scale follows a near inverse amplitude dependence, given by

$$\omega_{pe} t_s \sim 53.5 \left(\frac{\delta B}{B_0} \right)^{-0.9} \tag{4.1}$$

This scaling is also consistent with the fluid simulations of *Yoon (2011)*. Furthermore, *Yoon (2014)* [63] points out the significance of the propagation angle on the level of wave steepening; that paper concludes that regardless of the wave amplitude, only when sufficiently near the resonance cone will the oblique whistler wave see significant

steepening leading to wave breaking. For the wave at $\theta = 30^o$ the frequency is $\omega/\omega_{pe} = 0.14$ and Eq. (2.2) gives a resonance cone angle of $\theta_{res} \simeq 65^o$; similarly, for the wave propagating at $\theta = 70^o$ the resonance cone angle is $\theta_{res} \simeq 80^o$. The result that at $\theta = 30^o$ the steepening does not lead to wave breaking even at large amplitudes, while at any amplitude the wave at $\theta = 70^o$ eventually undergoes steepening and wave breaking is consistent with the findings of *Yoon (2014)*.

In the small amplitude wave limit Landau damping competes with the steepening process, however, in the large amplitude regime particle trapping and nonlinear damping become important. Particle trapping, as observed in the phase space plots of Fig. 4.7b and Fig. 4.7d, is mainly associated with the longitudinal electric field component of the oblique whistler wave. The trapping time scale in the electrostatic part of the wave field is approximated to be $t_{tr} = 2\pi\sqrt{m_e/(ekE_y \sin\theta \cos\theta)}$, where the term with the square root is the inverse bounce frequency of the particle trapped in the wave potential, k is the wave number of the large amplitude wave and E_y is the longitudinal electric field component [62]. Using the same normalization as the particle simulation model leads to the trapping time scale

$$\omega_{pe} t_{tr} = 2\pi \sqrt{\frac{1}{kE_y \sin\theta \cos\theta}} \tag{4.2}$$

From the simulations with $\theta = 70^o$, $\delta B/B_o = 0.3$, $k \simeq 0.098$, and $E_y \simeq 0.15$ in the formula above gives a trapping time $\omega_{pe} t_{tr} \simeq 92$. For this wave amplitude, Eq. (4.1) gives a steepening time $\omega_{pe} t_s \simeq 158$, which is about 1.7 times longer than the particle trapping time scale. Note that the particle trajectories of Fig. 4.7a and Fig. 4.7c are consistent with this trapping time scale estimate.

Once the particles become trapped in the large amplitude oblique wave a resonance damping begins to set in, this is clearly seen in Fig. 4.9a. After the trapping

begins a wave damping occurs over a time scale of $t_{damp} \sim 20 - 30\omega_{pe}^{-1}$, for the parameters stated in the previous paragraph. This so-called O'Neil damping is due to phase mixing of particles trapped in the wave potential and the general treatment for an obliquely propagating wave is found in *Palmadesso (1972)* [62]. This resonance damping vanishes after $\omega_{pe}t \sim 120$ and leaves an undamped oblique whistler wave for longer times. Fig. 4.9b illustrates the electric field wave power in the pre-damping phase which exhibits a lower frequency peak around $\omega \simeq 0.05\omega_{pe}$, and is consistent with the initial whistler wave perturbation frequency. After the wave damping the power spectrum reveals a decrease in the whistler wave power along with a corresponding increase in power at the plasma frequency (ω_{pe}). This increase in wave power at the plasma frequency is attributed to the distortion of the electron distribution function arising from particle acceleration in the nonlinear wave fields as we demonstrated in Section 4.2.3.

Furthermore, the distorted wave fields in Fig. 4.8a are consistent with space observations detailed in *Kellogg et al. (2010)* [23] who attribute this distortion to trapped particles. *Kellogg et al. (2010)* highlight that the distortion is minimal at less oblique angles, the distorting component is linearly polarized compared to the circularly polarized whistler component, and the trapped particle density is peaked in the potential wells of the trapping potential. Our simulation results agree that little distortion of the trapping fields is seen when the angle of propagation is $\theta = 30^o$, reinforcing the proposal that the distortion is due to particle trapping as this is also not evident at $\theta = 30^o$. Confirmation of the linearly polarized distortion field and extracting the trapped particle density profile we leave for future work.

Lastly, we discuss the time scale associated with particle heating and acceleration in the nonlinear wave fields, as seen in Fig. 4.10 and Fig. 4.11. For the case of $\theta = 70^o$, a scaling study of the acceleration time scale versus initial wave amplitude was made,

similar to the wave steepening time. The result obtained in normalized form is,

$$\omega_{pe} t_{ac} \sim \left(\frac{\delta B}{B_0} \right)^{-2/3} \tag{4.3}$$

For a comparison of this acceleration time to particle trapping and wave steepening temporal scales we consider an initial wave amplitude of $\delta B/B_o = 0.3$. This gives an acceleration time of $\omega_{pe} t_{ac} \sim 42.7$ which is comparable to the trapping time scale of $\omega_{pe} t_{tr} \sim 44$ and less than the steepening time $\omega_{pe} t_s \sim 158$. For the more realistic amplitudes in the Earth's radiation belt, $\delta B/B_o \sim 0.01$, the time scales are more separated with: $\omega_{pe} t_{ac} \sim 415.7$, $\omega_{pe} t_{tr} \sim 819.5$ and $\omega_{pe} t_s \sim 3375.6$. Here we note that the steepening time is considerably longer than the other characteristic time scales; it is possible that the wave damping from particle trapping occurring well before the steepening would increase this steepening time beyond the predicted time. The fluid simulation results in *Yoon (2011)* [19] report non-interacting particle acceleration up to a maximum energy on the order of 10 MeV when using an initial distribution peaked around 500 keV. Repeating our simulations with an initial thermal distribution of the non-interacting particles similar to that used by *Yoon (2011)* [19] results in very little acceleration. However, it is not clear that the acceleration of the lower energy seed population should scale to higher energies. A limitation of this work is that we use an isotropic energy distribution; it may be that non-interacting particles moving near the phase velocity of the wave experience very large accelerations while the bulk of the distribution remains unchanged. An extension of this work would be to use a non-interacting population that is mostly resonant with the wave to see if if all or most of the distribution is accelerated.

CHAPTER 5.

Nonlinear Wave Interactions

The following chapter presents results of modelling parallel whistler wave propagation using the UPIC Darwin code in three different scenarios: single electron species with electrostatic Langmuir waves, a single electron and single ion species with electrostatic Langmuir and ion acoustic modes, and two electron species at different temperatures to produce electrostatic Langmuir and electron acoustic modes. As stated previously in Chapter 3, the whistler wave is generated by adding sinusoidal external fields to the self-consistent transverse electric fields for the first $\omega_{pe}t = 100$ units of time after which the external fields are turned off and the pumped wave continues to propagate. The results of each of the three scenarios are presented in the following three sections. Here we make a note that the color scale dimension in many of the figures in the following results is purely qualitative and has been normalized to the maximum value occurring in the frame; all plots involving a Fourier analysis are the natural logarithm of the transform values and then normalized.

5.1 Langmuir Wave Coupling

We begin by presenting results simulations with a single moving electron species. The only electrostatic mode is the familiar Langmuir or electron plasma wave. The normalized electron thermal velocity is $v_{te} = 1.00$ corresponding to cell size $\Delta_x = \lambda_{De}$, the number of particles is $N_{pe} = 3.6864 \times 10^6$, the system length is $N_x = 2048$ cells, the electron cyclotron frequency is $\omega_{ce} = \omega_{pe}/3$, and the pumped whistler is mode $(kc/\omega_{pe} = 0.98, \omega = 0.1613\omega_{pe})$ corresponding to $n = 32$ where $k = 2\pi n/N_x$ and

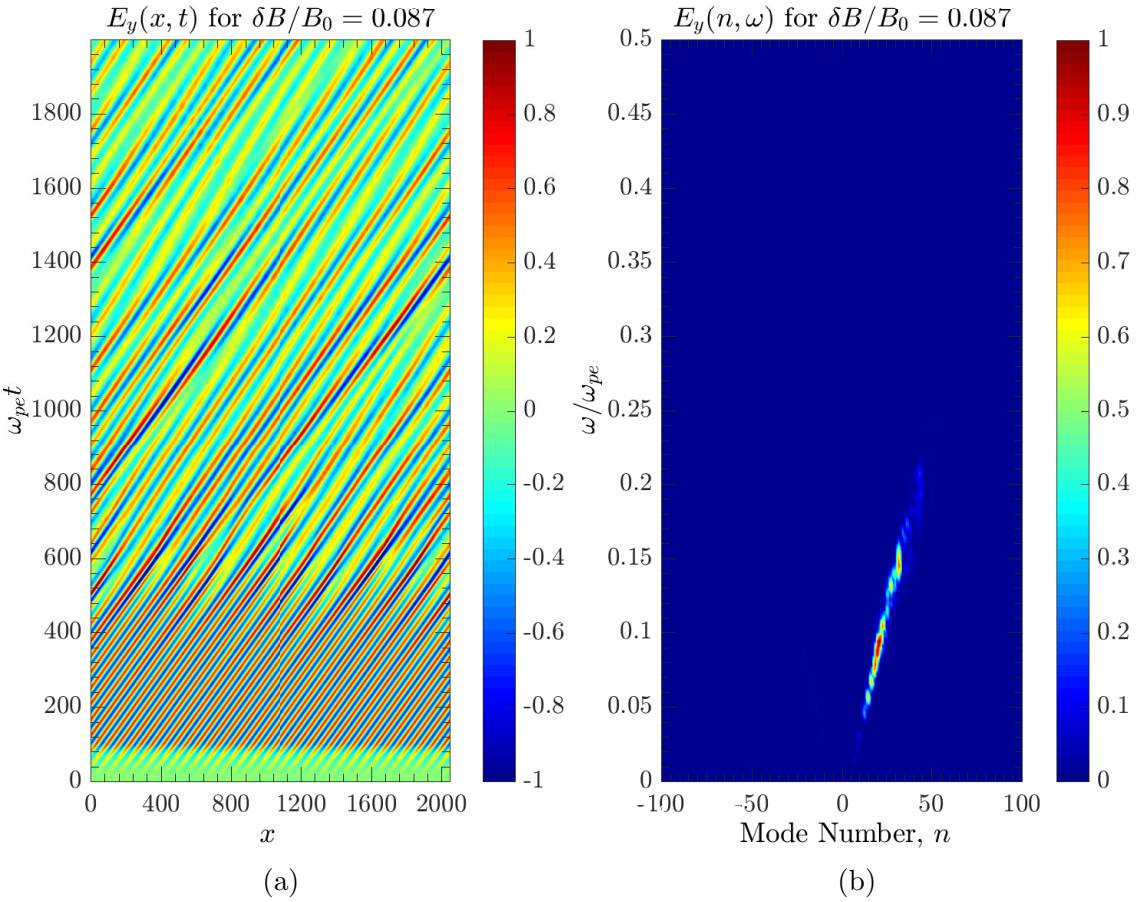

Figure 5.1: Result of a whistler pumped at ($n = 32$, $\omega = 0.163\omega_{pe}$) in the presence of a single electron species and fixed ions. (a) The space-time plot of the E_y field shows whistler decays into other forward travelling whistler waves. (b) The corresponding (n, ω) plot depicting the modes present in the transverse fields.

$c/\omega_{pe} = 1$. With a cyclotron frequency below the plasma frequency the Langmuir modes will never intersect the electrostatic ponderomotive modes produced by the pump whistler beating with the rest of the whistler branch. Given this setup, there should not be ponderomotive coupling between the whistler and Langmuir branches. The result of pumping a whistler in this scenario is depicted by the E_y transverse electric field component in Fig. 5.1. The space time evolution of Fig. 5.1a shows the pumped whistler wave being slowly ramped up until $\omega_{pe}t = 100$, at this time

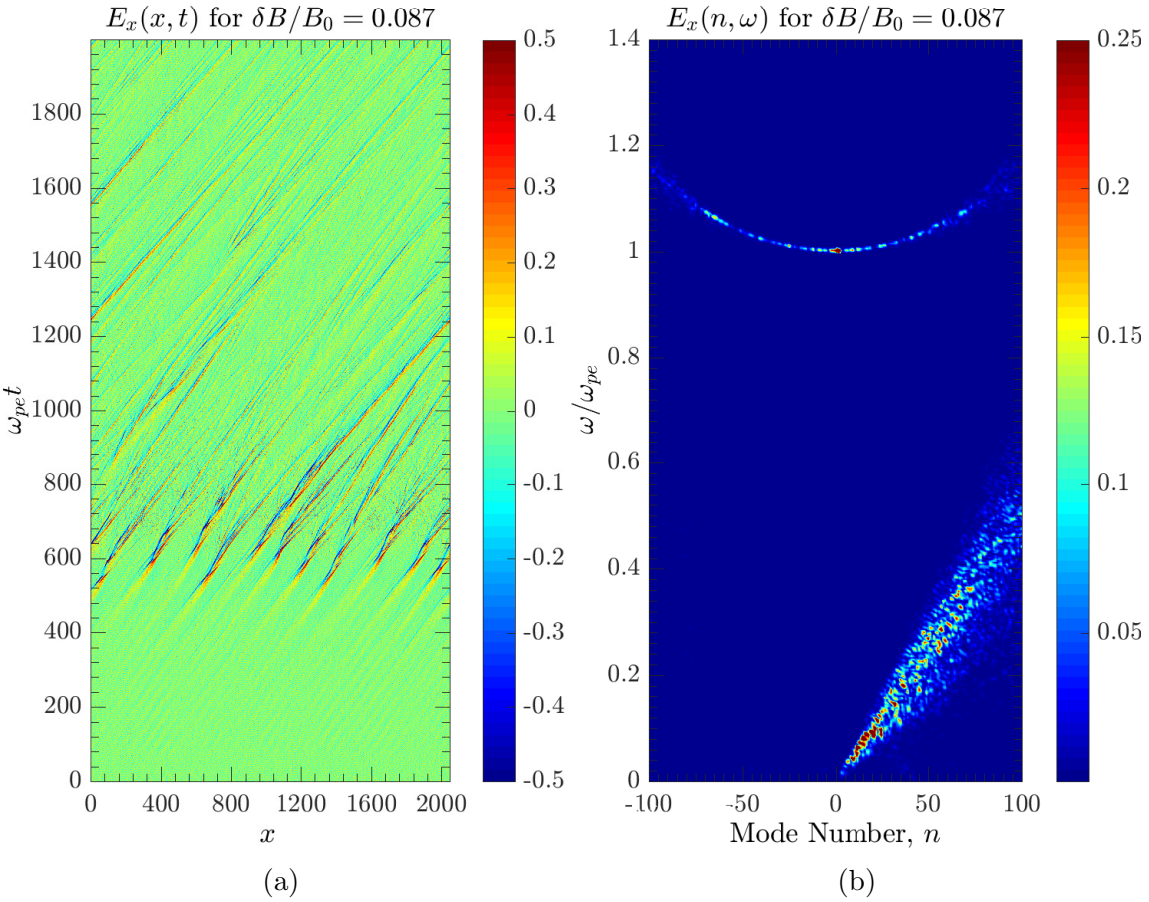

Figure 5.2: For the case depicted in Fig. 5.1 the decay of the whistler waves produces forward traveling beam-like structures in the electron density and E_x field. (a) The E_x space-time plot showing the beam-like structures that develop along x direction. (b) The corresponding (n, ω) plot shows the dispersion of these structures is mostly linear with some broadening at high mode numbers; the beam velocity is roughly equivalent to phase velocity of the whistler wave.

the amplitude is $\delta B/B_0 = 0.087$ and the external fields are turned off. The wave continues to propagate until $\approx \omega_{pe}t = 400$ when it begins to break up into a number of lower frequency and mode number whistler modes. Fig.5.1b shows the frequency and wavenumber map and reveals a broad spectrum of forward traveling whistler modes are excited. Simultaneously, in the space-time diagram of the E_x component of the electric field in Fig. 5.2a we see the generation of propagating nonlinear electrostatic

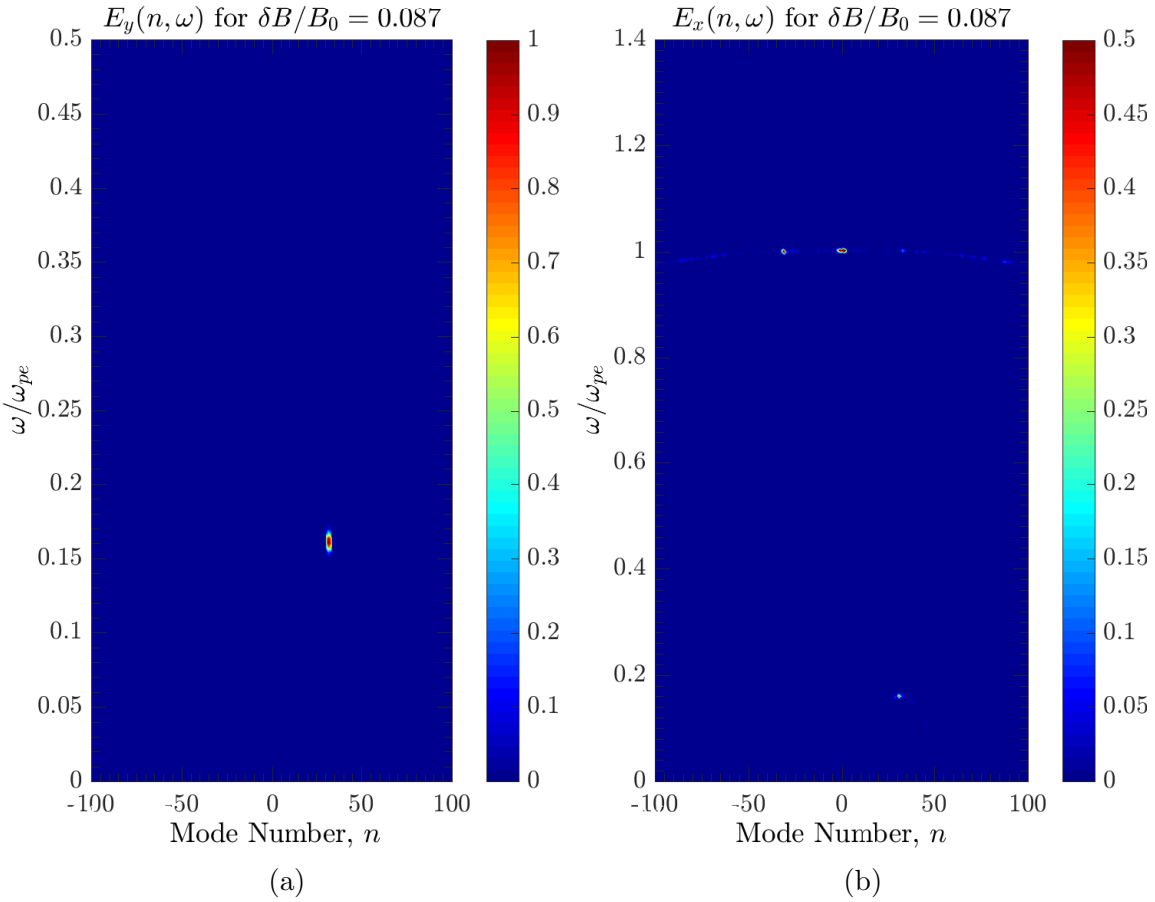

Figure 5.3: Repeating the simulation of Fig. 5.2 and Fig. 5.1 with cold electron population ($v_{te} = 0.316$) reveals a coupling between the Langmuir and Whistler branches. (a) The E_y component shows that the $n = 32$ whistler does not decay to other whistler modes. (b) The whistler mode at $n = 32$ couples into the longitudinal field and couples with the Langmuir branch at $n = -31$ and $n = 1$.

structures. Fourier analysis in Fig. 5.2b shows that the structures cover a broad range of frequencies and mode numbers with a nearly linear dispersion that spreads out at higher mode numbers. Additionally, the electron density also shows these structures but is not shown as it has more thermal noise in the Fourier analysis. The velocity of the structures covers the range of phase velocities of the pump whistler and the lower frequency daughter whistler waves, suggesting these modes are generating the structures.

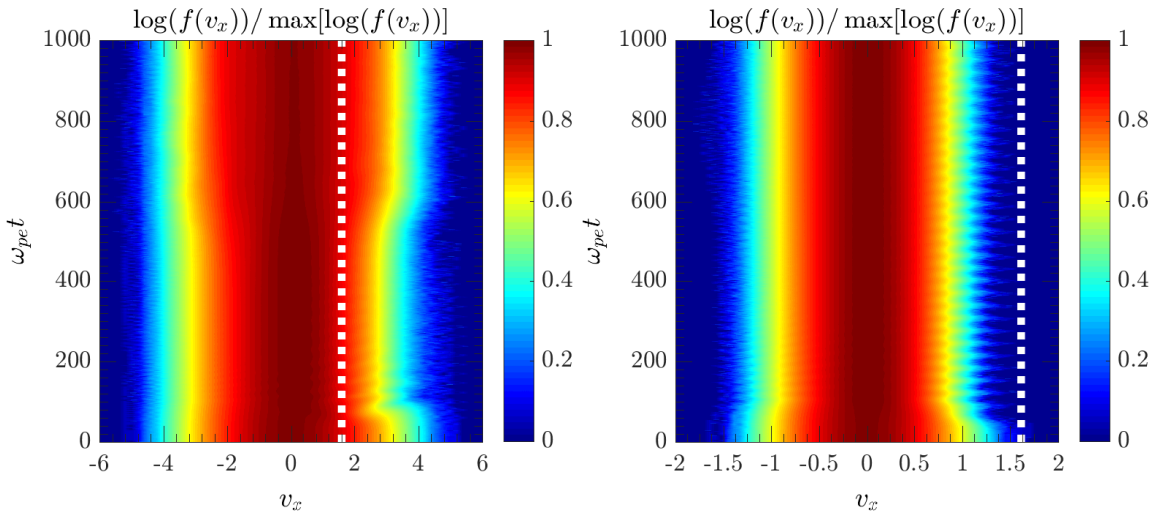

Figure 5.4: Velocity distribution functions for a single electron species when a whistler with amplitude $\delta B/B_0 = 0.087$. The phase velocity of the whistler mode that couples into the E_x field is indicated by a dashed white line. (a) Distribution when $v_{te} = 1.000$, the phase velocity of the wave is located inside the distribution and cools the tail distribution while producing a beam population near the phase velocity. (b) Distribution when $v_{te} = 0.316$, the phase velocity of the wave is well outside the distribution and causes small tail fluctuations.

To gain a better understanding of this process the electron population was cooled down to a thermal velocity of $v_{te} = 0.316$. The resulting E_y and E_x frequency and mode number analyses are shown in Fig. 5.3a and Fig. 5.3b, respectively. In the transverse field we see that the whistler wave no longer undergoes a decay into the broad range of daughter modes, while in the longitudinal field we see three modes have significant power above the thermal modes. The lower frequency electrostatic mode corresponds to the whistler mode, indicating the whistler is somehow coupling into the electrostatic field. The higher modes are Langmuir waves corresponding to modes $n = -31$ and $n = 1$, at slightly lower power are the opposite modes at $n = 31$ and $n = -1$. The Langmuir modes form a mode number matching with the $n = 32$ mode. With the cooler electron population no beam structures are formed.

An analysis of the evolution of the v_x electron velocity distribution function $f(v_x)$ for both the hot and cold electron scenarios is shown in Fig. 5.4. The phase velocity of the pumped whistler mode is indicated by a dashed white line. The whistler phase velocity lies outside of the cold distribution and along the slope of the hot distribution. The hot distribution in Fig. 5.4a is modified at $\omega_{pe}t \approx 75$; the positive tail of the distribution decreases and is balanced by an increase at the whistler phase velocity. The thermal distribution profile recovers from $\omega_{pe}t \approx 400 - 600$, around the same time that the whistler mode begins to decay into other whistler modes and the density structures form. The cold distribution in Fig. 5.4b remains mostly undisturbed except for small tail oscillations of the distribution at the pump whistler frequency.

All of this would suggest that the whistler mode is coupling into the longitudinal electric field through some mechanism with the Langmuir mode involving spatial beats, indicated by Fig. 5.3b. This beating is causing a modification of the parallel electron velocity distribution at the whistler phase velocity, which leads to the decay of the whistler mode and generation of beam like structures in the density when the phase velocity is situated inside the velocity distribution. At this time it is not clear what this nonlinear coupling mechanism is, though it is possible it is a higher order $\mathbf{J} \times \mathbf{B}$ effect. A qualitative analysis of the dependence on the whistler amplitude shows that this coupling occurs down to amplitudes of $\delta B/B_0 = 0.018$ where the coupling into the electrostatic branch still occurs but the resulting whistler decay and density structure growth are minimal.

5.2 Ion Acoustic Wave Coupling

A final result of the single electron species case demonstrates the ponderomotive beating of the pump whistler wave with the whistler branch. Using the cold electron

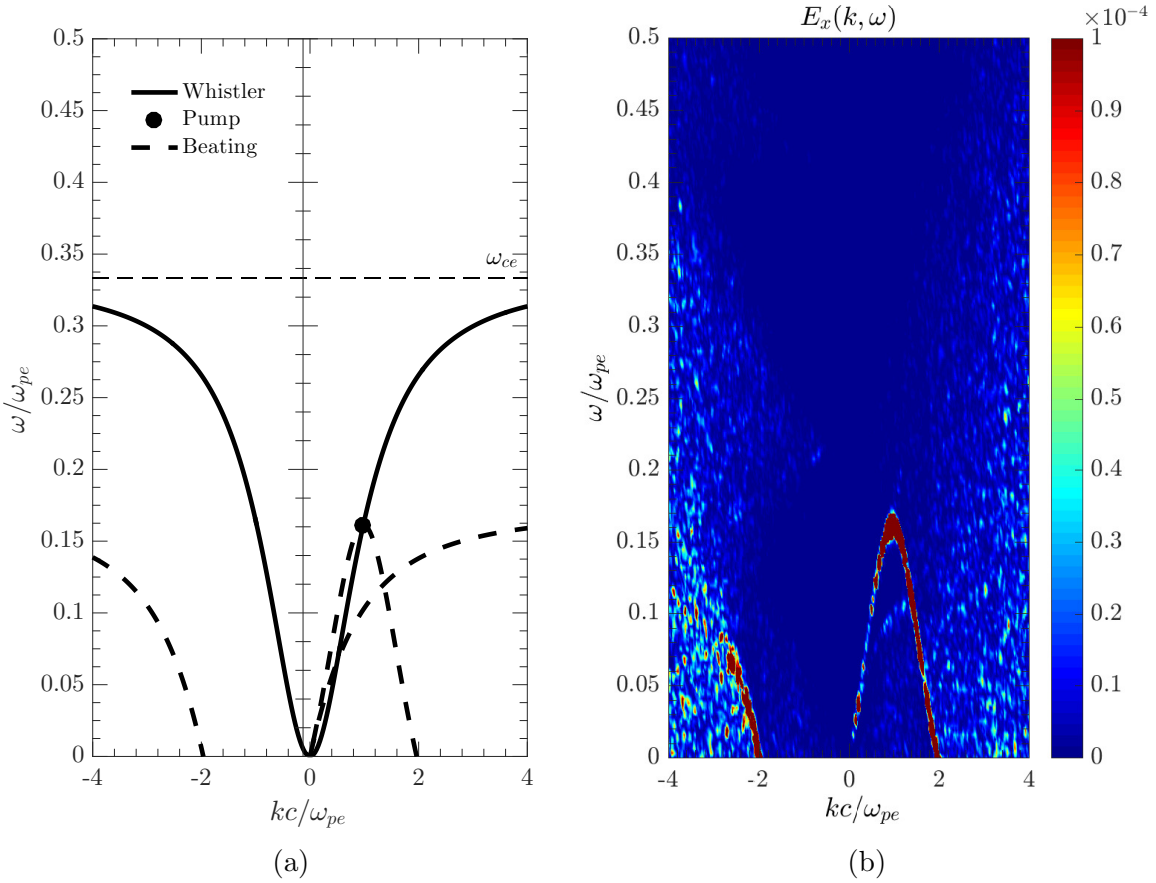

Figure 5.5: A comparison is made between the ponderomotive beating branches predicted by linear theory and the branches present in the simulation. (a) The branches predicted by linear theory that correspond to those seen in the simulation, the missing branches were shown earlier in Fig. 2.6. (b) A (k, ω) map of the E_x electric field reveals where the ponderomotive force has coupled into the electrostatic mode; the branches that are present show remarkable agreement with the beating predicted by linear theory.

distribution and a low amplitude whistler wave the Langmuir coupling effect just described is suppressed and the resulting E_x dispersion is displayed in Fig. 5.5b. The electrostatic modes generated from the ponderomotive force are revealed; these show remarkable agreement with the theoretical curves depicted in Fig. 5.5a. The theoretical branches assume the pump whistler is beating with the whole whistler dispersion but in reality the higher frequency whistler modes are going to experience

significant cyclotron damping by the electrons, meaning these modes are not going to beat very strongly with the pump. In Fig. 5.5a the two ponderomotive branches that saturate near $\omega_{ce}/2$ at high k are due to beating with the high frequency whistlers explaining why these are more damped in the simulation. However, in Fig 5.5a we only show the theoretical pondermotive branches that appear in the simulation; Fig. 2.6 shows more branches than are seen in the simulation, exact mirrors in direction of the modes present in the simulation. It is not clear why these modes are not coupled into the electrostatic field, it could simply be due to the initial conditions or a more fundamental aspect of the parametric coupling. In summary, Fig. 5.5 shows that we do have coupling into the electrostatic field that matches with the ponderomotive branches predicted by the parametric coupling conditions of Eqs. (2.27) and (2.28).

For simulations involving both ions and electrons the parameters used to simulate a plasma with an undamped ion acoustic mode are a electron thermal velocity of $v_{te} = 1.00$, a temperature ratio of $T_e/T_i = 100$ and a mass ratio of $M/m_e = 16$. The system length is $N_x = 512$, the number of particles of each species is $N_{pi} = N_{pe} = 1.8432 \times 10^5$, and the cyclotron frequency is again $\omega_{ce} = \omega_{pe}/3$. The dashed red line in Fig. 5.6a shows the theoretical dispersion of the ion acoustic mode. To analyse the ion acoustic mode in the simulations we use the the ion density fluctuations δn_i, which is simply the subtraction of the average density from the density and removes the large DC component from a Fourier analysis. The dispersion analysis of δn_i for a simulation with no pump whistler in Fig. 5.6b shows there is indeed an undamped ion acoustic mode that agrees well with the theoretical dispersion indicated by the dashed white line. However, the simulation dispersion shows a broader region of undamped modes than theory predicts and it is not clear at this time why this broadening occurs. Fig. 5.6a also indicates the whistler (solid black) and ponderomotive branches (dashed black); at the intersections of the ion acoustic and ponderomotive branches a three-

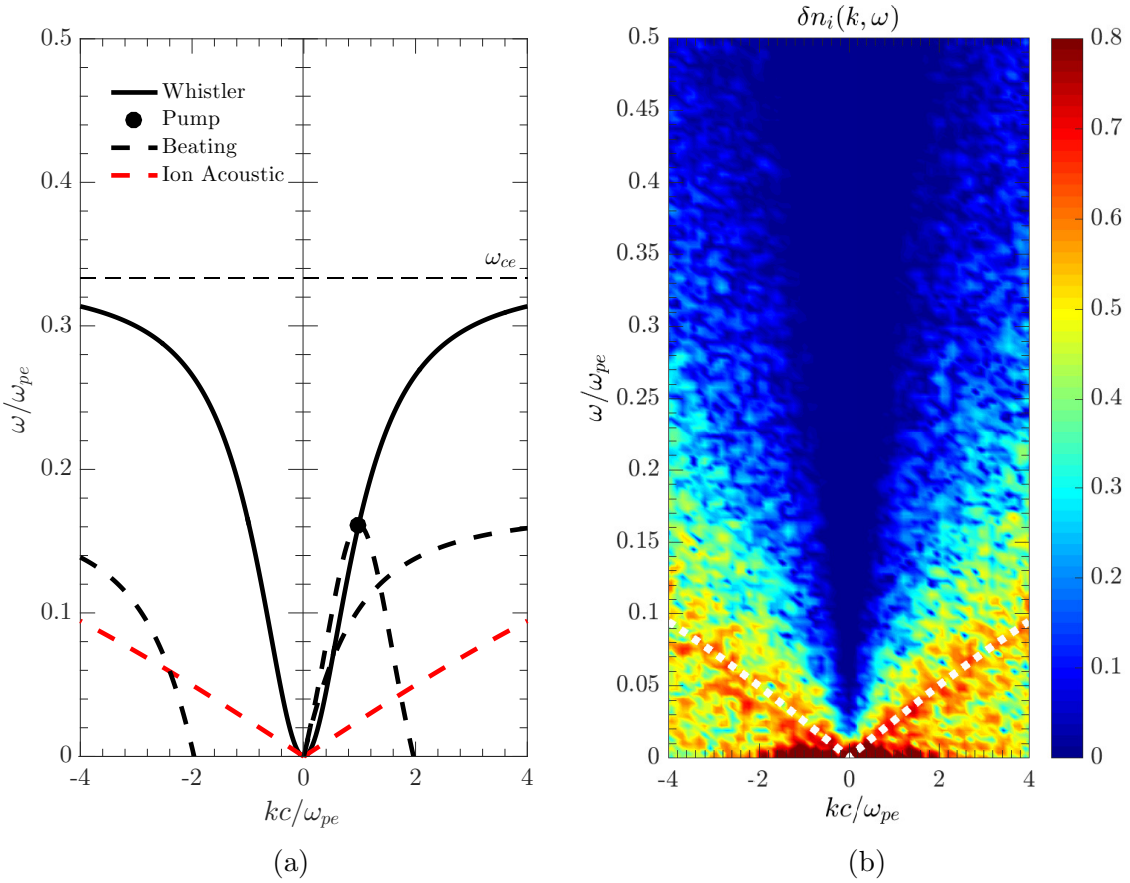

Figure 5.6: (a) Theoretical coupling potential for a pumped whistler and IAW; the whistler branch is indicated by the black line, the ponderomotive beating branches by the black dashed line, and the IAW by the dashed red line. (b) The ion density Fourier analysis shows the ion acoustic dispersion from the thermal motions of the ions, the theoretical dispersion of Eq. (2.3) is overplotted as a white dotted line to show the agreement between theory and simulation.

wave parametric coupling can occur.

5.2.1 Single, Double, and Triple Decay

Next we present results from simulations with a pumped a whistler at ($n_P = 8, \omega_P = 0.1613\omega_{pe}$) with an amplitude of $\delta B/B_0 = 0.036$. Fig. 5.7a and Fig. 5.7b show the space-time plots of the E_y electric field and ion density fluctuations, respectively. In Fig. 5.7a the whistler mode is successfully launched and at $\omega_{pe}t \approx 350$ a second

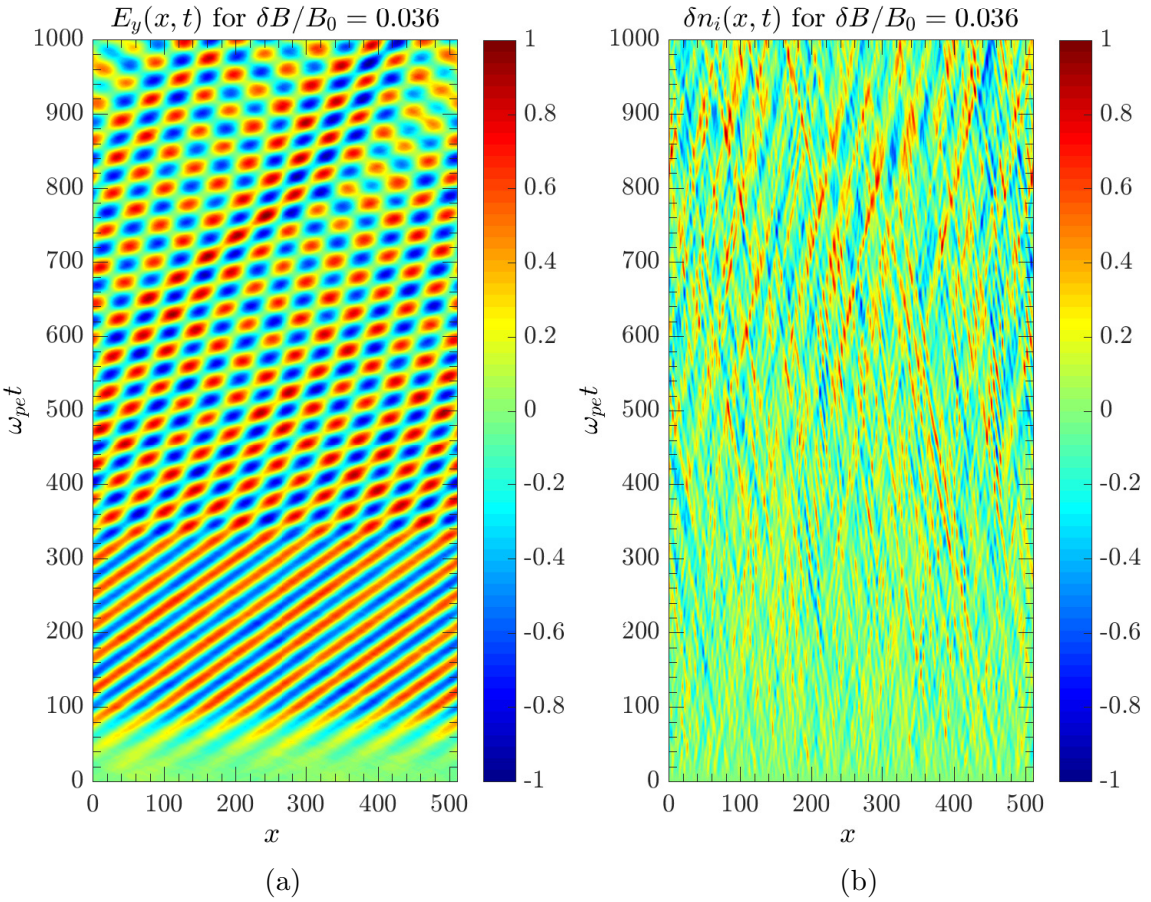

Figure 5.7: The parametric decay of a pumped whistler wave is observed. (a) The E_y component of the electric field space-time diagram, the pumped whistler begins to decay at $\omega_{pe}t \approx 400$ into a backwards travelling whistler wave. (b) The ion density evolution shows the generation of a forwards propagating ion acoustic mode

backwards travelling daughter whistler mode develops. At around the same time in Fig. 5.7b we see the development of a coherent ion acoustic mode. Fig. 5.8a is a spatial Fourier analysis showing the evolution of the modes present in the transverse electric fields. The whistler mode at $n = 8$ is accompanied by the growth of the $n = -6$ mode. Fig. 5.8b shows that the frequency of the daughter whistler is $\omega \approx 0.119\omega_{pe}$. Similar mode evolution and dispersion maps of the ion density fluctuations are shown in Fig. 5.9a and Fig. 5.9b, respectively. While the ion acoustic mode shows several

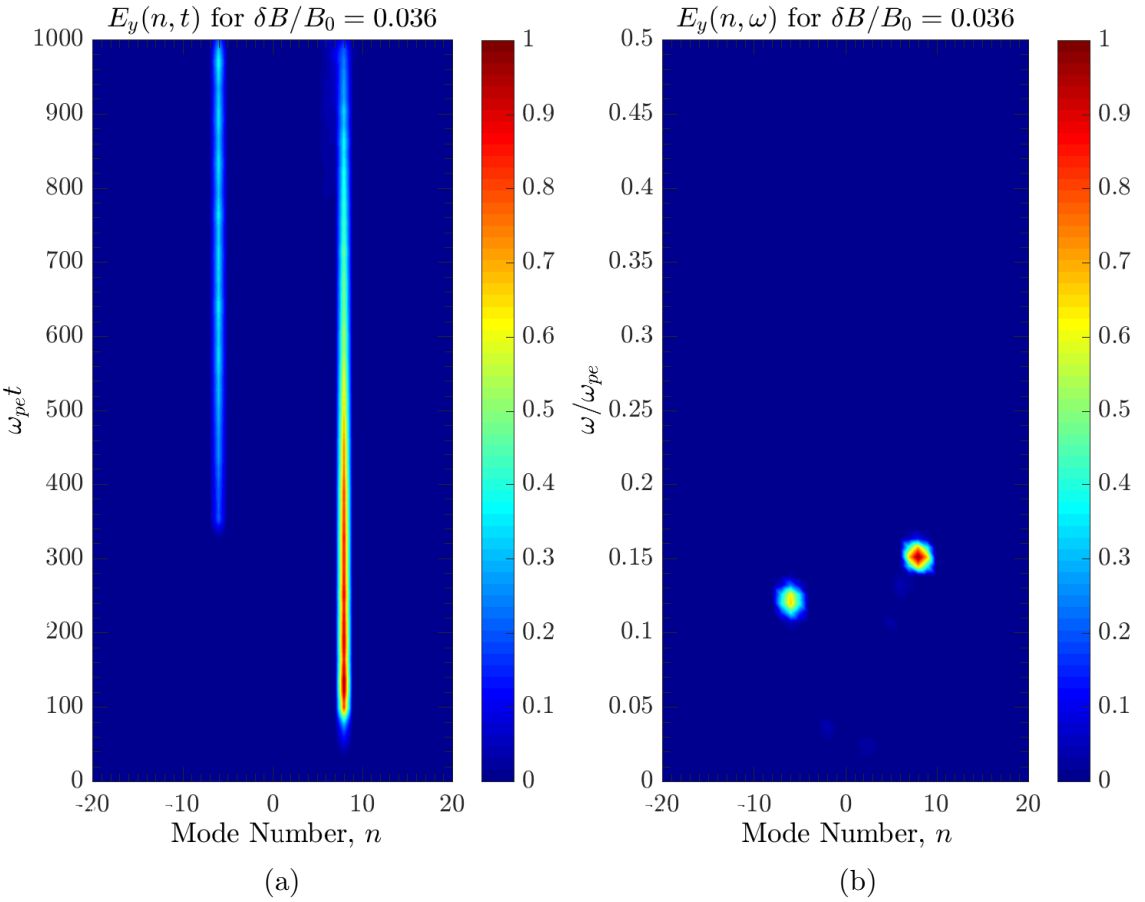

Figure 5.8: (a) The E_y component of the electric field (n,t) diagram, the pump and daughter whistler wave are present. These modes correspond to integer mode numbers $n_P = 8$ and $n_{H1} = -6$. (b) The E_y component of the electric field (n,ω) diagram, the daughter mode has frequency $\omega_{H1} \approx 0.119\omega_{pe}$.

undamped modes the $n = 14, \omega \approx 0.43\omega_{pe}$ mode shows significant growth over the rest of the modes at the same time as the $n = -6$ whistler mode.

The sum of the daughter mode numbers,

$$n_{H1} + n_{L1} = -6 + 14 = 8 = n_P$$

where the subscripts $H1$ and $L1$ refer to the high frequency daughter whistler and low frequency daughter IAW, exactly satisfy the spatial parametric coupling condition

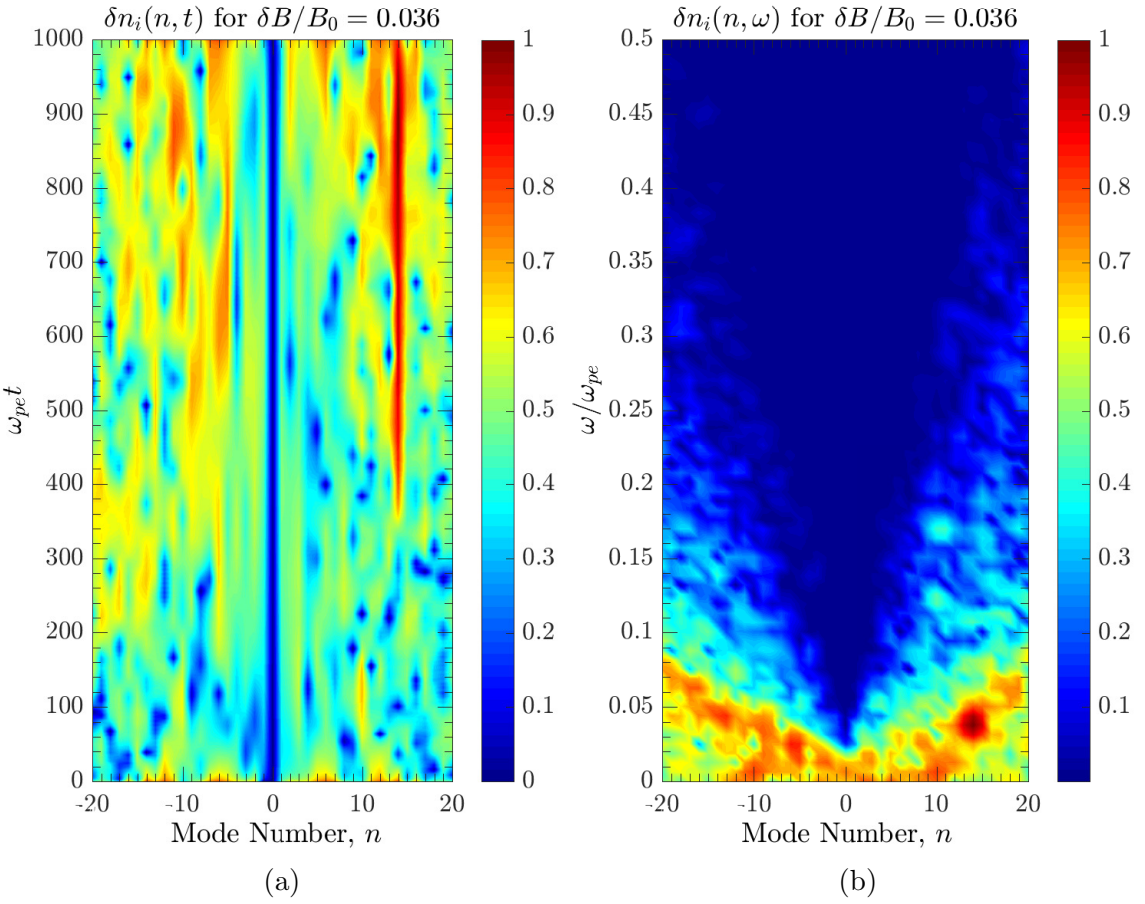

Figure 5.9: (a) The mode number evolution of the ion density, the daughter ion acoustic mode number corresponds to $n_{L1} = 14$. (b) The (n, ω) map of the ion density, the mode in (a) has frequency $\omega_{L1} \approx 0.043\omega_{pe}$.

Eq. (2.28). Similarly, the frequency sum is,

$$\omega_{H1} + \omega_{L1} = 0.119\omega_{pe} + 0.043\omega_{pe} = 0.162\omega_{pe} \approx \omega_P = 0.1613\omega_{pe}$$

and Eq. (2.27) is approximately satisfied, partly due to the finite frequency resolution. Fig. 5.10 illustrates the theoretical wavenumber and frequency matching that has occurred in Fig. 5.7. The modes satisfying the exact coupling conditions are indicated next to the black dots highlighting the three-wave coupling. In theory, the

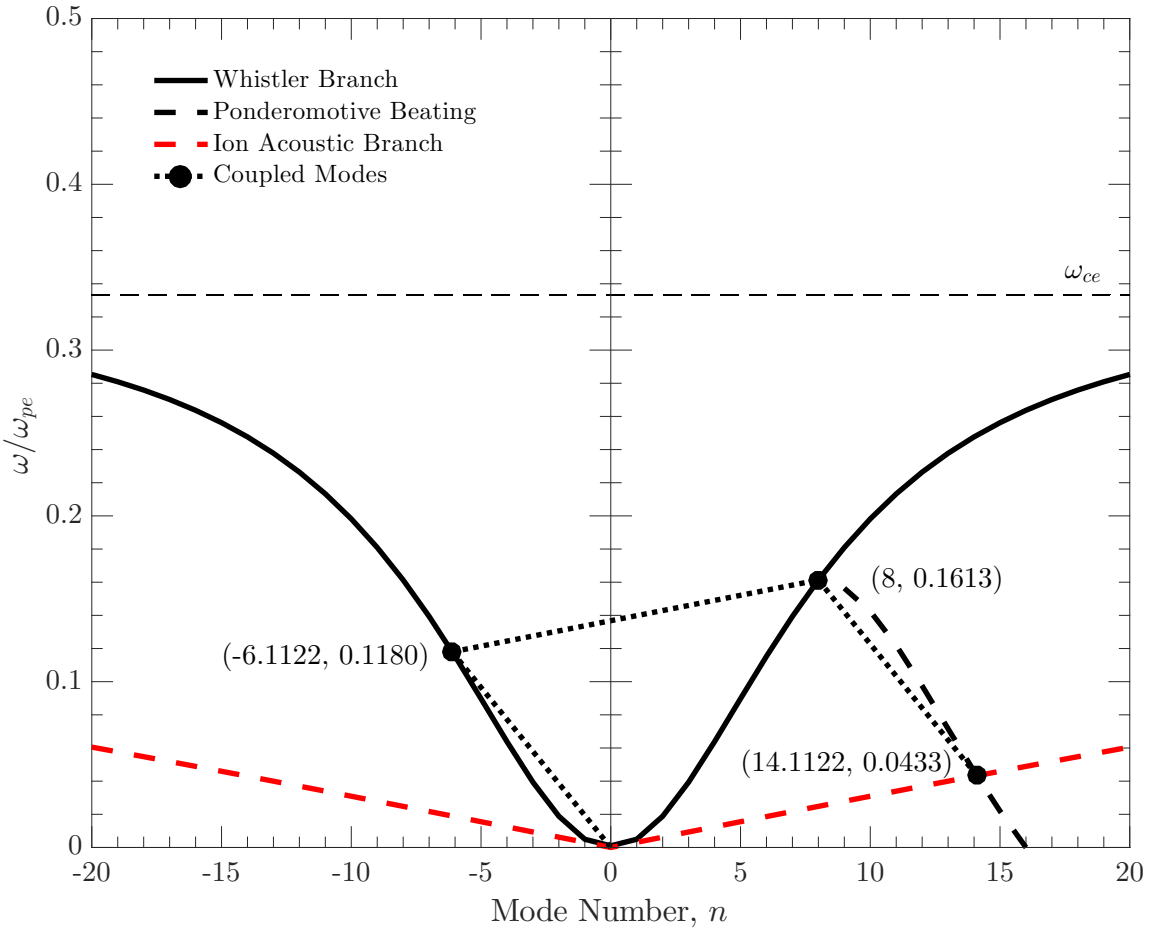

Figure 5.10: The parametric coupling for the decay of the $n_P = 8$ pump whistler mode into a backscattered daughter whistler wave and forward travelling daughter ion acoustic mode seen in Fig. 5.7. The whistler branch is indicated by the solid black line, the ponderomotive beating of the pump whistler branch with the backwards travelling whistler branch is indicated by the black dashed line, the ion acoustic mode is indicated by the red dashed line, and the coupled modes are indicated by large black dots with dotted connecting lines. The mode number and normalized frequency of the coupled modes are indicated next to the dots.

mode numbers do not correspond to exact integers like the simulation, which is restricted to integer modes by periodic boundary conditions. Fig. 5.6a indicates that in addition to the forward travelling ion acoustic coupling there is the potential for a separate three-wave coupling involving a backward travelling ion acoustic mode; it is

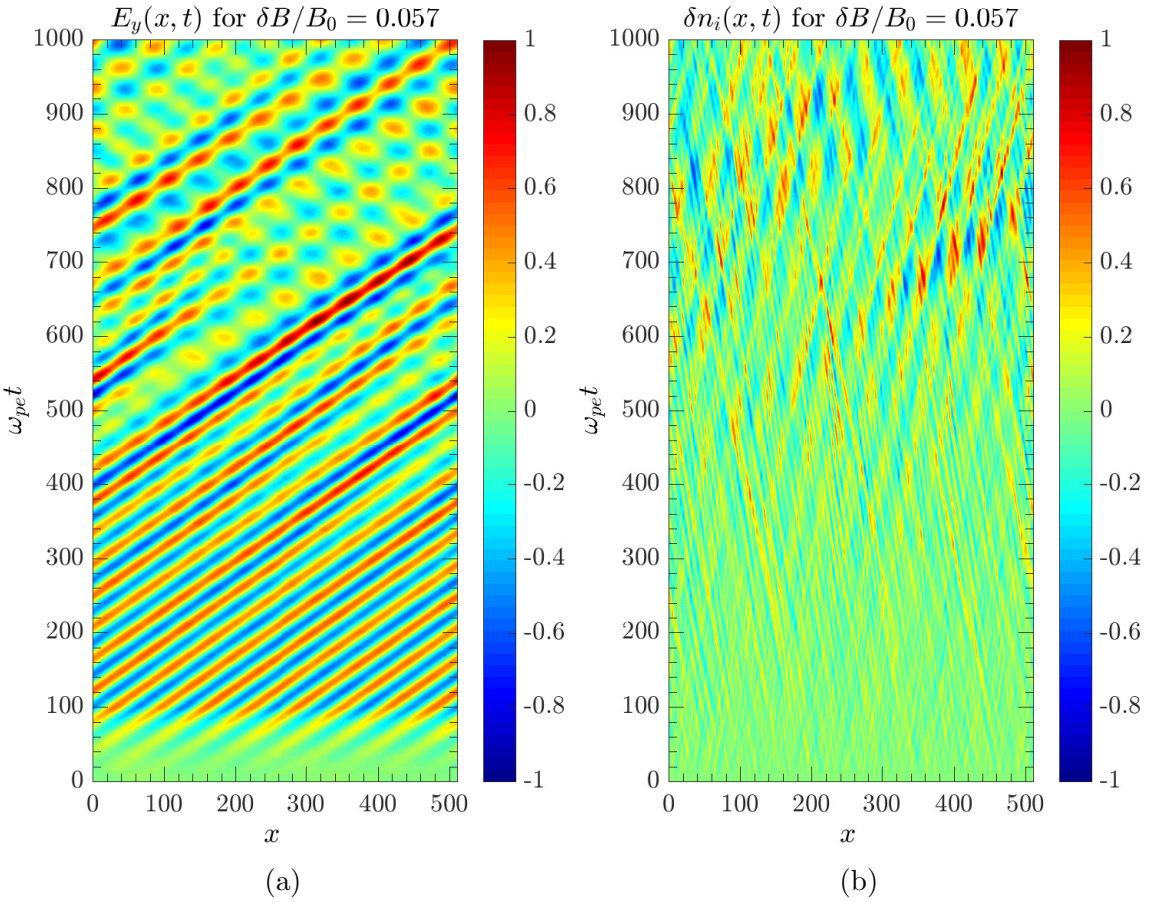

Figure 5.11: The double parametric decay of a pumped whistler wave is observed. (a) The E_y component of the electric field space-time diagram, the pumped whistler begins the first decay at $\omega_{pe}t \approx 350$. (b) The ion density evolution, generation of new ion acoustic modes coincides with the growth of whistler wave modes in (a).

likely the former process dominates due to the daughter whistler experiencing lighter cyclotron damping than the higher frequency daughter whistler that matches in the latter and thus the ponderomotive beating is stronger. To summarize, it is clear that the daughter whistler and ion acoustic modes seen in Figs. 5.8 and 5.9 correspond to a single, three-wave parametric decay facilitated by the ponderomotive force.

Next we present a similar simulation with the only change being the amplitude of the pump whistler increased to $\delta B/B_0 = 0.057$. Fig. 5.11 displays the E_y and

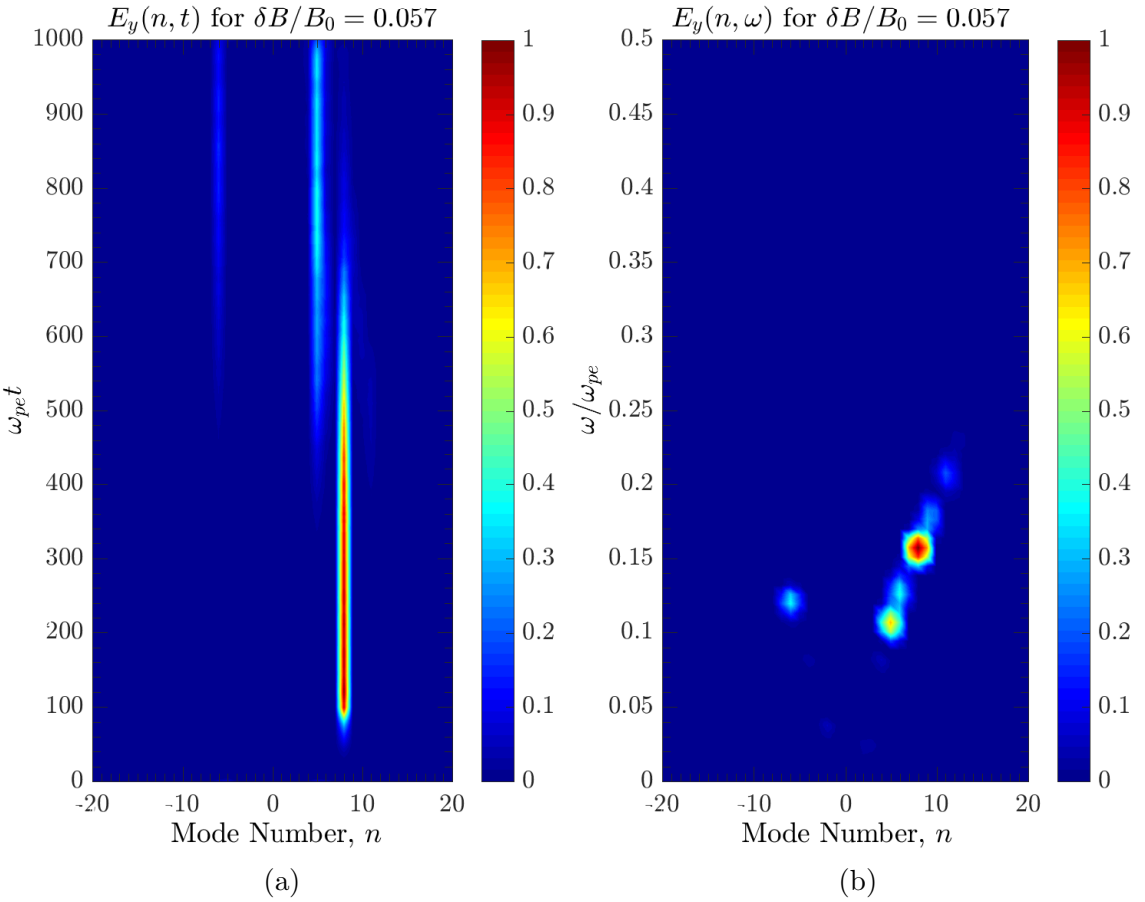

Figure 5.12: (a) The E_y component of the electric field (n,t) diagram, the pump and two daughter whistler mode numbers present. These modes correspond to integer mode numbers $n_P = 8$, $n_{H1} = -6$, and $n_{H2} = 5$. (b) The E_y component of the electric field (n,ω) diagram, the daughter modes in (a) are highlighted along the whistler branch with corresponding frequencies $\omega_{H1} \approx 0.119\omega_{pe}$, and $\omega_{H2} \approx 0.094\omega_{pe}$.

δn_i space-time plots. The transverse field in Fig. 5.11a again shows the decay of the pump whistler into a backwards travelling whistler but also a second daughter whistler mode travelling in the forward direction. The ion density evolution in Fig. 5.11b also indicates a second ion acoustic mode travelling backward in addition to the forward travelling mode seen in the single parametric decay. Fig. 5.12 and Fig. 5.13 show the same Fourier analysis of E_y and δn_i used to analyse the single decay. The new

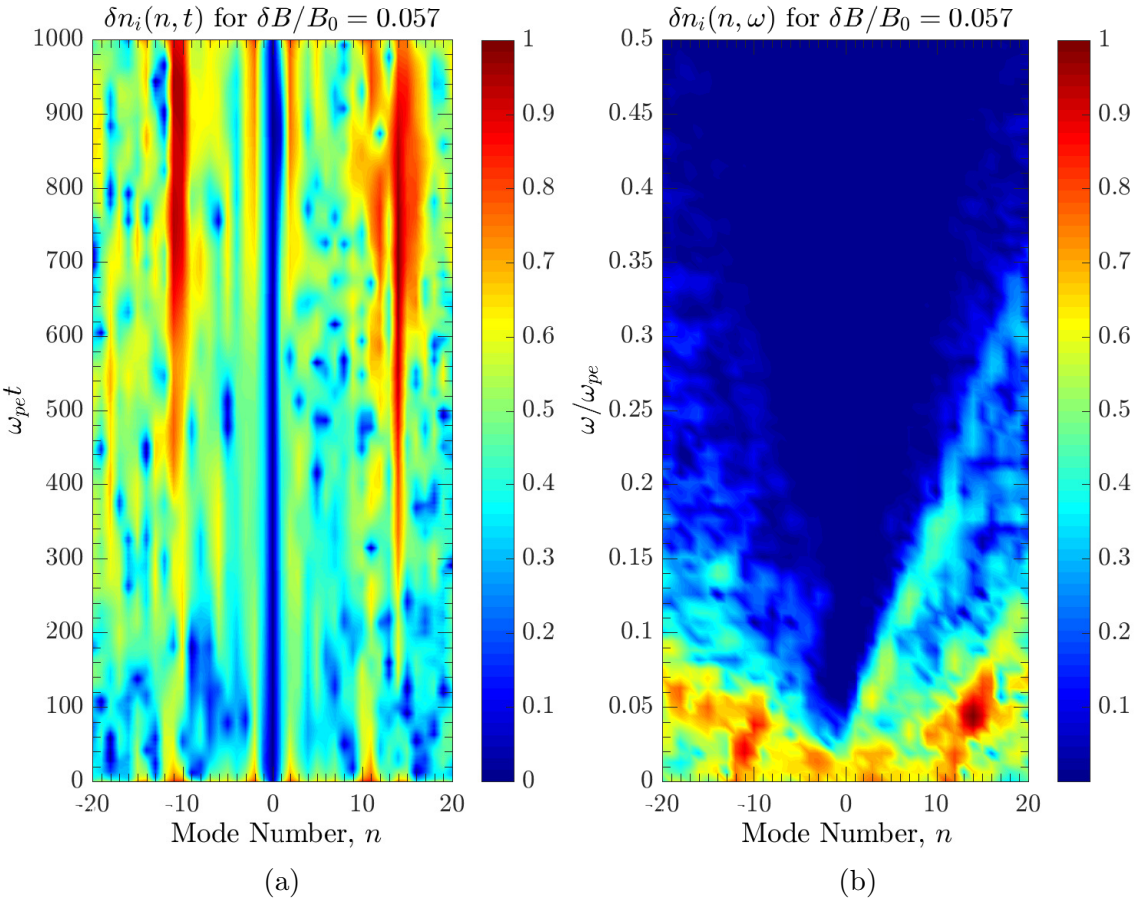

Figure 5.13: (a) The mode number evolution of the ion density, the two daughter IAW numbers show the largest power. These modes correspond to integer mode numbers $n_{L1} = 14$, and $n_{L2} = -11$. (b) The (n, ω) map of the ion density, the modes in (a) are along the ion acoustic branch with frequencies $\omega_{L1} \approx 0.043\omega_{pe}$ and $\omega_{L2} \approx 0.026\omega_{pe}$.

whistler mode corresponds to the $(n_{H2} = 5, \omega_{H2} = 0.094\omega_{pe})$ and the ion acoustic mode to $(n_{L2} = -11, \omega_{L2} = 0.026\omega_{pe})$, where the subscripts $H2$ and $L2$ refer to these being the second high and low frequency daughter modes.

The mode and frequency sums,

$$n_{H2} + n_{L2} = 5 + (-11) = -6 = n_{H1}$$

$$\omega_{H2} + \omega_{L2} = 0.094\omega_{pe} + .026\omega_{pe} = 0.12\omega_{pe} \approx \omega_{H1} = 0.119\omega_{pe}$$

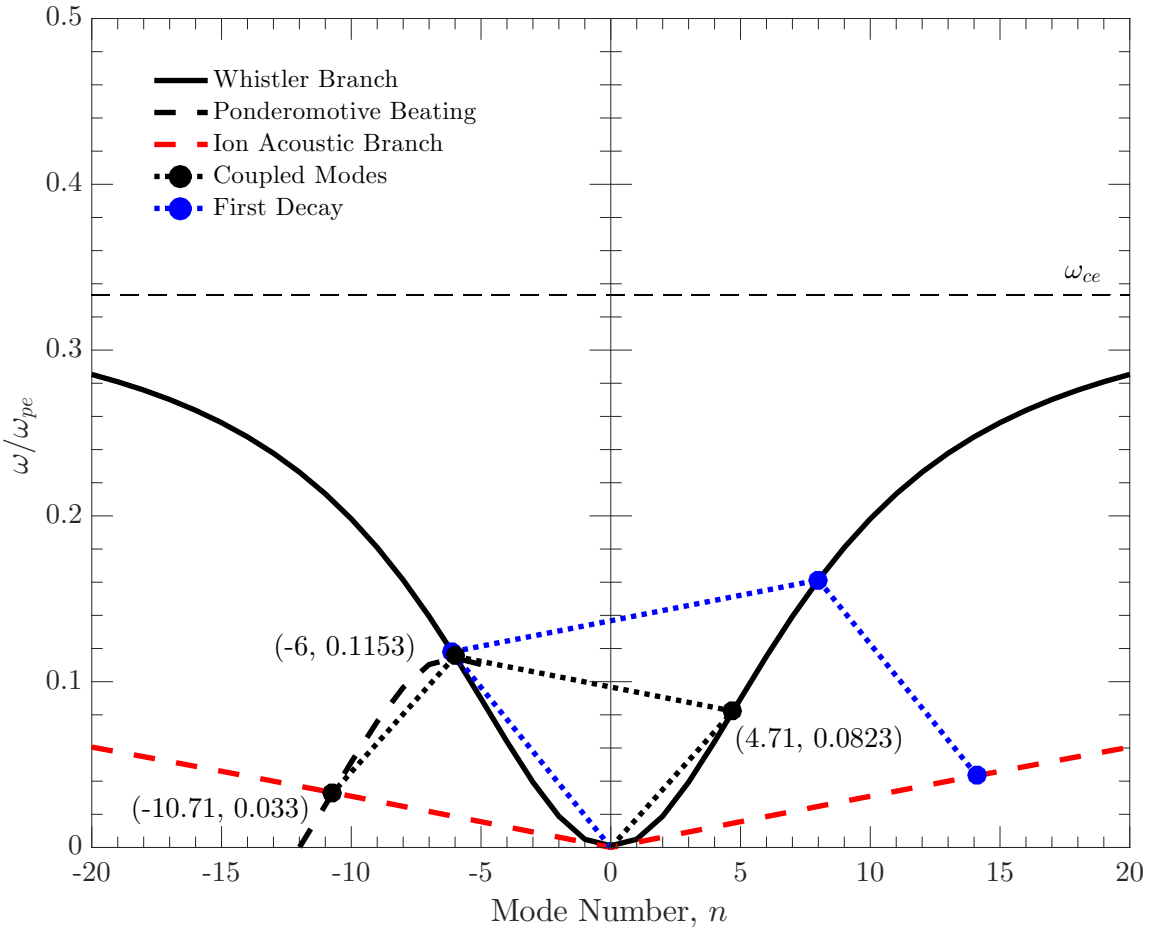

Figure 5.14: The theoretical parametric decay coupling for the observed double decay in Fig. 5.11. The whistler branch is indicated by the solid black line, the ponderomotive beating of the $n_{H1} = -6$ daughter whistler mode with the forwards travelling whistler branch is indicated by the black dashed line, the ion acoustic mode is indicated by the red dashed line, and the coupled modes are indicated by large black dots with dotted connecting lines. The mode number and normalized frequency of the coupled modes are indicated next to the black dots. The single decay that preceded this second decay is indicated by the blue dots and dotted connecting line.

again approximately satisfy the parametric decay conditions of Eqs. (2.27) and (2.28) where the daughter whistler wave of the previous single decay takes the place of the pump wave in the three-wave coupling. Fig. 5.14 shows the theoretical decay of the $n_{H1} = -6$ whistler mode acting as a pump wave into a forwards travelling whistler

and backwards travelling ion acoustic mode; we see that the same ponderomotive branch as the single decay is the dominant decay path. The original pump whistler is of large enough amplitude that it decays once into a daughter whistler and ion acoustic mode, and a second time through the single decay channel of the daughter whistler mode. It is interesting to note that Fig. 5.12a shows that the growth rate of the the $H2$ whistler is larger than the $H1$, while Fig. 5.13a shows the $L1$ ion mode grows faster than the $L2$ ion mode. This seems to indicate that both decays happen nearly simultaneously and there are more complex dynamics determining the growth rates of each mode. The simulation daughter modes $H2$ and $L2$ are less of a match for the theoretical daughter modes than the first decay, this can be attributed to the exact solution having non-integer mode numbers further from integer modes. The frequency discrepancy between $n = 4.71$ and $n = 5$ is large enough that the ion acoustic mode deviates significantly from the theoretical dispersion but is still able to form the coupling due to the width of the undamped ion acoustic mode mentioned previously when discussing Fig. 5.6b.

Finally, we present a third simulation with the pump amplitude increased further to $\delta B/B_0 = 0.11$. Fig. 5.15 displays the E_y and δn_i space-time diagrams. The E_y evolution in Fig. 5.15a again shows the decay of the pump wave into multiple whistler waves and multiple ion acoustic modes are also present in Fig. 5.15b. The now familiar E_y and δn_i Fourier analyses are presented in Fig. 5.16 and Fig. 5.17, respectively. In Fig. 5.16a we see the sequential growth of three daughter whistler modes at $n_{H1} = -6$, $n_{H2} = 5$, $n_{H3} = -4$. Fig. 5.16b reveals these are again all whistler modes but also that there is some power in the $(n = 4, \omega = 0.075\omega_{pe})$ mode; we will define this as the $\widetilde{H2}$ mode and return to it shortly. In the ion mode evolution shown in Fig. 5.17a we see the familiar $n_{L1} = 14$ and $n_{L2} = -11$ daughter modes as well as a third $n_{L3} = 9$ mode. The full dispersion plot in Fig. 5.17b shows there is

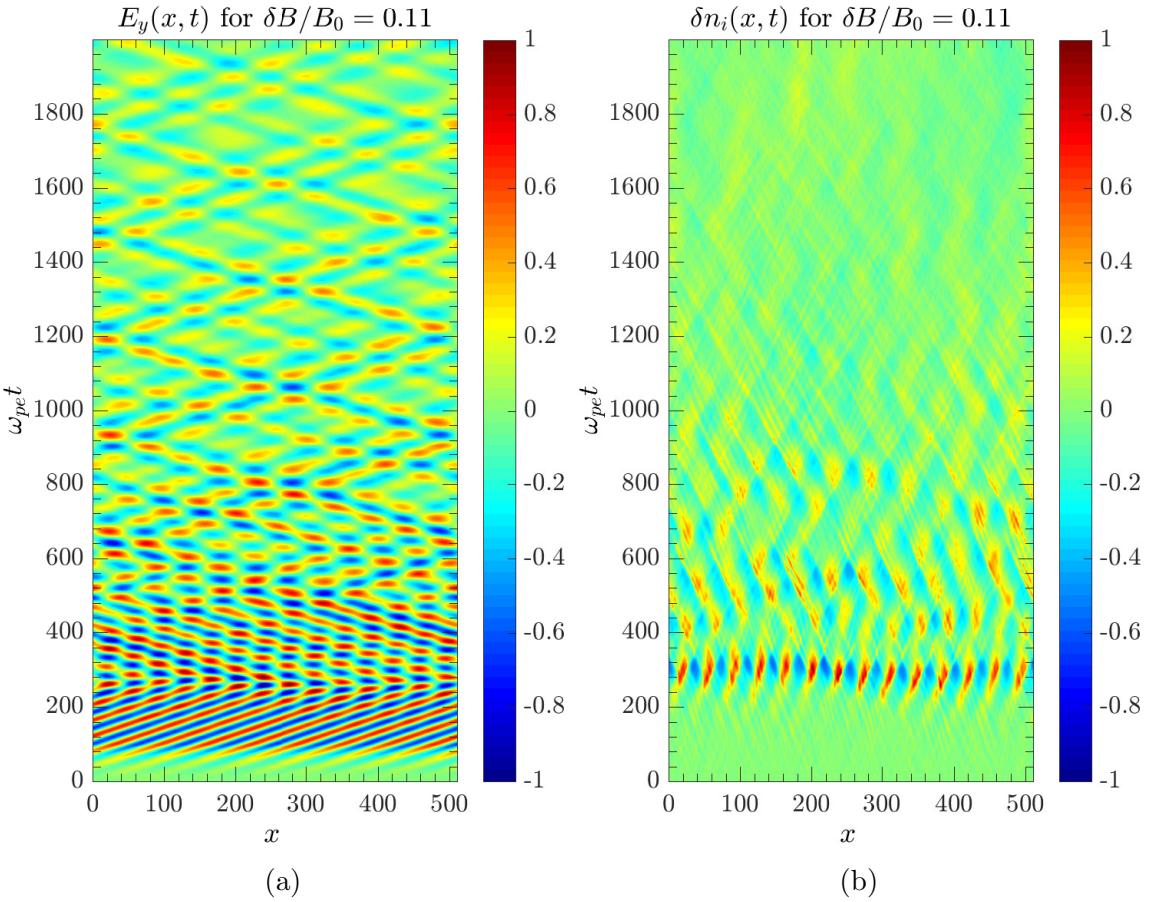

Figure 5.15: The triple parametric decay of a pumped whistler wave is observed. (a) The E_y component of the electric field space-time diagram, the pumped whistler begins the first decay at $\omega_{pe}t \approx 200$. (b) The ion density evolution, generation of new ion acoustic modes coincides with the growth of whistler wave modes in (a).

also a fourth ion acoustic mode at $(n = -10, \omega = 0.044\omega_{pe})$, which we will call the $\widetilde{L2}$ mode.

The $\widetilde{H2}$ and $\widetilde{L2}$ modes are easily understood from the parametric matching conditions,

$$n_{\widetilde{H2}} + n_{\widetilde{L2}} = 4 + (-10) = -6 = n_{H1}$$

$$\omega_{\widetilde{H2}} + \omega_{\widetilde{L2}} = 0.075\omega_{pe} + .044\omega_{pe} = 0.119\omega_{pe} = \omega_{H1}$$

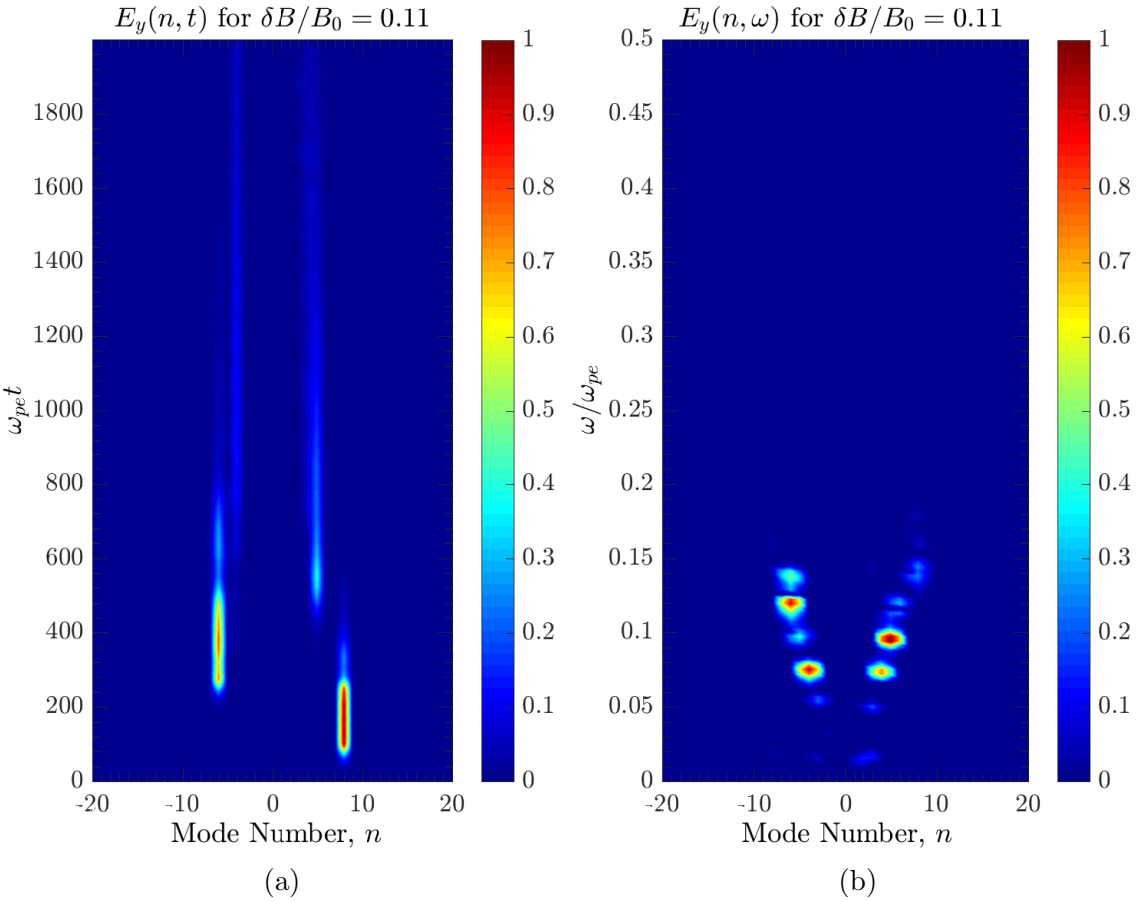

Figure 5.16: (a) The E_y component of the electric field (n,t) diagram, the pump and three daughter whistler mode numbers are clearly visible. These modes correspond to integer mode numbers $n_P = 8$, $n_{H1} = -6$, $n_{H2} = 5$, and $n_{H3} = -4$. (b) The E_y component of the electric field (n,ω) diagram, the daughter modes in (a) are clearly identified along the whistler branch with corresponding frequencies $\omega_{H1} \approx 0.119\omega_{pe}$, $\omega_{L2} \approx 0.094\omega_{pe}$, and $\omega_{L1} \approx 0.075\omega_{pe}$. Additionally, there is some power in the $(n_{\widetilde{H2}} = 4, \omega_{\widetilde{H2}} = 0.075\omega_{pe})$ mode though significantly reduced in power that it is not clearly visible in (a).

that show this is also a three-wave coupling with the $H1$ mode acting as the pump. As previously mentioned, the exact conditions for the coupling of the $H1$ mode to the whistler and ion acoustic branches lie far from integer mode numbers and this second coupling with $\widetilde{H2}$ and $\widetilde{L2}$ is also possible because of the periodic boundary conditions.

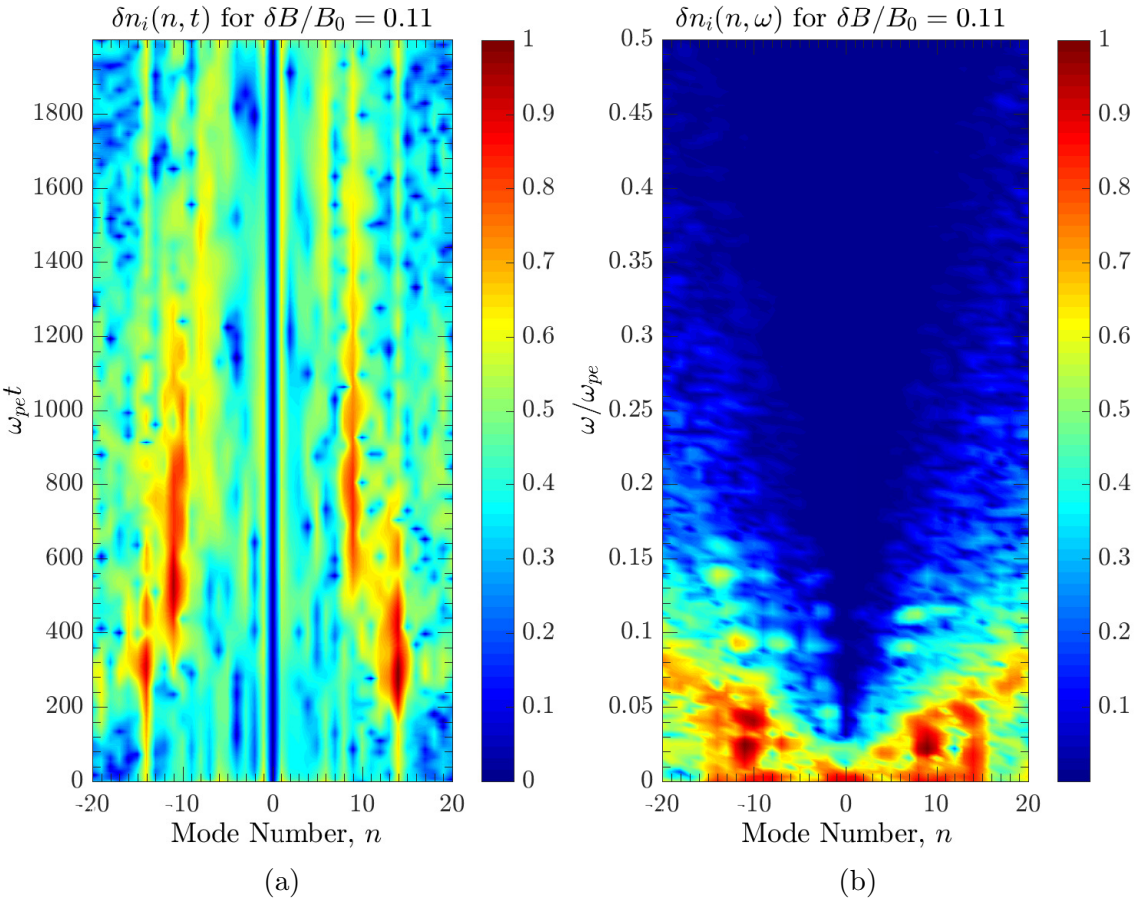

Figure 5.17: (a) The mode number evolution of the ion density, the three daughter ion acoustic mode numbers are clearly visible. These modes correspond to integer mode numbers $n_{L1} = 14$, $n_{L2} = -11$, and $n_{L3} = 9$. (b) The (n, ω) map of the ion density, the modes in (a) are clearly identified along the ion acoustic branch with frequencies $\omega_{L1} \approx 0.044\omega_{pe}$, $\omega_{L2} \approx 0.026\omega_{pe}$, and $\omega_{L3} \approx 0.028\omega_{pe}$. There is a fourth mode at $(n_{\widetilde{L2}} = -10, \omega_{\widetilde{L2}} = 0.044\omega_{pe})$.

The $H3$ and $L3$ modes correspond to a triple parametric decay where the $H2$ mode has acted like the pump wave, namely,

$$n_{H3} + n_{L3} = -4 + (9) = 5 = n_{H2}$$

$$\omega_{H3} + \omega_{L3} = 0.075\omega_{pe} + .028\omega_{pe} = 0.103\omega_{pe} \approx \omega_{H2} = 0.094\omega_{pe}$$

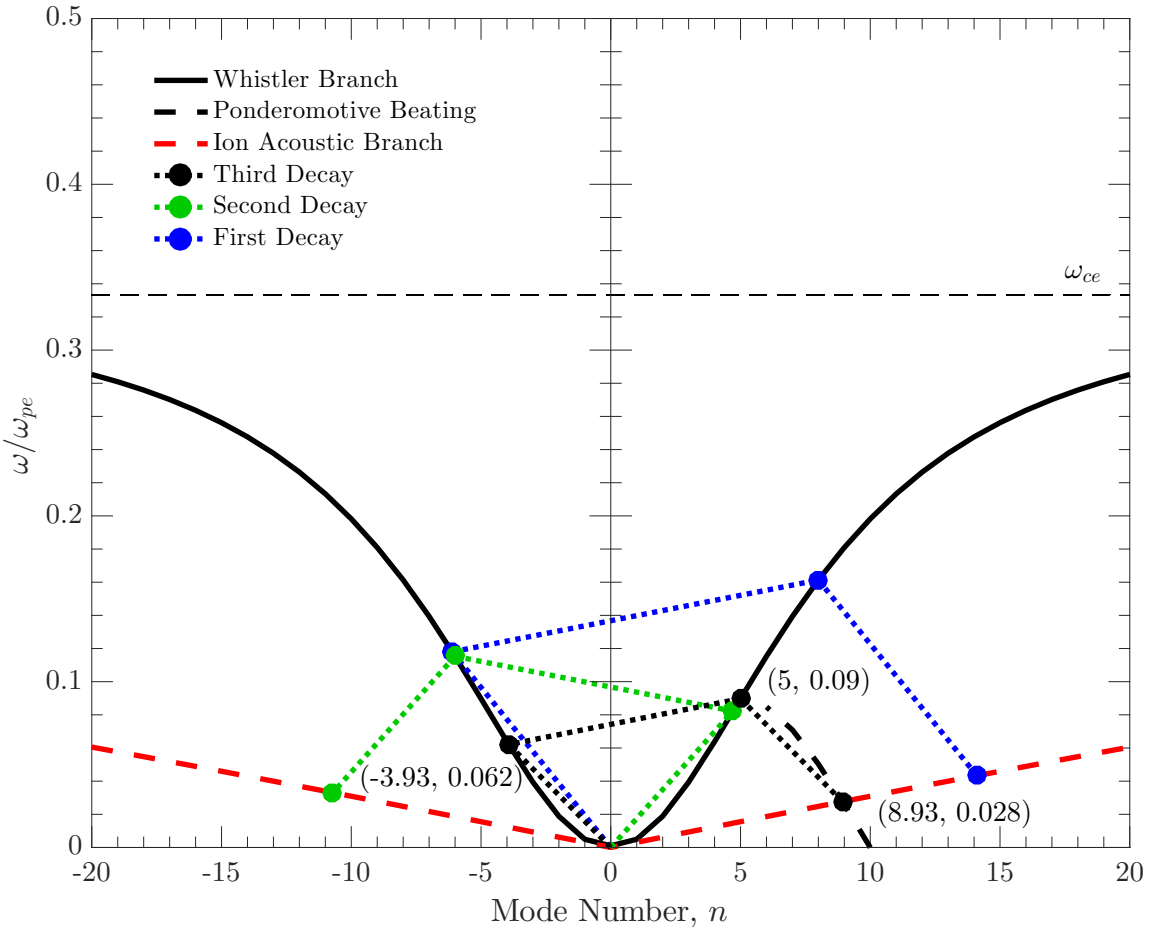

Figure 5.18: The predicted parametric decay coupling for the decay depicted in Fig. 5.15 that produces three whistler and three ion acoustic daughter waves. The whistler branch is indicated by the solid black line, the ponderomotive beating of the backwards travelling whistler branch with the $n_{H2} = 5$ whistler mode is indicated by the black dashed line, the ion acoustic mode is indicated by the red dashed line, and the coupled modes are indicated by large black dots with dotted connecting lines. The mode number and normalized frequency of the coupled modes are indicated next to the black dots. The single and double decay couplings leading up to this decay are also indicated by blue and green dots and dotted connecting lines, respectively.

where the parametric decay conditions are again approximately met within the resolution of the simulation frequency domain. This theoretical triple decay process where the $n_{H2} = 5$ mode acts as the pump in the final decay is depicted in Fig. 5.18 with the

final decay modes indicated. The same ponderomotive branch as the previous two decays acts as the coupling mechanism between the electromagnetic and electrostatic modes. In Fig. 5.16a and Fig.5.17a we show the simulation with a temporal scale up to $\omega_{pe}t = 2000.0$ to clearly demonstrate that no further decay of the $H3$ whistler mode occurs at $\delta B/B_0 = 0.11$. Increasing the amplitude beyond $\delta B/B_0 = 0.11$ causes a computational error in the Darwin code, believed to be caused by the iterative method of advancing the fields not converging due to large perturbations in the ion density from the growth of the acoustic modes.

5.2.2 GROWTH RATES AND ENERGY TRANSFER

Using the spatial Fourier analysis (n, t) plots we can isolate the temporal evolution of the individual modes to measure the growth rates. Fig. 5.19a shows the normalized growth rates Γ/ω_{pe} of the three daughter whistler waves as a function of the pump wave amplitude. It is obvious that the $H1$ mode (black) does not have a well defined relationship with the pump wave amplitude. As the $H2$ mode (red) begins to have a non-zero growth rate the $H1$ growth rate drops significantly and the $H2$ growth dominates, this is consistent with the result in Fig. 5.12a. A similar feature does not occur with the $H3$ mode (blue) becoming dominant, as it appears to reach a low growth saturation point rather quickly. At larger amplitudes the $H1$ mode recovers as the dominant mode with a growth rate more than double the $H2$ mode and nearly an order of magnitude larger than the $H3$ mode. Fig. 5.19b shows the temporal evolution of the three daughter whistler waves for the largest amplitude pump wave indicated by the vertical, black, dashed line in Fig. 5.19a; also shown is the growth and subsequent decay of the pump whistler (green). We see that the growth of all three daughter waves begins at $\omega_{pe}t \approx 200$ with the decay of the pump wave beginning shortly after. This demonstrates that the triple decay channels are all beating and

growing simultaneously, with the original pump wave providing the energy for the growth. This, along with the dominance of the $H2$ mode over the $H1$ at moderate amplitudes, shows that it is not necessary for the intermediate waves to have grown to significant amplitude for the next decay process to occur. Later in time we see that the three daughter waves reach nearly identical signal power while the pump wave has decayed to a power level consistent with the thermal noise power of the daughter waves at the beginning of the simulation.

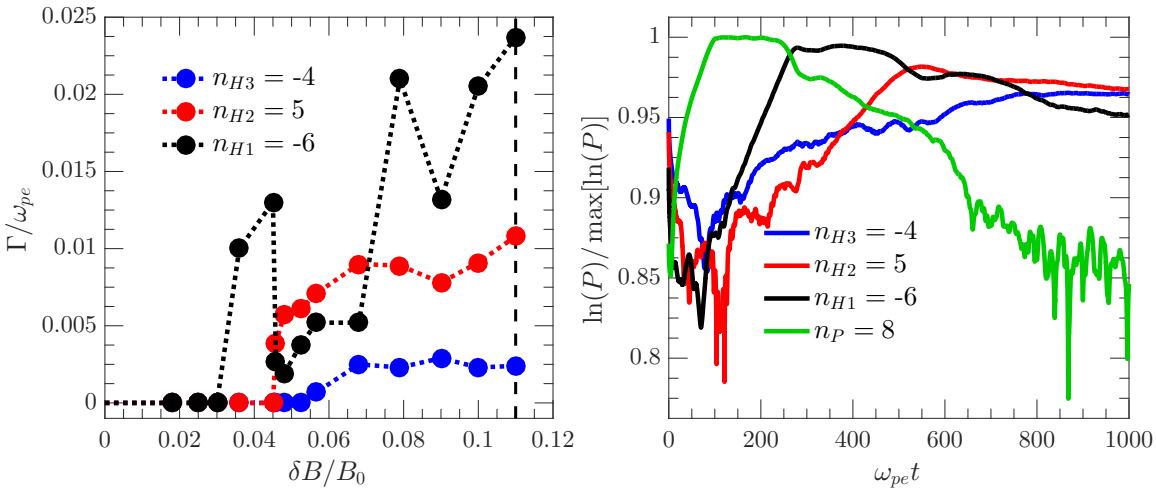

Figure 5.19: (a) The growth rates for the three daughter whistler waves as a function of the wave amplitude. (b) The whistler wave growth for the triple decay indicated by the vertical dashed line in (a), also indicated in green is the launch and decay of the pump whistler.

Fig. 5.20 is a qualitative analysis of the transfer of energy during the triple decay process depicted in Fig. 5.19b. Fig. 5.20a shows the ion (blue) and electron (red) kinetic energy evolution, both are normalized to the maximum energy reached individually. In Fig. 5.20b the transverse and longitudinal electric field are each normalized to the maximum energy of the transverse field. The transverse field energy is ramped up during the addition of the external fields, at the same time the electrons

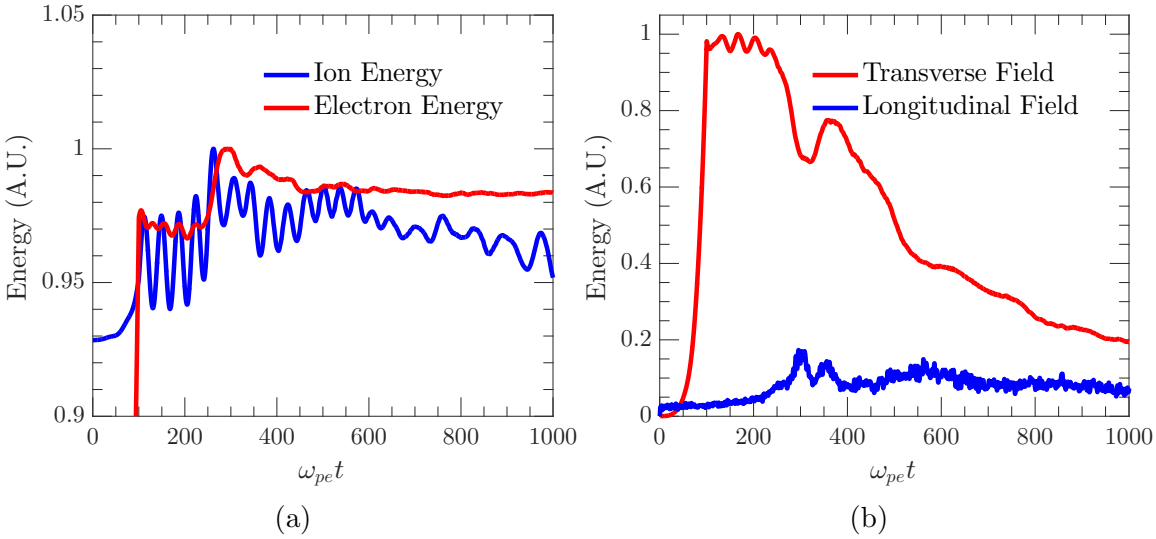

Figure 5.20: The qualitative view of the energy dynamics during the triple decay of a whistler wave. (a) The ion (blue) and electron (red) kinetic energy evolution, each is normalized to the maximum energy reached during the decay. (b) The transverse (red) and longitudinal (blue) electric field energy, each is normalized to the maximum energy of the transverse field.

gain energy from the transverse fields during cyclotron motion; some of this is also then transferred to the ions. After the external field is turned off ($\omega_{pe}t = 100.0$) the ion kinetic energy develops a modulation in the range ion acoustic modes. At $\omega_{pe}t \approx 200$, the same time the daughter whistler modes begin to grow in Fig. 5.19b, the ion, electron, and longitudinal field energy begin to grow while the transverse field energy decreases. The growth of the longitudinal field energy is consistent with the growth of the IAW, which transfers energy to the ions and electrons.

5.3 Electron Acoustic Coupling

For the final scenario we present simulations with an undamped EAW, achieved with hot and cold electron species. The parameters used to achieve this are the thermal velocities $v_{th} = 3.16$ and $v_{tc} = 0.316$, and population densities $n_h = 0.9n_e$ and $n_c = 0.1n_e$ where the subscripts h and c again refer to the hot and cold populations, respectively. The system length is $N_x = 2048$ cells, the total number of electron particles is $N_{pe} = 3.6864 \times 10^6$, and the cyclotron frequency is again $\omega_{ce} = \omega_{pe}/3$. We first present simulation results with these parameters when no whistler is pumped in the system; Fig. 5.21b shows the longitudinal electric field dispersion analysis. The Langmuir branch is located at the plasma frequency at low k and gradually rises at larger k due to thermal effects. At lower frequencies we see the electron acoustic mode is now undamped, the white dashed line is the theoretical dispersion defined by Eq. (2.5). Fig. 5.21a shows the electron acoustic dispersion (dashed red) along with whistler (solid black) and ponderomotive beating branches (dashed black). We see that the current setup is similar to the ion acoustic scenario just presented and we should expect to see a similar decay to a EAW with a mode number near the pump and very low mode number whistler. The ponderomotive beating is particularly strong here since the whistler that the pump is beating with experiences very minimal cyclotron damping, as seen in Fig. 5.5b.

Next we introduce a pump whistler with amplitude $\delta B/B_0$ to the system; Fig. 5.22 shows the resulting dispersion analysis. The transverse E_y field in Fig. 5.22a shows that the pump whistler is excited, along with a broad range of the whistler branch in the region around the pump mode. In the E_x field we see a beam-like dispersion with a phase velocity equivalent to the pump wave that bears a striking similarity to the single electron species result. Additionally, we can see that no region of the elec-

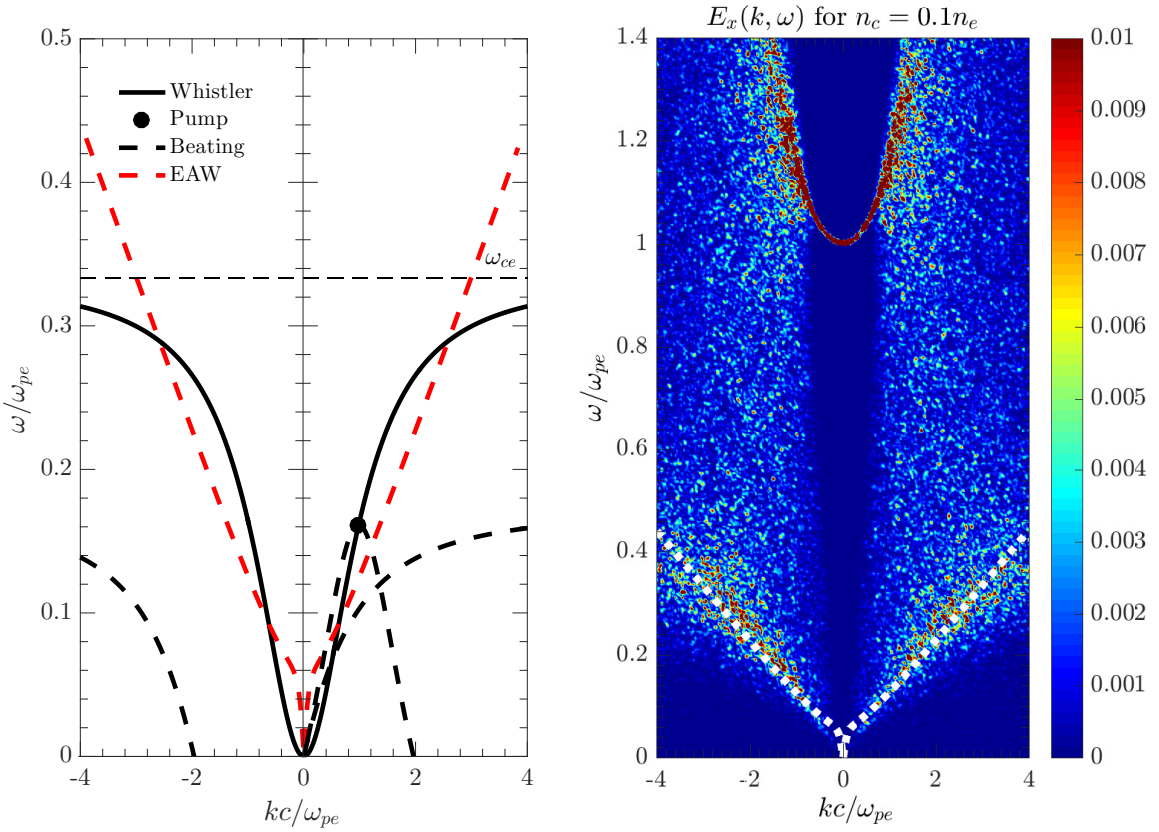

(a) (b)

Figure 5.21: (a) The possible parametric decay channels for a pumped whistler into an electron acoustic mode. The whistler branch is indicated by the solid black line, the pump whistler by a black dot, the ponderomotive branches present in the simulation are indicated by the dashed black line, and the electron acoustic dispersion defined by Eq. (2.5) is indicated by the red dashed line. (b) The undamped electron acoustic dispersion from the E_x field in the simulation for a temperature ratio of $T_h/T_c = 100$ and cold density $n_c = 0.1n_e$; the dispersion shows a good match with the theoretical dispersion indicated by the dashed white line.

tron acoustic branch is significantly excited, even though the ponderomotive beating branch is visibly intersecting the right travelling branch. We can conclude that the same Langmuir wave coupling seen previously has resulted, with the cold population stabilizing the decay of the pump whistler mode and thus keeping the beam mode to a sharper range of phase velocities than that seen in Fig. 5.2b. This is supported

by the stable whistler mode seen in the single cold electron simulations depicted in Fig. 5.3, The conditions are such that the parametric decay of a whistler into an EAW and another whistler should occur, but this is not seen. It is likely that the Langmuir coupling is dominating over the electron acoustic coupling, and not that the EAW coupling cannot occur. In the ion acoustic coupling the ponderomotive force directly couples to the electrons which is then transmitted to the ions, so there is no physical reason the ponderomotive force cannot not drive an electron acoustic mode.

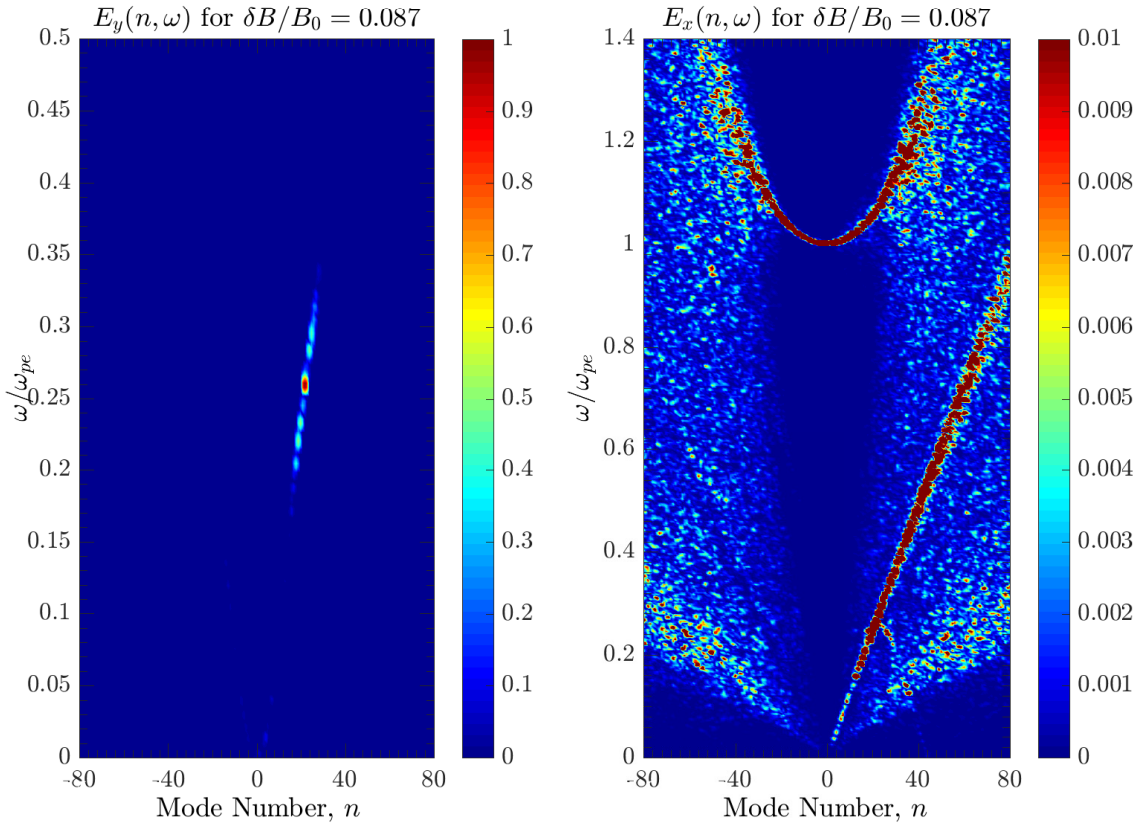

Figure 5.22: A whistler with $\delta B/B_0$ is launched in the presence of an undamped ion acoustic dispersion. (a) The transverse E_y electric field (n,ω) map shows the pumped whistler develops low power side bands. (b) The E_x field (n,ω) map shows there is no parametric decay to the EAW branch, the same Langmuir coupling seen in Fig. 5.2b occurs.

5.4 Discussion

Here we will discuss the relevance of the simulation results to physical observations. *Agapitov et al. (2015)* [28] state that the parametric decay of a whistler wave into both an IAW and EAW are very similar processes. However, it is clear from our simulation results that coupling to the EAW mode is not as easily achieved as in the IAW case. Our results from the IAW coupling show remarkable agreement with theory, with the largest discrepancies coming from the periodic boundary restrictions on the spatial mode numbers. Though we do not present the results here, simulations were conducted with $T_e/T_i = 1$ when the IAW is severely Landau damped. In these simulations the whistler and IAW coupling does not occur, and we again see the Langmuir wave coupling phenomena. In Fig. 5.6b we see that the IAW mode has significant power above the background, while in Fig. 5.21b it is necessary to reduce the color scale by 2 orders of magnitude to reveal the presence of the EAW due to the power in the Langmuir modes. Additionally, even in the parametric coupling to the IAW branch we see other acoustic modes with comparable power to the acoustic mode involved in the coupling. This would suggest that it may be necessary to reduce the damping of the EAW even further to achieve dominance over the Langmuir coupling. The event interpreted as the parametric decay of a whistler into an EAW in *Agapitov et al. (2015)* has conditions where the hot population has a drift relative to the cold. As mentioned in Chapter 2, a relative drift between hot and cold populations can result in the electron acoustic instability, where EAW modes will actually grow. It is possible that these conditions would more closely resemble the IAW conditions and coupling of the whistler to the EAW would be more easily facilitated.

Further complicating the issue is the location of the cyclotron frequency with respect to the undamped region of the EAW branch in space plasmas. The electron

populations in *Agapitov et al. (2015)* are in the range of $n_h \sim 1 - 3\text{cm}^{-3}$ and $n_c \sim 5 - 6\text{cm}^{-3}$, giving at minimum a cold population of $n_c = 0.7n_e$. *Gary and Tokar (1985)* [47] highlight that without a relative drift of the populations the lowest undamped frequency of the electron acoustic wave will be $\sim \omega_{pc}$, this is supported by Fig. 5.21b where $\omega_{pc} \sim 0.1\omega_{ce}$. For the parameters in *Agapitov et al. (2015)* this will result in $\omega_{pc} > \omega_{ce}$; thus, the EAW branch will be above the whistler branch and will not intersect the ponderomotive branches that couple into the electrostatic modes via the ponderomotive force. When a relative drift is present *Gary (1987)* [48] show that the entire EAW branch is undamped, allowing for ponderomotive coupling even when $\omega_{pc} > \omega_{ce}$. This suggests that for typical space plasma conditions the electron acoustic instability driven by a relative drift of the hot and cold populations becomes necessary to observe whistler wave coupling to the EAW mode. Futhermore, even in plasma conditions where $\omega_{pc} < \omega_{ce}$ but there is no relative drift our simulations show that whistler wave coupling to the EAW is difficult to achieve as other processes may dominate.

CHAPTER 6.

Summary and Future Work

In this chapter we make a summary of this thesis and outline possible future work that stems from our results and the outstanding questions surrounding them. In Chapter 1 two motivational topics for this research were presented. The discovery of large amplitude oblique whistler waves in the Earth's outer radiation belt by STEREO spacecraft and reported by *Cattell et al., 2008* [20] suggests a new mechanism for the energization of radiation belt electrons. Subsequent efforts were made to model and understand the space dynamics of these waves; the data interpretation by *Kellogg et al. (2010)* and fluid modelling by *Yoon (2011)* highlighted the importance of nonlinear processes associated with these waves, namely those of particle trapping and wave steepening, respectively. These results call for a better understanding of the basic nonlinear dynamics of oblique whistler waves.

Separately, *Mozer et al. (2013)* reported on Van Allen Probe satellite observations of large numbers of spiked signals in the electric field dubbed Time Domain Structures. It was shown in *Artemyev et al. (2014)* that these structures were capable of rapidly accelerating radiation belt electrons, emphasizing their importance to global belt dynamics. *Agapitov et al (2015)* presented detailed satellite measurements that were interpreted as the parametric decay of a whistler wave into an oppositely travelling whistler wave and an electron acoustic wave. They conclude that this parametric decay process into electron acoustic waves is the source of the fine scale structures reported in *Mozer et al. (2013)*. This observed whistler wave-wave interaction provides

the motivation for investigation into the basic processes of whistler wave coupling with electrostatic wave modes.

Sufficient background knowledge on the wave modes and plasma physics concepts relevant to this work was presented in Chapter 2, namely the whistler, ion acoustic, and electron acoustic wave modes and the ponderomotive force which provides a coupling mechanism for parametric decay processes. The results of this thesis are all simulation based and the basics of plasma modelling using Particle-in-Cell codes was outlined in Chapter 3; the KEMPO1 and UPIC Darwin codes and the simulation setups used to study whistler waves with each were explained in detail.

Chapter 4 presented results of one-dimensional relativistic particle simulations with self-consistent electromagnetic fields modelling the dynamics of large amplitude oblique whistlers. A perturbation was applied to the initial conditions of a cold plasma to launch a large amplitude wave consistent with the oblique whistler dispersion relation. Our results highlighted three major time scales of the wave evolution associated with nonlinear processes: wave steepening, particle trapping, and particle acceleration. The wave amplitude scaling law determined for the wave steepening time is consistent with steepening modelled in *Yoon (2011)*, and is in agreement with *Yoon (2014)* that the angle of propagation with respect to the whistler resonance cone plays a large role in the development of wave steepening. Our results demonstrated that the occurrence of particle trapping orbits in phase space coincides with the formation of large electrostatic wave potentials and wave distortion, supporting the conclusions of *Kellogg et al. (2010)* and calling attention to the subsequent whistler wave damping. Large amplitude oblique whistlers were observed to thermalize a cold Maxwellian distribution of self-consistent particles from ~ 1 eV to ~ 100 eV, while inserting a warm seed population of non-interacting particles at ~ 100 eV results in acceleration of particles up to $\sim 20-30$ keV. This work could be extended to include

a more detailed analysis of the trapped particle density profile and polarization of the field distortion to compare with those predicted by *Kellogg et al., 2010*. Additionally, performing simulations with the non-interacting test particles distributed such that most of the particles are nearly resonant with the phase velocity of the wave may demonstrate that acceleration to MeV energies is possible, but for only a small portion of an isotropic distribution.

One-dimensional simulations modelling wave-wave interactions of parallel propagating whistlers with electrostatic modes were presented in Chapter 5. A wave consistent with the parallel whistler dispersion was launched by pumping the self-consistent transverse electric fields with external source terms. We presented results of simulations of the pump wave in three scenarios involving different electrostatic modes: Langmuir waves, ion acoustic waves, and electron acoustic waves. The whistler wave was not expected to interact with the Langmuir waves through the ponderomotive force. However, simulations with a single warm electron species showed the decay of the pump whistler into a broadband whistler spectrum and the generation of a beam-like electrostatic mode. Identical wave parameters with a cold electron distribution revealed the whistler mode couples into the electrostatic field and forms a spatial beating pattern with the Langmuir branch; the mechanism permitting this nonlinear coupling to the electrostatic field is not well understood but may be due to higher order $\mathbf{J} \times \mathbf{B}$ forces. Simulations involving a moving ion species in addition to electrons provided a path for ponderomotive coupling to the low frequency undamped ion acoustic mode. We presented simulation results detailing the single, double, and triple parametric decay of a whistler wave into a backscattered whistler and ion acoustic wave. The decay paths showed remarkable agreement with a simple model of parametric decay facilitated by the ponderomotive force. A similar decay process was expected for simulations involving two electron species at different tem-

peratures, creating a condition where the electron acoustic mode is lightly damped. However, simulation results showed a similar coupling to the Langmuir mode instead of the electron acoustic branch. It is concluded that this dominance of the Langmuir wave coupling is likely due to the electron acoustic wave still experiencing relatively large damping compared to the ion acoustic wave in the previous scenario, which has incoherent thermal modes with wave power comparable to the coherent modes involved in the parametric decay. We make note that the damping of the electron acoustic mode may be reduced further by using a relative drift between the hot and cold populations [48]. Such are the conditions in *Agapitov et al. (2015)*, and given typical space parameters we suggest that this relative drift may indeed be necessary to facilitate the coupling of the whistler wave to the electron acoustic branch in the parametric decay process reported. This leads to the obvious extension to repeat the simulations designed to observe the parametric decay of a whistler into an electron acoustic wave but using a relative drift between the hot and cold electron populations; a parametric decay process in this scenario would possibly model the observation by *Agapitov et al (2015)*.

References

[1] R.A. Helliwell and M.G. Morgan, Proceedings of the IRE **47**, 200 (1959).

[2] R.L. Stenzel, J. Geophys. Res. **104**, 14379 (1999).

[3] H. Barkhausen, Physikalische Zeitschrift **20**, 401 (1919).

[4] T.L. Eckersley, Nature **122**, 768, (1928).

[5] T.L. Eckersley, Marconi Rev. **5**, 5, (1931).

[6] E.T. Burton adn E.M. Boardman, Proceedings of the IRE **21**, 1476 (1933).

[7] T.L. Eckersley, Nature **135**, 104, (1935).

[8] L.R.O. Storey, Phil. Trans. Roy. Soc. A **246**, 113 (1953).

[9] J.R. Koster and L.R.0. Storey, Nature **175**, 36 (1955).

[10] M.G. Morgan and G.M. Allcock, Nature **177**, 30 (1956).

[11] J.H. Crary, R.A. Helliwell, and R. F. Chase, J. Geophys. Res. **61**, 35 (1956).

[12] D.I. Golden, M. Spasojevic, and U.S. Inan, J. Geophys. Res. **114**, A05212 (2009).

[13] Y. Narita, R. Nakamura, W. Baumjohann, K.-H. Glassmeier, U. Motschmann, B. Giles, W. Magnes, D. Fischer, R.B. Torbert, C.T. Russell, R.J. Strangeway, J.L. Burch, Y. Nariyuki, S. Saito, and S.P. Gary, Astrophys. J. Lett. **827**, L8 (2016).

[14] W.S. Kurth, B.D. Strayer, D.A. Gurnett, and F.L. Scarf, ICARUS **61**, 497 (1985).

[15] D.A. Gurnett, T.F. Averkamp, P. Schippers, A.M. Persoon, G.B. Hospodarsky, J.S. Leisner, W.S. Kurth, G.H. Jones, A.J. Coates, F.J. Crary, Geophys. Res. Lett. **38**, L06102 (2011).

[16] C.F. Kennel and H.E. Petschek, J. Geophys. Res. **71**, 1 (1966)

[17] W. Baumjohann, and Rudolf A. Treumann, *Basic Space Plasma Physics* (Imperial College Press, London, 2012), p. 243-285, Rev. Ed.

[18] Stanford VLF Group, *Whistler-mode Wave Studies at Palmer Station, Antarctica*, `http://vlf.stanford.edu/research/whistler-mode-wave-studies-palmer-station-antarctica`, Accessed: 08/04/2017.

[19] P.H. Yoon, Geophys. Res. Lett. **38**, L12105 (2011)

[20] C.A. Cattell, J.R. Wygant, K. Goetz, K. Kersten, P.J. Kellogg, T. von Rosenvinge, S.D. Bale, I. Roth, M. Temerin, M.K. Hudson, R.A. Mewaldt, M. Wiedenbeck, M. Maksimovic, R. Ergun, M. Acuna, and C.T. Russell, Geophys. Res. Lett. **35**, L01105 (2008).

[21] P.J. Kellogg, C.A. Cattell, K. Goetz, S.J. Monson, and L.B. Wilson III, J. Geophys. Res. **116**, A09224 (2011).

[22] L.B. Wilson III, C.A. Cattell, P.J. Kellogg, J.R. Wygant, K. Goetz, A. Breneman, and K. Kersten, Geophys. Res. Lett. **38**, L17107 (2011).

[23] P.J. Kellogg, C.A. Cattell, K. Goetz, S.J. Monson, and L.B. Wilson III, Geophys. Res. Lett. **37**, L20106 (2010).

[24] J. Bortnik, R.M. Thorne, and U.S. Inan, Geophys. Res. Lett. **35**, L21102 (2008).

[25] X. Tao, J. Bortnik, Nonlin. Processes Geophys. **17**, 599 (2010).

[26] F.S. Mozer, S.D. Bale, J.W. Bonnell, C.C. Chaston, I. Roth, and J. Wygant, Phys. Rev. Lett. **111**, 235002 (2013).

[27] A.V. Artemyev, O.V. Agapitov, F. Mozer, and V. Krasnoselskikh, Geophys. Res. Lett. **41**, 5734 (2014).

[28] O.V. Agapitov, V. Krasnoselskikh, F.S. Mozer, A.V. Artemyev, and A.S. Volokitin, Geophys. Res. Lett. **42**, 3715 (2015).

[29] D.A. Gurnett, and A. Bhattacharjee, *Introduction to Plasma Physics: With Space and Laboratory Applications* (Cambridge University Press, 2005), p. 84-90.

[30] F.F. Chen, *Introduction to Plasma Physics and Controlled Fusion, 2nd Ed.* (Plenum Press, New York, 1984), p. 79-147, 305-317, 2nd Ed.

[31] D.R. Nicholson, *Introduction to Plasma Theory* (John Wiley and Sons, New York, 1983), p. 31-33.

[32] E.V. Appleton, U.R.S.I. Wash. Radio Conf. (1927).

[33] D.R. Hartree, Math. Proc. Camb. Phil. Soc. **27**, 143 (1931).

[34] M.T. Rietveld, P.N. Collis, and J.P. St. Maurice, J. Geophys. Res. **96**, A11 (1991).

[35] J.E. Wahlund, P. Louarn, T. Chust, H. de Feraudy, and A. Roux, Geophys. Res. Lett. **21**, 17 (1994).

[36] W.S. Kurth, D.A. Gurnett, and F.L. Scarf, J. Geophys. Res. **84**, A7 (1979).

[37] R.R. Anderson, G.K. Parks, T.E. Eastman, D.A. Gurnett, and L.A. Frank, J. Geophys. Res. **86**, A6 (1981).

[38] T. Neubert, Physica Scripta **26**, 239 (1982)

[39] T.H. Stix, *The Theory of Plasma Waves* (McGraw-Hill Book Co., New York, 1962), p. 132.

[40] A.Y. Wong, R.W. Motley, and N. D'Angelo, Phys. Rev. **133**, A436 (1964).

[41] B.D. Fried and R.W. Gould, Phys. Fluids **4**, 139 (1961).

[42] K. Watanabe and T. Taniuti, J. Phys. Soc. Japan **43**, 1819 (1977).

[43] M.Y. Yu and P.K. Shukla, J. Plasma Phys. **29**, 409 (1983)

[44] M.F. Thomsen, H.C. Barr, S.P. Gary, W.C. Feldman, and T.E. Cole, J. Geophys. Res. **88**, 3035 (1983).

[45] R.L. Tokar and S.P. Gary, Geophys. Res. Lett. **11**, 1180 (1984).

[46] C.S. Lin, J.L. Burch, S.D. Shawhan, and D.A. Gurnett, J. Geophys. Res. **89**, 925 (1984).

[47] S.P. Gary and R.L. Tokar, Phys. Fluids **28** 2439 (1985).

[48] S.P. Gary, Phys. Fluids **30**, 2745 (1987).

[49] M.A. Hellberg, R.L. Mace, R.J. Armstrong, and G. Karlstad, J. Plasma Phys. **64**, 433 (2000).

[50] M. Berthomier, R. Pottelette, M. Malingre, Y. Khotyaintsev, Phys. Plasmas **7**, 2987 (2000).

[51] C.E. Max, Phys. Fluids **19**, 74 (1976).

[52] G.J. Morales, Y.C. Lee, Phys. Rev. Lett. **33**, 1016 (1974).

[53] P.M. Bellan, K. Stasiewicz, Phys. Rev. Lett. **80**, 3523 (1998).

[54] D.J. Griffiths, *Introduction to Electrodynamics* (Prentice-Hall, New Jersey, 1999), Inside Cover Vector Identities, 3rd. Ed.

[55] Y. Omura and H. Matsumoto, KEMPO1: Technical Guide to One-Dimensional Electromagnetic Particle Code, *Computer Space Plasma Physics: Simulation Techniques and Software* (Terra Scientific Pub. Co., Tokyo, 1993), p. 21-65.

[56] V.K. Decyk, Computer Phys. Comm. **177**, 95 (2007).

[57] C.K. Birdsall and A.B. Langdon, *Plasma Physics via Computer Simulation* (McGraw-Hill Book Co., New York, 1985), p. 61-63.

[58] V.K. Decyk, *Description of Spectral Particle-in-Cell Codes from the UPIC Framework*, `https://picksc.idre.ucla.edu/wp-content/uploads/2015/05/UPICModels.pdf`, Accessed: 08/04/2017.

[59] Y. Omura, *Proc. ISSS-7*, March 26-31, 2005.

[60] K.S. Yee, IEEE Transactions on Antennas and Propagation **14**, 302 (1966).

[61] [Original German Version] R. Courant, K. Friedrichs, H. Lewy, Mathematische Annalen **100**, 32 (1928), [English Translation] R. Courant, K. Friedrichs, H. Lewy, IBM J. Res. Develop. **11**, 215 (1967).

[62] P.J. Palmadesso, Phys. Fluids **15**, 2006 (1972).

[63] P.H. Yoon, V.S. Pandey, and D.-H. Lee, J. Geophys. Res. Space Phys. **119**, 1851 (2014).